*M*ulti-scale descripti*o*n *o*f textural at*o*mizati*o*n *o*f liquid *o*xygen in liquid r*o*cket engine cry*o*genic flames

Leonardo Geiger

Normandie Université

UNIVERSITÉ DE ROUEN NORMANDIE

THÈSE

Pour obtenir le diplôme de doctorat

Spécialité **MECANIQUE DES FLUIDES, ENERGETIQUE, THERMIQUE, COMBUSTION, ACOUSTIQUE**

Préparée au sein de l'**Université de Rouen Normandie**

Multi-scale description of textural atomization of liquid oxygen in liquid rocket engine cryogenic flames

Présentée et soutenue par

LEONARDO GEIGER

Thèse soutenue le 09/12/2024

devant le jury composé de :

M. CHRISTOPHE DUMOUCHEL	Directeur de Recherche - Université de Rouen Normandie (URN)	Directeur de thèse
M. JEAN-BERNARD BLAISOT	Professeur des Universités - Université de Rouen Normandie (URN)	Co-directeur de thèse
M. FABIEN HALTER	Professeur des Universités - Université d'Orléans	Président du jury
M. NICOLAS FDIDA	Ingénieur de Recherche - Office National d'Etudes&recherches Aéro	Membre du jury
M. THIBAUT MENARD	Maître de Conférences - Université de Rouen Normandie (URN)	Membre du jury
MME MARIE THERON	INGENIEUR DE RECHERCHE RF - Centre National des Etudes Spatiales	Membre du jury
M. NATHANAEL MACHICOANE	Chargé de recherche HDR - Universite Grenoble Alpes	Rapporteur du jury
M. NICOLAS RIMBERT	Professeur des Universités - Université de Lorraine	Rapporteur du jury

Thèse dirigée par **CHRISTOPHE DUMOUCHEL** (COMPLEXE DE RECHERCHE INTERPROFESSIONNEL EN AEROTHERMOCHIMIE) et **JEAN-BERNARD BLAISOT** (Université de Rouen Normandie)

ED 591 PSIME

CORIA UMR 6614

UNIVERSITE DE ROUEN NORMANDIE

Multi-scale description of textural atomization of liquid oxygen in liquid rocket engine cryogenic flames

by

Leonardo GEIGER

A thesis submitted in partial fulfillment for the
degree of Doctor of Philosophy

in the
Ecole doctorale Physique, Sciences de l'Ingénieur, Matériaux et Energie

January 2025

ABSTRACT

The development of rocket engines to equip future launchers requires a better understanding of the complex physical phenomena that govern their operation. In the case of liquid-propelled rocket engines, the growing demand for engines that can be reliably reignited in space means that the transient phases such as start-up and shutdown must be better understood. These transient phases usually include subcritical injection regimes. Oxygen is injected in liquid state into the combustion chamber and undergoes a series of mechanisms: dense jet atomization, fragmentation of liquid ligaments, droplet evaporation, and turbulent combustion. Under these conditions, the combustion process is mainly driven by the atomization of the liquid oxygen, which must be accurately reproduced by simulation to better understand its role in the onset of combustion instabilities. Before using simulation as an autonomous tool to study the atomization process, it is necessary to ensure its level of accuracy. This requires conducting experimental test campaigns on test benches capable of reproducing conditions representative of rocket engines, such as the MASCOTTE test-bench at ONERA or the MARACA test-bench at CORIA. The goal of these studies is to characterize the atomization process and provide experimental data that can be used to develop and validate numerical models. The experimental study of primary atomization of liquid oxygen, in particular, relies on flow visualization techniques that depict the liquid structures involved in the process. The primary atomization process observed in liquid rocket engines can be categorized as textural or structural, depending on the scale at which the atomization takes place. Textural atomization processes are characterized by thin ligaments being peeled from the jet, while structural atomization is related with the breakup of the liquid bulk. Visualizations resulting from experimental test campaigns show very complex two-phase flows involving textural liquid systems that are difficult to characterize due to the wide range of spatial and temporal scales involved. To this day, no techniques are available to describe quantitatively the liquid ligaments involved in the textural atomization processes observed experimentally. In this thesis, a methodology is developed to characterize the textural primary atomization processes observed in the two-phase-flow conditions representative of those encountered in liquid rocket engines. Based on a multi-scale method developed at CORIA, this analysis provides a quantitative characterization of the size, shape and number of the textural liquid structures involved in the textural atomization process in its entire spatial scale range. This characterization provides information for the development of numerical primary atomization models. Additionally, the application of the methodology to liquid systems depicted by visualizations extracted from numerical simulations allow to validate the simulation results in terms of the correct reproduction of the liquid structures that participate in the textural atomization process.

Keywords: textural atomization, multi-scale description, turbulence, liquid rocket engines.

RESUME

Le développement des moteurs-fusées destinés à équiper les futurs lanceurs nécessite une meilleure compréhension des phénomènes physiques complexes qui régissent leur fonctionnement. Dans le cas des moteurs-fusées à ergols liquides, la demande croissante pour des moteurs pouvant être rallumés de manière fiable dans l'espace impose une profonde compréhension des phases transitoires, telles que le démarrage et l'arrêt. Ces phases transitoires incluent généralement des régimes d'injection sous-critiques. L'oxygène est injecté à l'état liquide dans la chambre de combustion et subit une série de mécanismes : atomisation du jet dense, fragmentation des ligaments liquides, évaporation des gouttelettes et combustion turbulente. Dans ces conditions, le processus de combustion est principalement gouverné par l'atomisation de l'oxygène liquide, qui doit être reproduite avec précision par simulation afin de mieux comprendre son rôle dans l'apparition des instabilités de combustion. Avant d'utiliser la simulation comme un outil autonome pour étudier le processus d'atomisation, il est nécessaire d'assurer son niveau de précision. Cela nécessite de mener des campagnes d'essais expérimentaux sur des bancs d'essais capables de reproduire des conditions représentatives de moteurs-fusées, tels que le banc d'essai MASCOTTE à l'ONERA ou le banc d'essai MARACA au CORIA. L'objectif de ces études est de caractériser le processus d'atomisation et de fournir des données expérimentales qui peuvent être utilisées pour développer et valider des modèles numériques. L'étude expérimentale de l'atomisation primaire de l'oxygène liquide repose en particulier sur des techniques de visualisation des écoulements, qui permettent de représenter les structures liquides impliquées dans le processus. Le processus d'atomisation primaire observé dans les moteurs-fusées à ergols liquides peut être catégorisé comme texturel ou structurel, selon l'échelle à laquelle se produit l'atomisation. Les processus d'atomisation texturelle se caractérisent par le détachement de fins ligaments du jet, tandis que l'atomisation structurelle est liée à la rupture du volume liquide principal. Les visualisations issues de campagnes d'essais expérimentaux révèlent des écoulements diphasiques très complexes impliquant des systèmes liquides texturaux difficiles à caractériser en raison de leur large gamme d'échelles spatiales et temporelles. À ce jour, aucune technique n'est disponible pour décrire quantitativement les ligaments liquides impliqués dans ces processus d'atomisation texturelle observés expérimentalement. Dans cette thèse, une méthodologie est développée pour caractériser les processus d'atomisation primaire texturelle observés dans des conditions d'écoulement diphasique représentatives de celles rencontrées dans les moteurs-fusées à ergols liquides. Cette analyse fournit une caractérisation quantitative de la taille, de la forme et du nombre des structures liquides texturelles impliquées dans le processus d'atomisation texturelle sur toute sa gamme d'échelles spatiales. Cette caractérisation fournit des données pour le développement de modèles numériques d'atomisation primaire. En outre, l'application de cette méthodologie à des systèmes liquides décrits par des visualisations extraites de simulations numériques permet de valider les résultats de simulation en termes de leur reproduction des structures liquides participant au processus d'atomisation texturelle.

Mots-clés : atomisation texturelle, description multi-échelles, turbulence, moteurs-fusées à ergols liquides.

Thesis framework

The research reported in this thesis is part of a collaboration between ONERA, CNES, and the CORIA laboratory (Université de Rouen Normandie), and was done with the financial support of ONERA and CNES.

The thesis was written under the co-direction of Dr. Christophe Dumouchel and Prof. Jean-Bernard Blaisot and under the supervision of Drs. Marie Théron, Nicolas Fdida and Luc-Henry Dorey.

Acknowledgements

First and foremost, I would like to express my gratitude to my PhD directors Christophe and Jean-Bernard for their invaluable guidance, encouragement and patience during this three-year journey. Their expertise has been crucial in shaping this research and my growth as a researcher. I would also like to thank my supervisors at ONERA, Nicolas and Luc-Henry, for their daily support and guidance. Nicolas, thank you for your constant encouragement—especially appreciated during all those (cryogenically) cold early-morning winter test runs on the MASCOTTE bench.

This research would not have been possible without the financial support of ONERA and CNES. I deeply appreciate their trust in this project and their commitment to advancing aerospace research. I would like to thank in particular my supervisor at CNES, Marie, for her trust and her specialist insight.

This work was both challenging and complex, requiring expertise across many different areas of liquid propulsion research. It would not have been possible without the help of numerous colleagues from both the ONERA and CORIA labs: in no particular order, I would like to thank Lucien, Aurélie, Eric, David, Sasha, Florian, Jean-Christophe, Julien, Michael, and Stéphane.

I cannot forget to mention the awesome PhD student crew at ONERA who made this journey so much more enjoyable. Turns out, a PhD is not just about work after all! From coffee breaks to grabbing a beer after long days in the lab, we kept each other sane—even when the work was driving us crazy. Special thanks to the couloir des doctorants, to the entire LPA PhD team, and to the CORIA PhD crew, who adopted me during my frequent trips to Rouen.

And of course, a huge thanks to my friends and family who somehow managed to put up with me through this rollercoaster. Special thanks to all my friends from Cité U (too many to mention), who made it nearly impossible to find a country where I don't have a place to stay when visiting. In particular, a big shout-out to the Fondation Danoise crew, for always making sure I didn't work too much! And to Anna, thanks for always keeping things interesting. To my family, thank you for always believing in me, even from a distance, even when I was busy buried in work. I couldn't have survived this without your love, patience and support. You've all made this whole adventure way more fun than I ever thought it would be!

Contents

General introduction

The rocket engines that will equip future launchers are being developed with the goal of increasing their reliability and reducing their cost. To achieve this, it is necessary to better understand the complex physical phenomena that govern their operation, in order to more accurately estimate the design margins that affect the cost and reliability of the engine. In the case of liquid-propelled rocket engines, the growing demand for engines that can be reliably reignited in space means that the transient phases such as start-up and shutdown must the better understood. For instance, the phenomenon of high-frequency combustion instabilities, which is particularly complex and critical for engine operation, can arise during these phases. In collaboration with CNES, research on this phenomenon is being conducted at ONERA and CORIA under subcritical injection conditions. These conditions are usually found during low-thrust operating regimes or during transient phases such as engine start-up and restart. Oxygen is injected in liquid state into the combustion chamber and undergoes a series of mechanisms: dense jet atomization, fragmentation of liquid ligaments, droplet evaporation, and turbulent combustion. Under these conditions, the combustion process is mainly driven by the atomization of the liquid oxygen, which must be accurately reproduced by simulation to better understand its role in the onset of combustion instabilities.

Before using simulation as an autonomous tool to study the atomization process, it is necessary to ensure its level of accuracy. This requires conducting experimental test campaigns on test benches capable of reproducing conditions representative of rocket engines, such as the MASCOTTE test-bench at ONERA or the MARACA test-bench at CORIA. The goal of these studies is to characterize the atomization process and provide experimental data that can be used to develop and validate numerical models. The experimental study of primary atomization of liquid oxygen, in particular, relies on flow visualization techniques that depict the liquid structures involved in the process. The primary atomization process observed in liquid rocket engines can be categorized as textural or structural, depending on the scale at which the atomization takes place. Textural atomization processes are characterized by thin ligaments being peeled from the jet, while structural atomization is related with the breakup of the liquid bulk. Visualizations resulting from experimental test campaigns show very complex two-phase flows involving textural liquid systems that are difficult to characterize due to the wide

range of spatial and temporal scales involved. To this day, no techniques are available to describe quantitatively the liquid ligaments involved in the textural atomization processes observed experimentally.

The main goal of this thesis is therefore to develop a methodology capable of characterizing the textural primary atomization processes observed in the two-phase-flow conditions representative of those encountered in liquid rocket engines. Based on a multi-scale approach developed at CORIA, this methodology aims at describing the textural liquid structures involved in the textural atomization process in their entire spatial scale range. This characterization should also provide information for the development of numerical primary atomization models. Additionally, the application of the methodology to liquid systems depicted by visualizations extracted from numerical simulations should allow to validate the simulation results in terms of the correct reproduction of the liquid structures that participate in the textural atomization process.

This thesis is organized in five chapters. In Chapter 1, the work is contextualized within the liquid rocket propulsion research. The main processes involved in liquid rocket engine operation are discussed, and an emphasis is given to the research on the atomization of liquid propellants. The main physical processes involved in rocket engine atomization are described and some of the most relevant works from the literature are introduced. The chapter ends with a discussion on academic and industrial requirements as well as on the identified gaps in the current research on liquid rocket engine atomization.

Chapter 2 deals with the multi-scale approach proposed at CORIA and developed in this thesis to describe the liquid structures involved in the atomization process. The theoretical aspects of the approach are first introduced. Secondly, an image analysis methodology is proposed to measure scale distributions of the visualized liquid systems. Lastly, the methodology is applied to an isolated liquid ligament, from a direct numerical simulation performed at ONERA, as it breaks up into droplets. This application gives insights into how the information on the size of the droplets produced by a ligament can be identified in the scale distribution of the ligament even before the breakup occurs.

Chapter 3 is dedicated to a presentation of the study configurations considered in this thesis. The atomization cases studied in this thesis correspond to two atomization processes showing textural features. The first application is a reactive, subcritical liquid oxygen-methane flow. A test campaign was designed and conducted during this PhD, and optical diagnostics were used to provide high-resolution visualizations of the small-scale textural liquid structures. Recorded images are presented and discussed to describe the cryogenic flame in conditions representative of real rocket engine combustion chambers. The second application is a non-reactive air-water configuration that was tested experimentally at CORIA and simulated numerically at ONERA prior to this thesis. The experimental and numerical approaches are introduced and the resulting visualizations, showing the presence of textural liquid structures, are discussed.

In Chapter 4 a methodology is proposed to allow the post-processing of the visualizations from Chapter 3, so that the multi-scale measurements presented in Chapter 2 can be applied to describe the small-scale textural ligaments observed. Then, the proposed post-processing technique is applied for the first time to images of a reactive configuration, and a qualitative description of the liquid-gas interface deformation is provided. Finally, a scale distribution is measured on the processed images and the smallest scale resolved by the methodology is identified.

The results of the application of the multi-scale measurement methodology developed in Chapters 2 and 4 are presented in Chapter 5. Scale distributions are measured and used to characterize the textural atomization process as a function of the distance to the injector and for the different operating conditions of the reactive configuration. A model is proposed to associate the textural ligaments with circular structures that are indicative of the drops that the ligaments will produce when they break up. Local size distribution of these structures are estimated to provide quantitative, local information about the process. The reported study constitutes a relevant work for the combustion and atomization communities and was published in an international peer review journal and presented in three international conferences. Finally, the multi-scale methodology is applied to the non-reactive configuration to compare results from a direct numerical simulation with the experimental visualizations. The goal of this comparison is to provide a method to validate results from numerical simulations in terms of the reproduction of the textural liquid structures involved in the primary atomization process.

Lastly, a general conclusion is presented and some of the future perspectives of the work are discussed.

Chapter 1

Context and literature review

This chapter dicusses the context of the work presented in this thesis. The main aspects involved in the research on liquid rocket propulsion are discussed. Then, the focus turns towards the atomization process. Its importance to the development and operation of liquid rocket engines is highlighted, and the main physical processes involved and their experimental investigation are described. Then, academic and industrial needs are discussed, including the development of primary atomization models. This discussion leads to the identification of gaps in the current research and the main objectives of the thesis are presented.

Contents

1.1 Liquid rocket propulsion

Rocket propulsion is the process of generating thrust to propel a rocket forward by expelling exhaust gases at high speeds through a nozzle. It enables spacecraft to overcome Earth's gravity and navigate through space. Unlike in atmospheric flight, space propulsion requires both fuel and oxidizer to be brought on board, as there is no atmospheric oxygen to support combustion.

There are two main types of rocket propulsion systems: liquid propulsion and solid propulsion. Solid propulsion, characterized by its simplicity and reliability, uses a premixed combination of fuel and oxidizer in a solid form. This type of propulsion is especially useful in applications that require rapid and powerful thrust, such as military missiles and the initial stages of launching spacecraft into orbit. In liquid propulsion, the fuel and oxidizer are stored separately and combined in a combustion chamber to generate thrust. This separation allows for precise control over the engine's power, enabling gradual adjustments crucial for tasks such as maintaining stable orbits, conducting interplanetary journeys, and executing complex maneuvers in space. The ability to throttle, shut down, and restart liquid engines provides flexibility, making them essential for new space missions.

1.1.1 Cryogenic liquid propellants

Within liquid propulsion, cryogenic liquid rocket engines represent a significant advancement in technology. These engines use cryogenic propellants, such as liquid hydrogen, liquid methane, and liquid oxygen, which are stored at extremely low temperatures to maintain them in a liquid state. Cryogenic propellants offer higher efficiency and specific impulse compared to other liquid fuels, making them ideal for demanding space missions. The high energy content of liquid hydrogen, or the more easily storable liquid methane, combined with the oxidizing power of liquid oxygen, allows cryogenic engines to generate high levels of thrust while maintaining fuel efficiency.

Hydrogen has historically been the primary choice for cryogenic rocket propulsion due to its exceptionally high specific impulse, which translates to greater efficiency and performance in space missions. Its use in famous engines, such as the Space Shuttle's main engines and the upper stages of the Saturn V, has solidified the role of hydrogen role in space exploration. However, in recent years, methane has emerged as an increasingly interesting alternative. Methane offers several advantages over hydrogen, including easier storage and handling due to its higher boiling point, which is closer to that of oxygen compared to hydrogen. Methane is denser than hydrogen, and thus requires less tank volume for the same amount of energy. This allows to design smaller and lighter fuel tanks. Additionally, methane is less prone to leakage and is more readily available, which

is particularly valuable for future missions involving in-situ resource utilization on other planets, like Mars. As a result, new rocket designs, such as SpaceX's Raptor, Blue Origin's BE-4, or ArianeGroup's Prometheus engines, are increasingly favoring methane as a propellant.

1.1.2 Physical processes in liquid rocket engines

In a liquid rocket engine, the combustion of the propellants occurs in a combustion chamber, where several critical processes unfold under some of the harshest conditions in aerospace engineering. The main processes include:

1. Propellant Injection: Fuel and oxidizer are injected into the combustion chamber through precise injector elements, ensuring the correct mixture and velocity ratios for optimal combustion.
2. Atomization: The injected propellants are atomized into fine droplets, enhancing the surface area available for the combustion reaction.
3. Evaporation: The atomized fuel and oxidizer rapidly evaporate, transitioning from liquid to gas, which further facilitates the mixing process.
4. Mixing: The evaporated fuel and oxidizer are thoroughly mixed within the chamber to ensure a uniform and efficient combustion reaction.
5. Combustion: The mixed propellants ignite and burn at extremely high temperatures, often exceeding 3000°C, generating intense thermal stresses and high-pressure gases.

The pressure within these chambers can reach hundreds of atmospheres, imposing significant mechanical stress on engine components. Additionally, the high-speed flow of hot gases can erode and corrode the chamber's interior, necessitating materials that can endure extreme temperatures and aggressive chemical environments. The turbulent and dynamic nature of the combustion process further complicates the precise mixing of fuel and oxidizer. To mitigate these extreme conditions, engineers employ advanced cooling techniques, such as regenerative cooling, where the propellant itself circulates around the chamber to absorb heat before it enters the combustion zone. The combination of high temperatures, high pressures, and aggressive chemical interactions makes designing and maintaining liquid rocket engine combustion chambers a complex and demanding task, requiring cutting-edge materials and engineering solutions to ensure reliable performance and longevity.

1.1.3 Operating conditions

In rocket engines, propellants can be subject to subcritical, transcritical or supercritical conditions, depending on their temperature and pressure. Subcritical conditions occur when the pressure and temperature of the propellants are below their critical point, i.e. the temperature and pressure at which the propellant transitions to a supercritical state. (For instance, the critical pressures of oxygen and methane are approximately 50 bar and 46 bar respectively). In subcritical conditions, the propellants exist as distinct liquid and gas phases, and can therefore be managed separately and mixed before combustion. Atomization of the liquid propellant in subcritical conditions is crucial as it controls the combustion process by ensuring a fine dispersion of oxygen droplets, which facilitates efficient mixing and ignition. The atomization process is also essential for preventing combustion instabilities, as non-homogeneous droplet sizes can lead to uneven combustion and pressure oscillations within the chamber. Subcritical conditions are commonly found in low-thrust engines and during transient working regimes, such as engine start-up and restarts.

Supercritical conditions, on the other hand, occur when the pressure and temperature exceed the critical point of the propellant. At this state, the propellant does not distinctly separate into liquid and gas phases but instead exists as a supercritical fluid—a phase with properties of both liquids and gases. Supercritical fluids have higher density than gases and can diffuse more easily than liquids, which improves the efficiency of propellant delivery and combustion. In modern rocket engines, especially those using advanced propellants like liquid methane or hydrogen, operating in supercritical conditions can enhance engine performance by providing more efficient combustion and reducing the overall mass and complexity of the propulsion system. This approach is particularly valuable in high-performance engines where optimizing propellant efficiency and reducing engine size are critical.

Transcritical conditions occur when the pressure in the combustion chamber exceeds the critical pressure of the propellant, but the temperature is still below the critical temperature. In this regime, the fluid behaves in a complex manner: it is injected as a liquid but quickly transitions to a supercritical fluid as it is heated inside the chamber.

1.1.4 Injection configurations

In subcritical conditions, and depending on the engine design, the propellants might be injected into the combustion chamber in either liquid or gaseous phase. In regeneratively cooled engines, for example, the liquid fuel is used to cool the combustion chamber and the nozzle before injection. In this case, the fuel is vaporized and therefore injected into the combustion chamber as a gas. The oxidizer, on the other hand, is usually injected

as a liquid. The injection phase is critical to ensure a safe and efficient combustion of the propellants. Many different injector designs have been developed over the years.

- Showerhead injector: probably the simplest injector design, it consists of small holes arranged in a pattern, each injecting a stream of either fuel or oxidizer into the combustion chamber.
- Impinging jet injector: streams of propellants are injected at angles so that they collide (impinge) with each other in the combustion chamber. This impingement causes the atomization of the propellants into fine droplets. One famous example of rocket engine using impinging jet injectors is the F1 engine of the Saturn V rocket.
- Pintle injector: a central pintle (a needle-like component) is used. The pintle can move to vary the size of the orifice through which the propellants are injected. The propellants are injected through a gap that forms around the pintle, allowing for good control over the mixture ratio. This type of injector is useful for engine throttling. One example of engine using pintle injectors is the Apollo Lunar Module Descent Engine.
- Coaxial injector: this type of injector consists of two concentric tubes. One of the propellants flows through the inner tube and the other through the outer tube. The two propellants are injected simultaneously, and mix as they exit the injector. Coaxial injectors can provide high propellant flow rates and allows a precise mixing of the propellants. They are used in Ariane's Vulcain engine and in SpaceX's Merlin Engine, for example.
- Coaxial swirl injector: this technology adds a rotating (swirling) motion to either one or both propellant flows before they are injected. The addition of swirl can improve the atomization and the mixing of the propellants. This type of injector can be found in SpaceX's Raptor and in Ariane's HM-7 engines, for example.

This work presented in this thesis focuses on the atomization of propellants issuing from coaxial injectors, in subcritical conditions where the fuel and the oxidizer are injected as a gas and a liquid, respectively. This type of configuration is of academic and industrial interest since it allows for high performance and efficiency in a wide range of operating conditions.

1.2 Coaxial assisted atomization: experimental and numerical investigation

The atomization process refers to the deformation and the breakup of a liquid flow, ejected from an orifice into a gaseous medium, into liquid fragments. The process stops

once the resulting liquid fragments are sufficiently small so that surface tension forces acting on their interface are strong enough to prevent further fragmentation. At this point the small liquid fragments assume the shape of spherical droplets. The ensemble of droplets produced by the atomization process is referred to as a spray.

The coaxial assisted atomization process, shown schematically in Figure 1.1 refers to the breakup of the liquid oxygen cylindrical jet injected through a central circular tube at relatively low velocities, with the aid of a surrounding higher-velocity gaseous fuel flow injected through an annular slit.

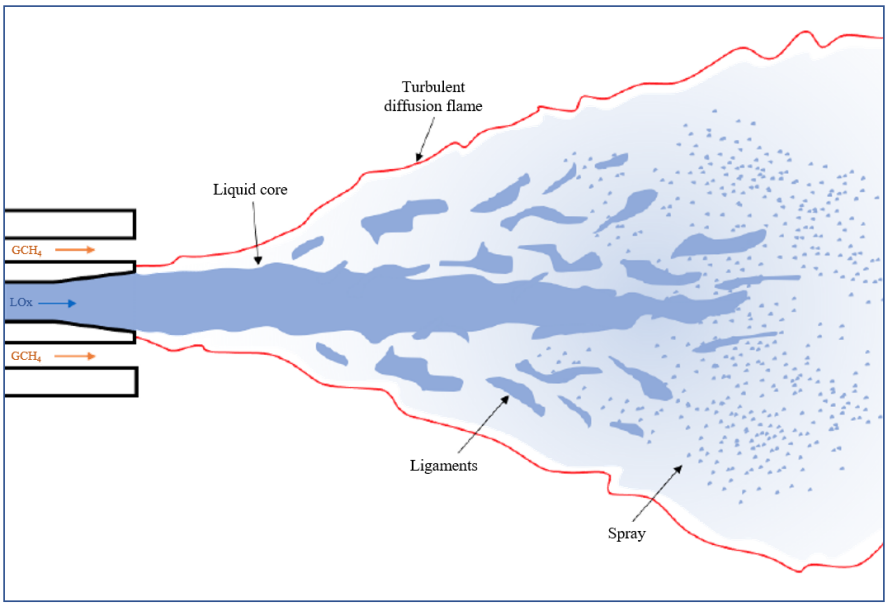

FIGURE 1.1: Schematic representation of the coaxial atomization process in a reactive flow representative of liquid rocket engines. Adapted from Lechner [2024].

1.2.1 Dimensionless numbers

The liquid and gas flows are characterized by their own respective average velocities, U_l and U_g, as well as by certain dimensionless numbers. These dimensionless numbers characterize the liquid and gas flows as well as their interaction during the combustion and atomization processes. The most relevant dimensionless numbers for the study of assisted atomization are presented below.

Reynolds number

The Reynolds number (Re) expresses the ratio between the inertial forces and the viscous forces in a fluid flow. Since the assisted atomization process involves a liquid and a gaseous flow, the Reynolds number is defined for each phase as:

$$Re_l = \frac{\rho_l U_l L_l}{\mu_l} \tag{1.1}$$

and

$$Re_g = \frac{\rho_g U_g L_g}{\mu_g}, \tag{1.2}$$

where the subscripts l and g represent the liquid and gaseous phases, respectively. ρ is the density of the fluid, μ its dynamic viscosity, and U its average velocity. L represents a characteristic length which, in the context of assisted atomization, is usually taken as equal to the diameter of the injector orifice.

The Reynolds number is commonly used in fluid mechanics to determine the flow regime: laminar, transitional or turbulent. In general, the higher the Reynolds number, the higher is the amount of turbulence in the flow.

Weber number

In two-phase flows, the Weber number (We) expresses the relative importance of the inertial forces compared to the surface tension forces at the interface. It is defined for each phase as:

$$We_l = \frac{\rho_l U_l^2 L_l}{\sigma} \tag{1.3}$$

and

$$We_g = \frac{\rho_g U_g^2 L_l}{\sigma}, \tag{1.4}$$

where σ is the surface tension of the liquid phase in the gas. In some contexts, a relative Weber number can be used. It considers the relative velocity between the liquid and gaseous phases and is defined as follows:

$$We_R = \frac{\rho_g (U_g - U_l)^2 L_l}{\sigma} \tag{1.5}$$

The Weber number is important to the study of atomization since it relates the stabilizing effect from surface tension with destabilizing effects from the inertial forces in the flow. The higher the Weber number, the higher the dominance between the destabilizing forces over the stabilizing ones. This leads to higher a deformation of the interface, consequently facilitating the atomization process.

Ohnesorge number

The Ohnesorge number (Oh) relates the viscous forces to the combined effects of inertial and surface tension forces in a flow, and is defined as:

$$Oh = \frac{\mu_l}{\sqrt{\rho_l \sigma L_l}} \tag{1.6}$$

It can also be expressed in terms of the Reynolds and Weber numbers as:

$$Oh = \frac{\sqrt{We_l}}{Re_l} \tag{1.7}$$

In general, low Ohnesorge numbers correspond to flows dominated by inertial and surface tension effects, facilitating the breakup of the liquid into droplets. High Ohnesorge numbers on the other hand correspond to flows where viscous forces dominate, leading to more stable flows less prone to undergo breakup.

Momentum flux ratio

The momentum flux ratio (J) is defined as the ratio between the momentum flux of the gas flow and that of the liquid flow:

$$J = \frac{\rho_g U_g^2}{\rho_l U_l^2} \tag{1.8}$$

The momentum flux ratio is commonly used in the study the primary atomization of assisted liquid jets. In general, a high momentum flux ratio means that the gas flow has much more momentum compared to the liquid. In this case, the primary atomization process tends to be enhanced due to the interaction between the two flows. The opposite is true for low momentum flux ratios, where the effect of the gas flow is less significant for the atomization process.

Mixing rate

The mixing rate (M) is defined as the ratio between the mass flow rate of the liquid flow and that of the gas flow:

$$M = \frac{\dot{m}_l}{\dot{m}_g} = \frac{\rho_l U_l A_l}{\rho_g U_g A_g} \tag{1.9}$$

where A is the cross-sectional area of the injector orifice. The mixing rate is commonly used to characterize the completeness of the combustion process in in reactive flows. Mixing rates lower than at stoichiometric conditions correspond to fuel-rich mixtures, while mixing rates higher than stoichiometry correspond to oxidizer-rich, or lean mixtures. The closer the mixing rate is to stoichiometry, the more complete is the combustion of the propellants.

1.2.2 Primary and secondary breakup

The desintegration of the liquid flow usually occurs in two main stages. First, the injected liquid flow is deformed by perturbations which can grow and eventually lead to the formation of liquid structures that detach from the main liquid bulk. Once these liquid fragments are detached, they may continue to deform and desintegrate into smaller and smaller fragments until reaching an equilibrium point where fragments become small spherical droplets. The first stage of the process is usually referred to in the literature as the primary atomization process [Dumouchel, 2008], whereas the second stage is referred to as the secondary atomization process [Guildenbecher et al., 2009].

Primary atomization studies in the literature report two main droplet production mechanisms. Some of the liquid fragments are produced as a result of the peeling of the interface, while others are produced from the breakup of the liquid bulk itself. The first mechanism depends on local characteristics of the liquid-gas interface and usualy results in liquid fragments of sizes far smaller than that of liquid bulk characteristic scale. The second mechanism depends mostly on global characteristics of the flow and tends to produce larger fragments, of sizes closer to the characteristic scale of the liquid bulk. Inspired by Kaye [1994] who proposed introduced a textural and structural fractal dimension to describe the tortuosity of the boundary of a system, Dumouchel et al. [2019] proposed to refer to the first and second droplet production mechanisms as *textural* and *structural* atomization processes, respectively.

Textural breakup processes are associated with an increase in the tortuosity of the liquid-gas interface. This increase in tortuosity is usually related to the formation of liquid ligaments at the interface. The formation of ligaments can arise from different processes. One source is the development interfacial instabilities such as the Rayleigh-Taylor instabilities, which produce streamwise ligaments on the interface of assisted liquid jets. However, most sources of ligament formation are linked with the characteristics of the injected liquid flow. Dumouchel et al. [2019] reported a cavitation-induced textural atomization process and found that the characteristics of the textural ligament scale distribution correlate with the liquid flow cavitation number. Grout et al. [2007] characterized the interface tortuosity caused by the formation of ligaments with a textural fractal dimension. This fractal dimension was found to correlate with the liquid Reynolds number of the injected flow. In their investigation on non-turbulent round jets, Wu et al. [1995] reported a textural atomization process where textural ligaments were triggered by the boundary layer developed in the injector. The size of the droplets produced by these textural ligaments was found to correlate with the thickness of this boundary layer. Wu and Faeth [1993], Wu et al. [1992, 1995] also reported textural breakup processes on turbulent round jets, where the size of the droplets produced by the textural ligaments were found to relate with the local turbulent scales of the liquid flow.

1.2.3 Assisted atomization regimes

In their experimental investigation on coaxial air-water jets, Chigier and Farago [1992] proposed a morphological classification of coaxial assisted jet breakup based on Re_l and We_R. Hopfinger [1998] added that a classification of atomization regimes should also account for the momentum flux ratio J. The author introduced a breakup regime classification diagram, based on Re_l, We_g and J, which was later completed by Lasheras and Hopfinger [2000] and Baillot et al. [2009] and is shown in Figure 1.2.

Baillot et al. [2009] identified five main atomization regimes. These regimes are visualized in Figure 1.3 and described below.

- Axisymmetric Rayleigh regime: observed at low values of Re_l and We_g in the diagram, this regime is characterized by a cylindrical liquid jet that remains largely axisymmetric as it travels. At this regime, aerodynamic forces are minimal, and the breakup is primarily driven by capillary instabilities. The droplets produced are relatively uniform in size and their diameter is of the order of that of the liquid jet.

- Non-axisymmetric Rayleigh regime: similar to the previous regime, the non-axisymmetric Rayleigh regime occurs when the gas-flow velocity is increased, leading to higher aerodynamic effects on the liquid. The result is a liquid jet that no longer maintains its axisymmetric shape and that produces droplets of less uniform sizes and smaller diameters compared to the axisymmetric regime.

- Shear breakup regime: this regime occurs when the gas velocity is increased further, leading to the development of a shear instability at the liquid-gas interface. These shear instabilities may lead to the creation of some ligaments due to the development of a Rayleigh-Taylor transverse instability, but this process is quickly damped by a capillary instability that produced droplets of diameters of the order of the jet diameter.

- Membrane regime: in this regime, the aerodynamic effects are strong enough to curve the liquid jet, as seen in Figure 1.3. The gas flow impacts on the liquid jet, which leads to the creation of membrane-like liquid structures. These membranes then breakup into small droplets of various sizes.

- Fiber-type regime: occurring at high values of Re_l and We_g, this regime is characterized by the formation of very thin liquid ligaments (fibers) at the jet interface. These ligaments are quickly atomized by the gas flow into very small liquid structures, while the remaining liquid core breaks up into larger structures along the injection axis. This is the breakup regime usually found in the atomization of liquid oxygen in liquid rocket engines.

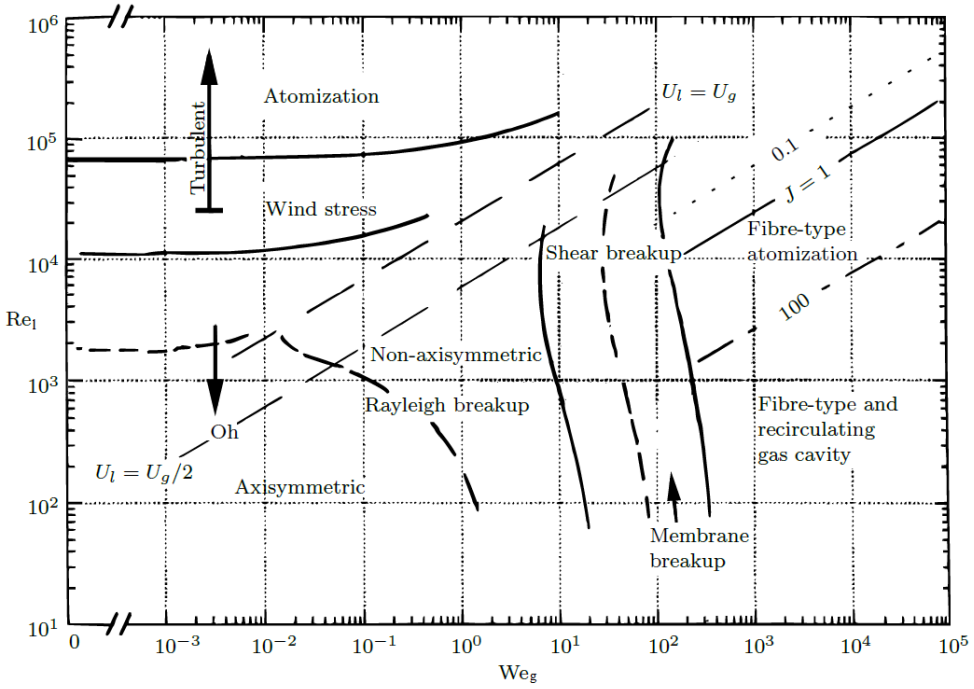

FIGURE 1.2: Assisted atomization regime classification diagram based on Re_l, We_g and J from Lasheras and Hopfinger [2000] and Baillot et al. [2009].

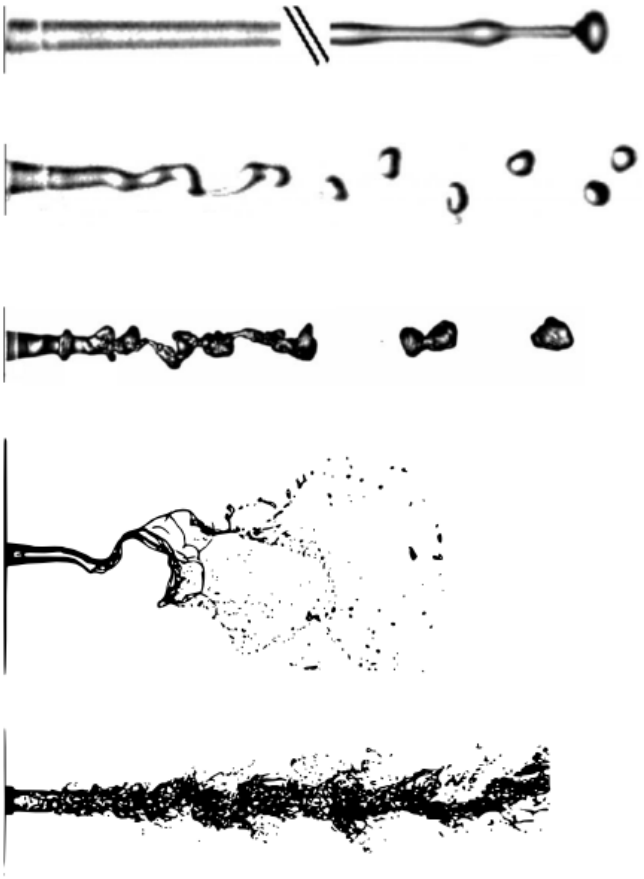

FIGURE 1.3: Visualization of the main atomization regimes identified by Chigier and Farago [1992] and Baillot et al. [2009]. From top to bottom: axisymmetric Rayleigh regime, non-axisymmetric Rayleigh regime, shear breakup regime, membrane regime, fiber-type regime.

1.2.4 Macroscopic quantities

Most studies on fiber-regime assisted atomization processes rely on descriptions based on global measurements of the liquid atomizing flow. These global measurements usually include macroscopic quantities such as the length of the liquid core and the angle between the cone formed by the spray of droplets and the injection axis. These measurements are widely used in industrial studies since they allow to study the effect of specific parameters related to the liquid and gas flows themselves or to other parameters that might influence the atomization process such as the combustion of propellants in liquid rocket engines.

1.2.4.1 Liquid core length

One of the main macroscopic characteristics describing a coaxial atomizing jet is the length of the liquid core; L_c. This quantity is defined by Porcheron et al. [2002] as the

length of the main liquid structure attached to the injector, which may include ligaments and gas inclusions. The liquid core length is an important information for the design of combustion chambers since it is linked with the lenght of the flame that surrounds the atomizing liquid jet.

Many studies in the literature have reported measurements of the liquid core length of non-reactive coaxial atomizing jets and proposed correlations between this length and some of the main dimensionless numbers characterizing the atomization process. Eroglu et al. [1991] measured the liquid core length on shadowgraph images considering injection conditions associated with membrane- and fiber-type atomization regimes. The authors proposed a correlation, shown in Table 1.1, that depends on the liquid injector diameter D_l and on We_R and Re_l. Woodward et al. [1994] proposed a correlation based on measurements of the liquid core length made images of the X-ray transmitted intensity through the two-phase flow field. The correlation, shown in Table 1.1, relates the liquid core length with the density ratio ρ_g/ρ_l, as well as We_R, Re_l and a parameter Z that considers the ratio of the specific heat of the fluids and the gas-constant. Porcheron et al. [2002] measured the liquid core length using a optical fiber probe measurement capable of detecting the presence of either liquid or gas phases due to the variation of the refractive index of the fluid in contact with the probe. The resulting signal allowed to report the liquid presence probability. The liquid core length was defined as the farthest downstream position where the liquid presence probability was equal to 0.5. A correlation, shown in Table 1.1, was found to relate the liquid core length with the density ratio ρ_g/ρ_l, with the Ohnesorge number Oh and with the momentum flux ratio J. Leroux et al. [2007] measured L_c on shadowgraph images and proposed a correlation, shown in Table 1.1, where the length of the liquid core depends mainly on the momentum flux ratio J. Davis and Chehroudi [2007] proposed a correlation, shown in Table 1.1, based on measurements of L_c made on backlit images of subcritical atomizing liquid jets. Similarly to the correlation from Leroux et al. [2007], this correlation states that the liquid core length depends mostly on the momentum flux ratio.

Table 1.1: Liquid core length correlations from the literature

Eroglu et al. [1991]	$\frac{L_c}{D_l} = 0.66 We_R^{-0.4} Re_l^{0.6}$
Woodward et al. [1994]	$\frac{L_c}{D_l} = 0.095 \left(\frac{\rho_g}{\rho_l}\right)^{-0.36/Z} We_R^{-0.22/Z} Re_l^{0.68}$
Porcheron et al. [2002]	$\frac{L_c}{D_l} = 2.85 \left(\frac{\rho_g}{\rho_l}\right)^{-0.38} Oh^{0.34} J^{-0.13}$
Leroux et al. [2007]	$\frac{L_c}{D_l} = 10 J^{-0.3}$
Davis and Chehroudi [2007]	$\frac{L_c}{D_l} = 25 J^{-0.2}$

Investigations on the coaxial atomization of liquid oxygen in subcritical reactive conditions representative of those found in liquid rocket engines reported measurements of the liquid core length made on shadowgraph images. The reported measurements are in

good agreement with the correlation from Davis and Chehroudi [2007] in the cases of liquid oxygen-methane flames Yang et al. [2007] and liquid oxygen-hydrogen flames Fdida et al. [2013]. This agreement seems to confirm that the liquid core length is controlled by the momentum flux ratio in the subcritical regimes considered.

1.2.4.2 Spray cone angle

Another global characteristic of the atomization process that is important in the design of combustion chambers is the spray cone angle. This quantity is defined as the maximum angle formed between the injection axis and cone formed by the droplets produced by the atomization of the liquid jet. In their work on the atomization of non-reactive coaxial assisted liquid jets, Lasheras and Hopfinger [2000] propose an expression of the spray cone angle θ considering the growth rate of the liquid-gas mixing layer, which is itself related to the liquid core length L_c. Valid for $J < 30$ and $\theta < 40\,\text{deg}$, the expression writes:

$$\theta = tan^{-1}\left(\frac{J^{0.5}}{6}\right) \tag{1.10}$$

Leroux et al. [2007] proposed an expression obtained from a linear stability analysis for the fiber regime which writes:

$$\theta = 2tan^{-1}\left(\frac{0.75J^{0.5}(1-0.1J^{0.5})}{0.06J+J^{0.5}+1}\right) \tag{1.11}$$

1.2.5 Numerical simulation of primary atomization

The numerical simulation is a precious tool in the study of atomization processes and of their interaction with other physical processes. In the case of liquid rocket engines, experimental studies face several challenges, among which are the cost of full-scale experiments, the limited amount of data that the extreme conditions found inside the combustion chamber impose on measurements, etc. The numerical simulation appears therefore as a solution that can allow for more detailed information on some of the main processes involved, at costs that allow for parametric and full-scale studies.

In order to provide realistic results capable of complementing or even replacing some of the experimental measurements, numerical simulations must be capable of accuratly reproducing the main physical processes in the flow. The simulation of primary atomization in the fiber regime faces challenges related to the wide range of temporal and spatial scales involved in the process. Figure 1.4 illustrates these challenges on an experimental visualization of the fiber-regime atomization of a LOx-H_2 coaxial jet. For

instance, the spatial scales involved in the process range from the size of the liquid core, which can reach lengths of the order of tens of milimiters, all the way to the size of the smallest droplets produced which can be of the order of a few micrometers. Therefore, a complete solution of the governing equations for all scales involved requires a very large amount of computational resources, which are usually prohibitive in the context of real, engine-like applications.

A usuefull classification of zones within a two-phase flow is given by Ishii and Hibiki [2010]. As illustrated in Figure 1.4 by the highlighted zones, the two-phase flow is classified accoring to the geometry of the interface into three classes: a separated phases flow, a mixed flow and a dispersed phase flow. In the separated phases zone, the liquid phase is found in a dense, continuous shape. The atomization process causes this continuous liquid phase to breakup into ligaments and droplets in the mixed zone. As these ligaments and droplets continue to breakup into smaller and smaller droplets, which disperse through the gas phase, in the so-called dispersed phase.

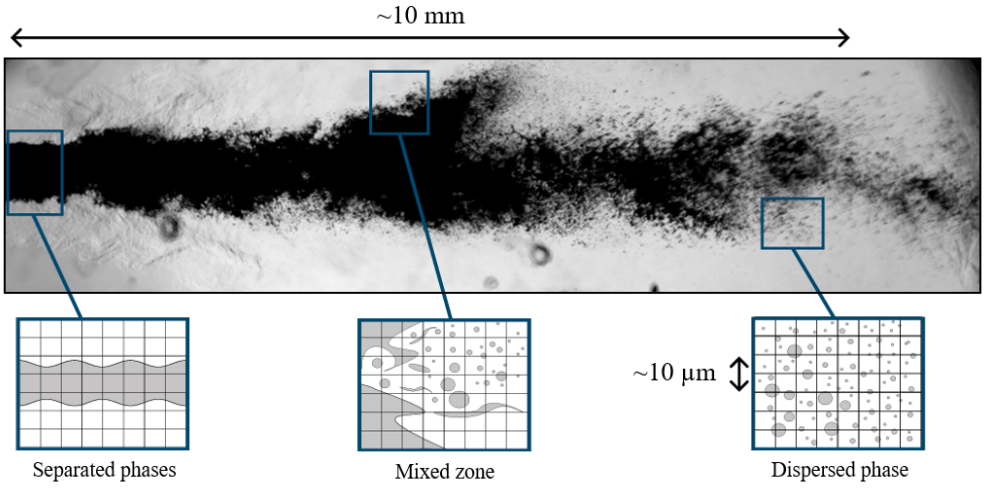

FIGURE 1.4: Identification of the separated phases zone, the mixed zone and the dispersed phase zone in a LOx-CH_4 fiber-regime atomization process during combustion in the MASCOTTE test-bench [Fdida et al., 2019]. Adapted from Granger [2023].

Numerical simulations of atomizing flows usually include the solution of the Navier-Stokes equations. The most widely used approaches differ mainly on how the turbulence of the flow is treated. The Direct Numerical Simulation (DNS) resolves all scales of turbulence without any modeling assumptions, making it the most precise but also the most computationally demanding method. Reynolds-Averaged Navier-Stokes (RANS) models, on the other hand, focus on averaging the effects of turbulence, providing a computationally efficient method at the expense of accuracy. A middle ground is obtained considering Large-Eddy Simulations (LES). In this approach, the larger turbulent structures are resolved while the smaller scales are modeled. Figure 1.5 schematizes the turbulent energy cascade which describes the energy transfer between the large turbulent eddies which carry the most amount of energy into smaller and smaller eddies until

reaching very small scales where the turbulent energy is dissipated. Figure 1.5 also indicates the range of scales resolved and modeled by each of the simulation approaches mentioned above. The LES approach resolves turbulent structures of scale larger than a cut-off scale $1/\kappa_c$, while smaller structures are modeled. In this case, the resolution of the large turbulent scales relies on the spatial filtering of the Navier-Stokes. This filtering is usually imposed by the size Δ of the cells in the mesh, so that $\Delta = 1/\kappa_c$.

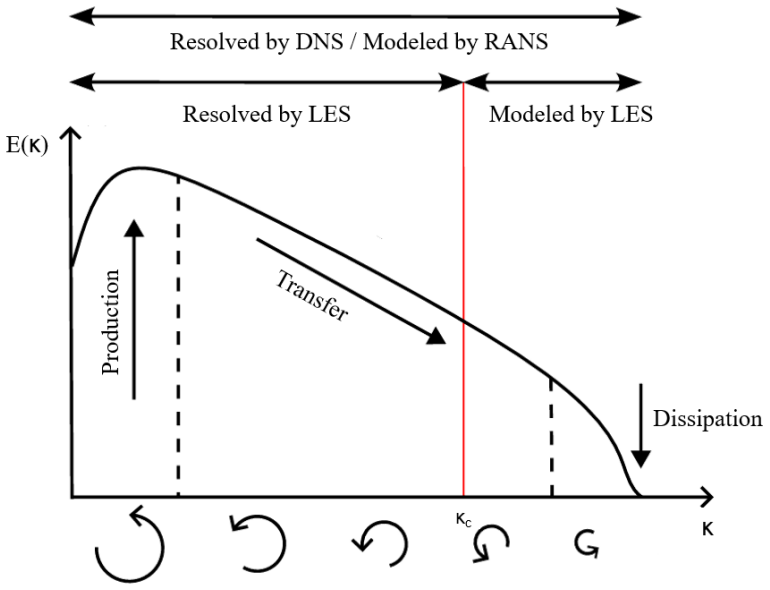

FIGURE 1.5: Turbulent energy cascade proposed by Kolmogorov. Adapted from Granger [2023].

Complex flows such as the ones found in liquid rocket engines involve strongly unstationary processes. RANS approaches are therefore considered unfit for most applications. DNS approaches, while capable of reproducing the entire range of turbulent scales and therefore yielding the most accurate results, is computationally costly. Its use is therefore mostly reserved for academic scenarios involving small flow domains. The most widely used approach for the simulation of complex two-phase flows representative of real applications such as liquid rocket engine atomization is the LES approach. Thus, much of the research on primary atomization focuses on the development of LES models to allow relatively fast but accurate simulations of this type of flow.

1.2.5.1 Two-phase flow simulation approaches

The simulation of two-phase flows requires the consideration of forces related to the presence of an interface between the two phases. The adequate capture of the dynamics of the liquid-gas interface is one of the main challenges in the simulation of this type of flow. Different approaches can be used to simulate two-phase flows depending on the characteristics of the interface structure shown in Figure 1.4. Four main approaches

can be identified: *interface capturing methods*, which allow to describe the entire flow including both the separated phases and the dispersed phase zones, at the cost of high computational cost. This approach uses interface reconstruction methods to capture the precise position of the interface. *Diffuse interface methods* [Le Touze et al., 2020], which are used to describe the separated phases zone at lower computational costs. In this approach, the interface is simulated with the help of a phase indicator function, i.e. the volume fraction α_k of each phase. Cells where both the liquid and the gas are present are part of the interface, which can diffuse over multiple cells; *statistical* or *kinetic methods*, which are used to describe the dispersed phase zone of the flow. In this approach, the liquid droplets are considered as spherical particles dispersed in the gas phase. The droplets interact with each other and with the gas phase, and their macroscopic behavior is described by the kinetic *Williams-Boltzmann* equation [Williams, 1958]. For more details, refer to Le Touze [2015] and references therein. The fourth approach considers a coupling of the three approaches listed above to simulate different zones of the flow. This is the approach chosen at ONERA to simulate the complex, reactive flows found in liquid rocket engines in a LES framework.

1.2.5.2 LES simulation strategy at ONERA

As described previously, complex flows such as the atomization of liquid jets in the fiber regime found in liquid rocket engines include a wide range of time and spatial scales, including different flow topologies as shown in Figure 1.4. Interface reconstruction methods, while very precise, particularly for separated phases, are not well suited for the dispersed phase nor for potential coupling with a kinetic method to resolve it. Kinetic methods on the other hand are very well suited for resolving the dispersed phase, but since they do not consider separated phases, they do not allow for the simulation of the mixed zone or the transition to the separated phase. Finally, diffuse interface methods allow for the description of the large scales of the liquid core if the diffusion is numerically controlled, and are suitable for modeling a transition to a dispersed phase. Considering an atomizing flow resolved on a LES-type mesh, where the mesh size is much larger than the smallest droplets, the diffuse interface solution distributes the liquid mass across a set of cells with a low volumetric presence of liquid. This approaches the assumptions of a dispersed phase flow, which favors a transition to this type of modeling.

Therefore, a simulation methodology combining different approaches was established at ONERA by Le Touze [2015] and later used by Rutard [2019] and Granger [2023] to simulate the fiber-regime atomization process in rocket engine-like conditions. The proposed coupled simulation strategy combines a diffuse interface method to describe the separated phases as well as the mixed zone, and a kinetic method is used to simulate the dispersed phase. This approach was implemented in ONERAS's multi-physics simulation code CEDRE using a separated phases solver (SPS) called CHARME and a dispersed

phase solver (DPS) called SPIREE. The transfer of fluid (mass, momentum, and energy) between the SPS and DPS solvers is achieved through source terms in the equations. These source terms must account for the primary atomization process, simulating the corresponding transfer of mass of the liquid phase from the SPS to the DPS in the shape of spherical droplets.

The modeling of the primary atomization process is therefore achieved in the transfer of mass from the liquid phase of the SPS to the DPS by the introduction of a corresponding source term in the equations. Once the mass of liquid representing the primary atomization is transfered from the SPS to DPS, it must be modeled as a spray of spherical droplets whose initial size, velocity and temperature distributions must still be defined. As Figure 1.6 illustrates, the ensemble of droplets can characterized alternatively by:

(a) Imposing average properties that are uniform throughout the domain and constant over time. This is the simplest case, where global flow quantities (We, Re, ...) and/or experimental correlations can be used to determine the average characteristics of the spray.

(b) Imposing distributions that are uniform throughout the domain and constant over time. This approach is similar to the previous one but considers a distribution of variables around the average.

(c) Imposing average properties that are dynamic and depend on the local flow conditions.

(d) Imposing dynamic distributions that depend on the local flow conditions.

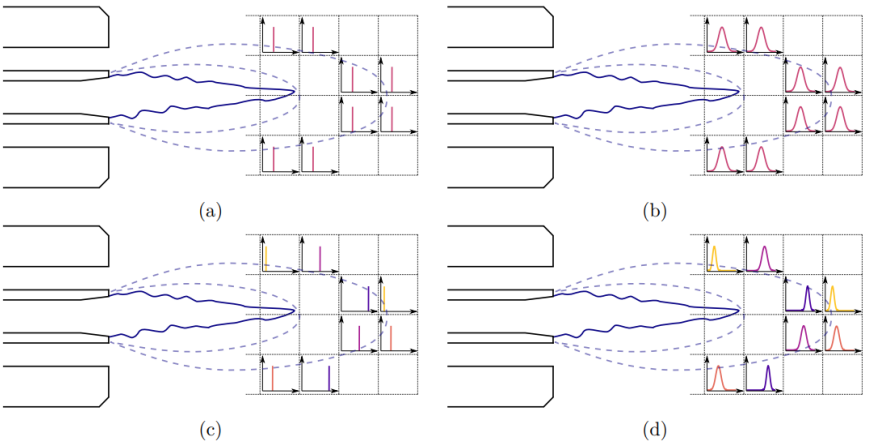

FIGURE 1.6: Illustration of the possible characteristics of the properties of the modeled primary atomization droplets transfered to the DPS solver: (a) uniform and constant averages; (b) uniform and constant distributions; (c) dynamic averages; (d) dynamic distributions.

Le Touze [2015] and Rutard et al. [2020] simulated fiber-regime atomization processes considering the modeling described above, using the simplest of the models for the properties of the primary droplets issuing from the SPS. In this case, a constant and uniform average value for the diameter, the velocity and the temperature of the droplets is imposed in all of the cells where the mass transfer occurrs.

An improvement to the primary atomization modeling from Le Touze [2015] was proposed recently by Granger [2023], who introduced a interface area density model for the LES simulation of a fiber-regime atomization process. The method is based on the developments of Chesnel et al. [2011] and includes the transport of a subgrid interface area density with an advection equation, while opportune source terms to simulate its growth by fragmentation or its reduction by coalescence effects are modeled. The interface area density Σ is defined as the ratio between the interface area and the volume of the cell where it is contained. Together with the liquid volume fraction α_l from the diffuse interface approach used to simulate the separated phases in the flow, the interface area can be used to determine an equivalent Sauter diameter as:

$$D_{32} = \frac{6\alpha_l}{\Sigma} \tag{1.12}$$

In this case, a local mean diameter is determined based on the local characteristics of the flow. This allows to improve the primary atomization model from Le Touze [2015] where a uniform and constant average diameter is imposed for all droplets transfered to the DPS (Figure 1.6(a)) by instead considering a dynamic average diameter (Figure 1.6(c)).

1.3 Research gap and thesis objectives

As discussed in this chapter, the experimental description of the fiber-regime assisted atomization of liquid jets in conditions found inside the combustion chamber of liquid rocket engines is mostly based on the measurement of macroscopic quantities such as the liquid core length or the spray angle. These measures, altought useful for the design of engines, do not provide sufficient detail for the description of droplet production processes. Other, more detailed quantities, such as the average ligament size or the average drop size issuing from ligament breakup, can be estimated from correlations involving properties of the flow at injection.

Even if they allow rough estimations of the scales involved in the atomization process, none of these quantities allow to describe the textural atomization process locally and quantitatively. Furthermore, the numerical simulation of representative industrial atomization processes requires the use of primary atomization models that must impose the initial sizes of the primary droplets produced in the process. To this day, only average

droplet sizes are considered. A more detailed characterization of the primary droplets produced by the textural atomization process is therefore required. The goal of this thesis is therefore to provide a methodology capable of providing a local characterization of the small-scale ligaments visualized in textural atomization processes and to provide an estimation of the local diameter distribution of the main primary drops produced.

The methodology proposed in this thesis aims at describing the textural atomization process based on a multi-scale description, which is presented in detail in Chapter 2. The representation of the ligaments in the scale space includes all information relative to their size, number and shape as a function of the position in the flow. This information can then be used to estimate the distribution of drops that are likely to produced by these ligaments. This methodology will then allow to study the influence of certain flow parameters on the textural atomization process, to improve the numerical modeling currently used in the simulation of such flows, or to validate simulation results in terms of the reproduction of the textural atomization process.

Chapter 2

Multi-scale description of atomizing jets

This chapter presents a multi-scale technique capable of describing the deformation of liquid-gas interfaces such as the ones encountered in atomization processes. The presentation starts with the theoretical aspects of the multi-scale description of liquid systems. These concepts are used to develop an image analysis technique capable of measuring scale distributions of liquid systems visualized on binary images. Then, the image measurement technique is used to describe a breakup process of a liquid ligament.

Contents

2.1 The multi-scale method

2.1.1 Definitions

The work presented in this thesis proposes the study of liquid systems based on a multi-scale description of the system's morphology. Any system in n-dimensional space can be described by a set of scalar geometrical measures. In two-dimensional (2D) space, a system of boundary, or interface, C can be described by its surface area S, its perimeter or interface length L, defined as:

$$L = \int_C dl \tag{2.1}$$

and its length-integrated curvature H, defined as:

$$H = \int_C \kappa \; dl \tag{2.2}$$

where κ is the local curvature of the system's interface. In 2D, the length-integrated curvature H of a system is proportional to its Euler characteristic χ ($H = 2\pi\chi$) [Mecke and Wagner, 1991]. χ is a topological invariant and is equal to 0 or 1 if the system is homeomorphic to an infinite 2D cylinder or to a disk, respectively. Two systems are considered homeomorphic with each other when they are topologically equivalent, i.e they have the same number of connected components and the same number of holes. Therefore any simply connected 2D system (i.e. a system whose boundary is path-connected, so that there is a continuous path between any two points on its boundary, and that shows no holes), such as squares, rectangles, or any polygon, is homeomorphic to a disk. On the other hand, in 2D, systems whose boundaries extend infinitely in one direction, such as any deformed infinite cylinder, do not form a connected system. If in addition they do not contain holes, they are homeomorphic to a cylinder. Figure 2.1 shows some examples of 2D systems homeomorphic to a 2D cylinder or to a disk.

The proposed multi-scale method, introduced by Dumouchel et al. [2008, 2019, 2022] considers these measures of the liquid system and of all the systems parallel to it in the liquid phase. A parallel system is a body whose boundary is parallel to that of the original system interface, at a given distance from it in the direction normal to the interface, as shown in Figure 2.2. These parallel systems can be obtained upon erosion operations on the original system. Erosion is a classical image analysis operation that

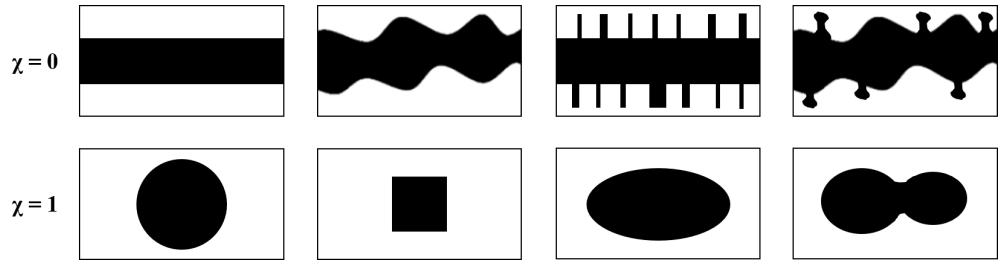

FIGURE 2.1: Examples of systems homeomorphic to a 2D infinite cylinder (top) and to a disk (bottom).

consists in removing from the system a region covered by a disk of diameter d that was dragged along the interface while keeping the disk center on the interface line. An erosion at scale d results in a parallel system at distance $d/2$ from the original interface (for example, a disk of diameter D eroded at scale d is a disk of diameter $(D–d)$). Figure 2.2 shows a schematic representation of a given system and of some of its parallel systems. For each parallel system, a surface $S(d)$, an interface length $L(d)$, and a length-integrated curvature $H(d)$ are defined.

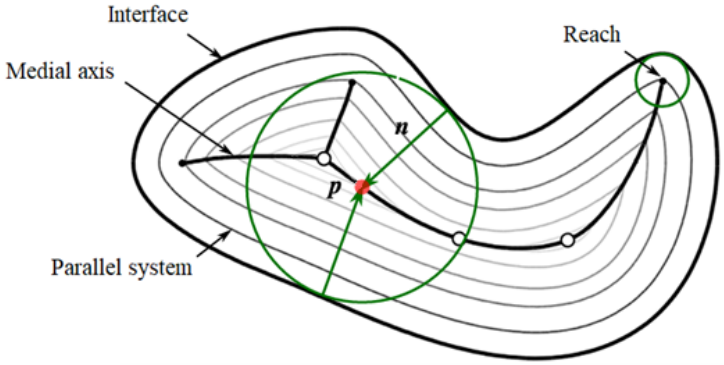

FIGURE 2.2: Schematic representation of a body and some of its parallel systems. Adapted from Dumouchel et al. [2022].

The multi-scale description of any given system relies on these measures of the original system and of the entire set of parallel systems obtained upon erosion at scales in the $[0,\ d_{max}]$ range. Here, d_{max} is defined as the smallest scale for which the system is completely eroded. $S(0)$, $L(0)$ and $H(0)$ characterize the original system.

The function $S(d)$ is used to construct a cumulative scale distribution $E_2(d)$ [Dumouchel et al., 2008, 2019], defined as:

$$E_2(d) = S(0) - S(d) \tag{2.3}$$

$E_2(d)$ starts at 0 when $d = 0$ and grows until $S(0)$ when $d = d_{max}$.

The derivative with respect to d (noted $(\cdot)_{,d}$) of $E_2(d)$ is called the scale distribution $e_2(d)$ of the system:

$$e_2(d) = E_2(d)_{,d} \tag{2.4}$$

These functions, $E_2(d)$, $e_2(d)$, and its derivative $e_2(d)_{,d}$ are related to $S(d)$, $L(d)$ and $H(d)$ respectively. $E_2(d)$ and $S(d)$ are directly related by definition, as seen in Equation 2.3. Dumouchel et al. [2022, 2023] show that the scale distribution $e_2(d)$ is equal to half of the interface length $L(d)$ of the parallel system at scale d:

$$e_2(d) = \frac{L(d)}{2} \tag{2.5}$$

The relation between $e_2(d)_{,d}$ and $H(d)$ depends on the eroded system at scale d. For small scales, the interface of the parallel system at scale d is smooth, meaning that it does not show any cusps, i.e. points where the interface shows a sharp corner with a discontinuity in its local curvature. In this case $e_2(d)_{,d}$ is proportional to $H(d)$. For larger scales, however, the interface of the parallel system is not smooth, and the equality does not hold. The scale delimiting these two situations is called the *reach* of the system and is noted as d_R.

To undertand what is the reach of a system, let us consider again the system in Figure 2.2. A point on the interface of a given parallel system might have more than one closest neighbor on the original interface. One example is point p shown in Figure 2.2. This point p is the center of a circle bi-tangent to the original interface, i.e. the circle is tangent to the original interface in at least two points. The set of points where this occurs forms the medial axis of the system (Lee [1982]). The smallest radius of the set of circles is equal to d_R. It is only for scales larger than d_R that the eroded systems show cusps on their interfaces (see Figure 2.2). The relation between $e_2(d)_{,d}$ and $H(d)$ can therefore be written as:

$$e_2(d)_{,d} = \begin{cases} \frac{H(d)}{4} & \text{if } d \leq d_R \\ \frac{H(d)}{4} + F(d) & \text{if } d > d_R \end{cases} \tag{2.6}$$

where d_R is the scale equal to the reach of the system, and $F(d)$ is a corrective function that depends on the shape of the system.

2.1.2 Applications

2.1.2.1 Cylinders and spheres

The $E_2(d)$, $e_2(d)$ and $e_2(d)_{,d}$ distributions of elementary bodies such as cylinders and spheres can be determined analytically. The 2D projection of a section of length L of an infinite cylinder of diameter D_c is a band of length L and width D_c, whereas that of a sphere of diameter D_s is a disk of the same diameter (as shown in the first column in Figure 2.1.).

From the definitions in Equations 2.3 and 2.5, the corresponding $E_2^c(d)$, $e_2^c(d)$ and $e_2^c(d)_{,d}$ distributions for a section of length L of an infinite cylinder of diameter D_c write:

$$E_2^c(d) = \begin{cases} Ld & \text{if } d < D_c \\ LD_c & \text{if } d \geq D_c \end{cases} \tag{2.7}$$

$$e_2^c(d) = \begin{cases} L & \text{if } d < D_c \\ 0 & \text{if } d \geq D_c \end{cases} \tag{2.8}$$

$$e_2^c(d)_{,d} = \begin{cases} 0 & \text{if } d \neq D_c \\ -\infty & \text{if } d = D_c \end{cases} \tag{2.9}$$

In the case of a sphere of diameter D_s, the corresponding $E_2^s(d)$, $e_2^s(d)$ and $e_2^s(d)_{,d}$ distributions write:

$$E_2^s(d) = \begin{cases} \frac{\pi}{4} d(2D_s - d) & \text{if } d < D_s \\ \frac{\pi}{4} D_s^2 & \text{if } d \geq D_s \end{cases} \tag{2.10}$$

$$e_2^s(d) = \begin{cases} \frac{\pi}{2}(D_s - d) & \text{if } d < D_s \\ 0 & \text{if } d \geq D_s \end{cases} \tag{2.11}$$

$$e_2^s(d)_{,d} = \begin{cases} -\frac{\pi}{2} & \text{if } d < D_s \\ 0 & \text{if } d \geq D_s \end{cases} \tag{2.12}$$

The theoretical distributions for the 2D projections of a cylinder and of a sphere, both of diameter D, are plotted in Figure 2.3. In each figure, the scale axis is normalized by the diameter D. In Figures 2.3a and 2.3b, the $E_2(d)$ and $e_2(d)$ distributions are normalized by the original system surface area $S(0)$ and interface length $L(0)$ respectively.

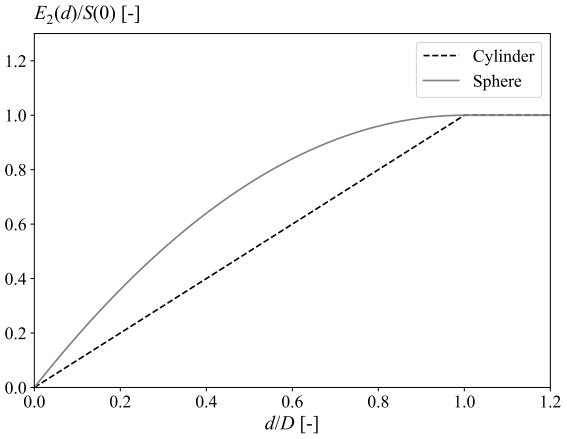

(a)

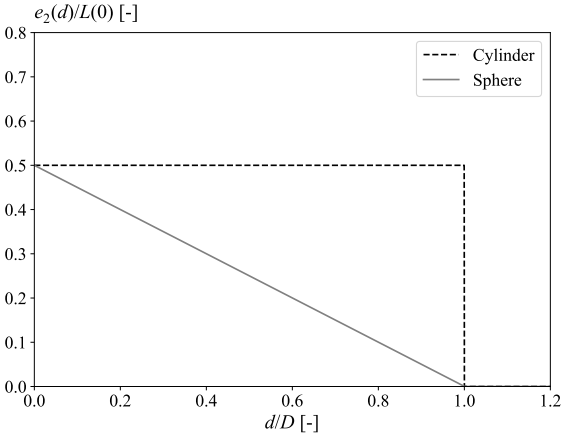

(b)

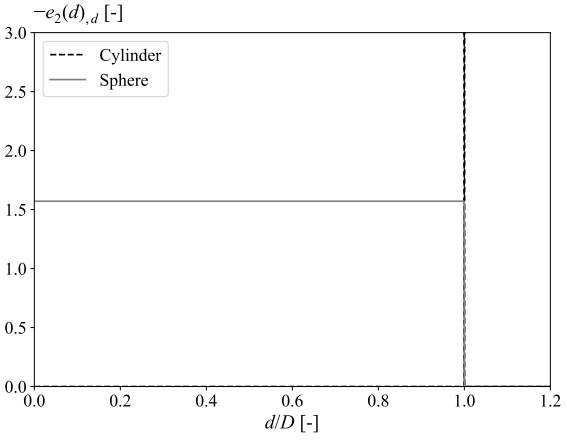

(c)

FIGURE 2.3: Theoretical scale distributions for a cylinder and a sphere: (a) cumulative scale distribution $E_2(d)$, (b) scale distribution $e_2(d)$ and (c) its derivative with respect to d, $e_2(d)_{,d}$.

2.1.2.2 Perturbed cylinder

Let us now consider the cylinder shown in Figure 2.4. The cylinder unperturbed radius is a, and its interface is deformed by a sinusoidal perturbation of amplitude η and wavelength λ (wave number $k = 2\pi/\lambda$). The parametric equation, in the (x,y) plane, of the position of the upper and lower interfaces writes:

$$y = \pm\left(a + \eta cos(kx)\right) \tag{2.13}$$

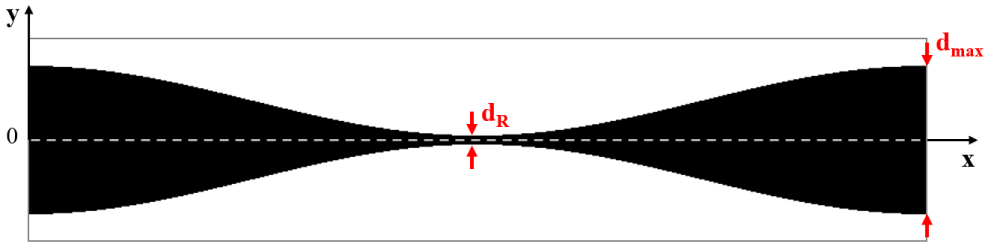

FIGURE 2.4: Perturbed cylinder

Two characteristic scales can be identified in the perturbed cylinder. The first, d_R, is the smaller diameter of the object and is located in the center of the contracted segment of the cylinder. The scale d_R is the reach of the system. The second characteristic scale, d_{max}, is the largest cylinder diameter, located at the swollen segment of the cylinder.

The theoretical scale distribution of the perturbed cylinder has been determined by Dumouchel et al. [2023]. The theoretical $e_2(d)_{,d}$ distribution can be written according to the following parametric expression:

$$\begin{cases} d = 2(a + \eta cos(kx))\sqrt{1 + (\eta k sin(kx))^2} \\ e_2(d)_{,d} = -\frac{1}{4}\left(n\pi + 2n\left[\frac{1}{\eta k sin(kx)} - arctan\left(\frac{1}{\eta k sin(kx)}\right)\right]\right) \end{cases} \tag{2.14}$$

where n is the number of cusps of the parallel system at scale d. By definition, $n = 0$ for $d < d_R$ and, in the case of the cylinder shown in Figure 2.4, $n = 2$ for $d \geq d_R$). Equation 2.14 is only valid if the cusps of the parallel systems all lie on the x-axis. This is ensured by the condition $\eta < \sqrt{\frac{a^2}{4} + \left(\frac{\lambda}{2\pi}\right)^2} - \frac{a}{2}$.

The theoretical $e_2(d)_{,d}$ function from Equation 2.14 is plotted in Figure 2.5. For scales smaller than the reach of the system ($d < d_R$), $e_2(d)_{,d}$ is equal to zero. This is the case because at these scales the parallel systems are homeomorphic to a cylinder. Therefore, as mentioned previously, their Euler characteristic $\chi(d)$, and consequently also their length-integrated curvature $H(d)$, are equal to zero. Thus, according to Equation 2.6, $e_2(d)_{,d} = 0$.

Next, the theoretical distribution shows two discontinuities at the characteristic scales d_R and d_{max}. Indeed, according to Equation 2.14, at scales d_R (located at $x = \lambda/2$) and d_{max} (located at $x = \lambda$), the sine functions in the denominators of $e_2(d)_{,d}$ are zero, which leads to the observed discontinuities. These discontinuities indicate an abrupt variation with d of the interface length of the parallel system. In this particular case, d_R is located at the pinch-off section of the cylinder. The abrupt variation of interface length as the erosion scale d reaches d_R is therefore associated with the sudden appearance of cusps in the eroded system, caused by a topological rupture (i.e. the eroded system is no longer simply connected).

For intermediate scales $d_R < d < d_{max}$, the theoretical $e_2(d)_{,d}$ shows an "U" shape. Finally, at d_{max}, the system is completely eroded and $e_2(d)_{,d} = 0$ for $d \geq d_{max}$.

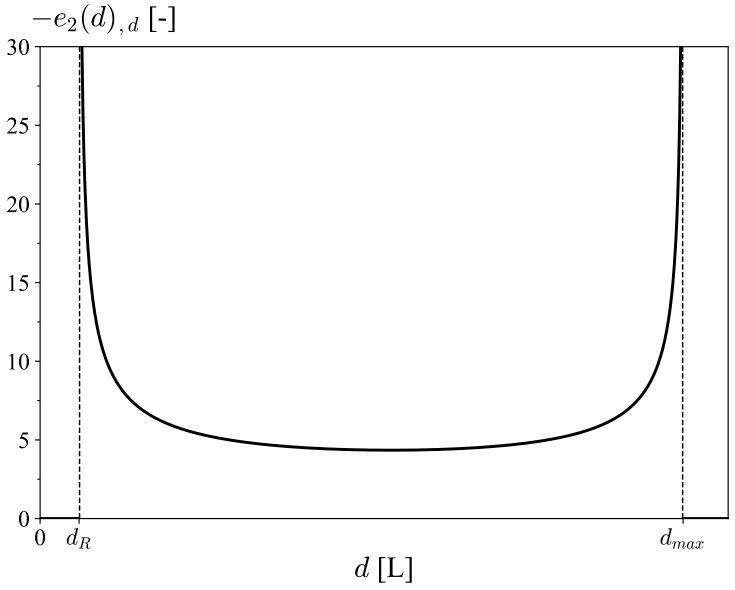

FIGURE 2.5: Theoretical $e_2(d)_{,d}$ distribution of the perturbed cylinder.

2.1.2.3 Distributions of objects

We now consider an ensemble of N objects, each characterized by a diameter D. The ensemble of objects can be represented by a cumulative diameter distribution $F_0(D)$. This distribution corresponds to the number fraction of the objects whose diameter is smaller than or equal to D:

$$F_0(D) = \frac{N(D)}{N} \tag{2.15}$$

where $N(D)$ is the number of objects of diameter smaller than or equal to D. Therefore $F_0(D)$ increases monotonally from 0 to 1. The number-based diameter distribution of the ensemble is called $f_0(D)$. The distributions $f_0(D)$ and $F_0(D)$ are related by:

$$f_0(D) = F_0(D)_{,D} \iff F_0(D) = \int_0^D f_0(D)dD \tag{2.16}$$

The $f_0(D)$ distribution is a normalized function ($\int_0^\infty f_0(D)dD = 1$) and has for dimension the inverse of a length. A diameter distribution such as $f_0(D)$ is associated with a family of mean diameters D_{ab}, as introduced by Mugele and Evans [1951], which characterizes the ensemble:

$$(D_{ab})^{a-b} = \frac{\int_0^{+\infty} f_0(D)D^a\, dD}{\int_0^{+\infty} f_0(D)D^b\, dD} \tag{2.17}$$

where indexes a and b can take any real number provided that $a \neq b$.

The $E_2(d)$, $e_2(d)$ and $e_2(d), d$ distributions are additive (Dumouchel et al. [2022]), i.e. the distribution of a system composed of an ensemble of objects is equal to the sum of the distributions of each individual object in the ensemble. In the next sections, this property is used to determine the scale distributions of an ensemble of cylinders and of spheres, respectively.

Scale distribution of an ensemble of cylinders

Let us consider a 2D ensemble of N_c cylinders, of fixed length L_c, and whose diameters D follow a number-based diameter distribution $f_{0c}(D)$, as well as surface- and number-based cumulative diameter distributions $F_{2c}(D)$ and $F_{0c}(D)$, respectively. The cumulative scale distribution $E_2^c(d)$ of such an ensemble was obtained by Dumouchel et al. [2008] and writes:

$$E_2^c(d) = N_c L_c D_{10} \left[F_{2c}(D) + \frac{D}{D_{10}}(1 - F_{0c}(D)) \right]_{|D=d} \tag{2.18}$$

The scale distribution $e_2^c(d)$ is obtained by derivation of $E_2^c(d)$ with respect to the scale d and writes:

$$e_2^c(d) = N_c L_c \left(1 - F_{0c}(D)\right)_{|D=d} \tag{2.19}$$

and the derivative of the scale distribution $e_2^c(d)_{,d}$ writes:

$$e_2^c(d)_{,d} = -N_c L_c f_{0c}(D)_{|D=d} \tag{2.20}$$

The distribution $e_2^c(d)_{,d}$ is therefore proportional to the diameter distribution $f_{0c}(D)$. Lastly, the second derivative of the scale distribution, $e_2^c(d)_{,d,d}$, writes:

$$e_2^c(d)_{,d,d} = -N_c L_c \left(f_{0c}(D)_{,D}\right)_{|D=d} \tag{2.21}$$

Scale distribution of an ensemble of spheres

We now consider an ensemble of N_s spheres whose diameters D are distributed following $F_{0s}(D)$, $F_{1s}(D)$ and $F_{2s}(D)$, its number-, length-, and surface-based cumulative distributions. The number-based diameter distribution is named $f_{0s}(D)$. For such an ensemble, the cumulative scale distribution, the scale distribution and its first and second derivatives write, respectively:

$$E_2^s(d) = N_s \frac{\pi}{4} D_{20}^2 \left[F_{2s}(D) + \frac{2DD_{10}}{D_{20}^2}(1 - F_{1s}(D)) - \frac{D^2}{D_{20}^2}(1 - F_{0s}(D)) \right]_{|D=d} \tag{2.22}$$

$$e_2^s(d) = N_s \frac{\pi}{2} (D_{10}(1 - F_{1s}(D)) - d(1 - F_{0s}(D)))_{|D=d} \tag{2.23}$$

$$e_2^s(d)_{,d} = -N_s \frac{\pi}{2} (1 - F_{0s}(D))_{|D=d} \tag{2.24}$$

$$e_2^s(d)_{,d,d} = N_s \frac{\pi}{2} f_{0s}(D)_{|D=d} \tag{2.25}$$

Equation 2.25 established that, in the case of an ensemble of spheres, it is the $e_2^s(d)_{,d,d}$ distribution that is proportional to the diameter distribution $f_{0s}(D)$.

2.1.2.4 Notion of equivalent systems

Dumouchel et al. [2008] have intoduced the notion of equivalent systems to designate systems that, althought being different in shape, report identical scale distributions. Dumouchel et al. [2019] have shown that, in 2D, any system can be associated with an equivalent system of cylinders. This notion was then used to describe a cavitation-based atomization process by associating the measured scale distribution to that of an equivalent system of cylinders whose diameter distribution was determined using Equation 2.20.

We now consider a system of cylinders of diameter distribution $f_{0c}(D)$ and a system of spheres of diameter distribution $f_{0s}(D)$. As mentioned previously, if the systems are equivalent, they share the same scale distribution. Therefore, using Equations 2.20 and 2.24, we have:

$$N_c L_c f_{0c}(D) = N_s \frac{\pi}{2}(1 - F_{0s}(D)) \tag{2.26}$$

which means that $f_{0c}(D)$ is proportional to $(1 - F_{0s}(D))$. By definition, $F_{0s}(D)$ starts from zero and grows monotonally towards 1. Therefore $(1 - F_{0s}(D))$ starts from 1 and decreases monotonally towards zero. Figure 2.6 shows schematically the qualitative shapes of a cumulative diameter distribution $F_{0s}(D)$ and its complement $(1 - F_{0s}(D))$ of a monomodal diameter distribution.

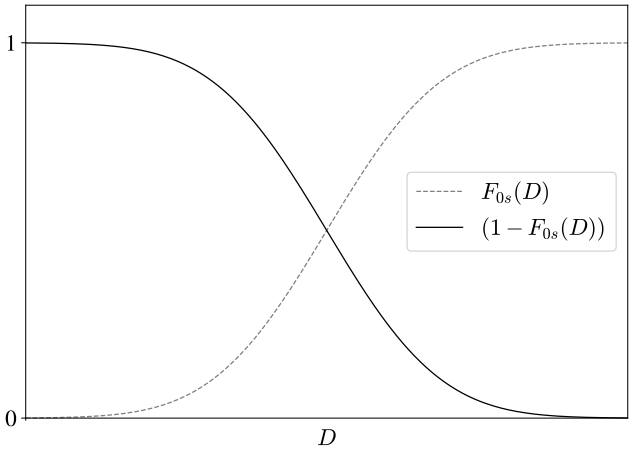

FIGURE 2.6: Schematic example of $F_{0s}(D)$ and $(1 - F_{0s}(D))$

In this case, the $(1 - F_{0s}(D))$ distribution reports a maximum at $D = 0$. The diameter distribution $f_{0c}(D)$ of the equivalent system of cylinders reports therefore the same qualitative shape, with a peak at $D = 0$.

2.1.3 Mathematical representation of scale distributions of ensembles of objects

2.1.3.1 Diameter distributions

Liquid sprays issuing from atomization processes are commonly described by their droplet diameter distribution, which considers that droplets are spherical objects. According to Lefebvre [1989], the choice of a mathematical distribution to represent a given drop diameter distribution strongly depends on the application and on the operating conditions considered. There is therefore no single mathematical expression that can adequatly represent all spray applications. Lefebvre [1989] concludes that the best reasons for selecting a given mathematical diameter distribution are: its mathematical simplicity, the ease of manipulation in computations, and the consistency with the physical phenomena involved.

Most diameter distributions found in the atomization-related literature are empirical distributions, which are obtained by determining a mathematical form that fits a given experimental data set. The most commonly used empirical diameter distributions include the Nukiyama-Tanasawa distribution, the Rosin-Rammler distribution and its modified version, the log-normal distribution, etc. [Babinsky and Sojka, 2002]. These distributions, however, are obtained for a specific domain of validity and should not be used outside of it, since they might lead to unrealistic results.

Another type of diameter distribution found in the literature are those determined by making use of the Maximum Entropy Formalism. This method states that the most likely diameter distribution is the one that maximizes the entropy of the system, under certain constraints [Dumouchel, 2006]. The constraints are related to properties or available information on the desired distribution. Different approaches are found in the literature. Li et al. [1988, 1990], Sellens and Brzustowski [1985], Sellens [1989] proposed a formulation using a normalization constraint and a set of constraints representing the conservation of mass, momentum, kinetic energy and surface energy. Sirignano and Mehring [2000] questioned this approach by demonstrating that thermal processes must be taken into account in order to relate the spray's surface and kinetic energy to the initial energy values. Cousin and Dumouchel [1996] and Dumouchel and Boyaval [1999] on the other hand, proposed a formulation using a single constraint equivalent to the definition of a mean diameter D_{q0}, which introduced two parameters: the mean diameter D_{q0} and its order q. Lastly, Dumouchel [2006] proposed a new formulation using three constraints based on physically relevant information commom to any atomization process. Two constraints relate to the fact that experimental drop diameter distributions report bell shapes, meaning that the production of large and small drop populations is limited. This limitation is due to aerodynamic effects that lead to the desintegration of large drops and to the surface tension effects that limit the size of small droplets. The final constraint considers that the spray is composed of a fixed number of drops. The solution of the problem under these three constraints leads to a three-parameter Generalized Gamma distribution (3pGG).

The 3pGG distribution obtained by Dumouchel [2006] covers many empirical distributions from the literature, such as the Weibull, the Rosin-Rammler or the Nukiyama-Tanasawa distributions [Dumouchel, 2006]. Lecompte and Dumouchel [2008] have successfully used it to represent drop-size distributions from ultrasonic sprays, low-pressure gasoline sprays, and twin-fluid atomizer sprays. In the latter case, results have suggested that the 3pGG distribution has potential to extrapolate results to diameters beyond the measured range. It has also been used by Dumouchel et al. [2019] to describe ligaments from the textural atomization process of a cavitating flow, and to represent the resulting drop-size distribution. This allowed to establish a correlation between the size distribution of the textural liquid ligaments and that of the resulting spray drop population.

In their work about the deformation and breakup of liquid ligaments into droplets, Villermaux et al. [2004] proposed an aggregation model where ligaments are represented by an ensemble of constitutive spherical liquid volumes (called *blobs*) which coalesce as the ligament is about to break up, forming bigger blobs along the ligament. A schematic representation of such constitutive blobs is provided and shown in Figure 2.7. This blob coalescence process results in final mean drop (blob) sizes larger than the average thickness of the initial ligament. In the proposed model, blobs are arranged in independent adjacent layers which interact randomly as blob structures coalesce. When the breakup process is complete and the ligament has given place to a set of droplets, the resulting blob diameter distribution obtained using this model is a gamma distribution. This gamma distribution, as it can be shown, is a particular case of the 3pGG distribution introduced above.

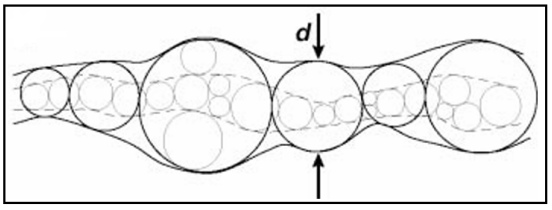

FIGURE 2.7: Schematic representation of a ligament by an ensemble of blobs from Villermaux [2007].

The works cited above demonstrated the capability of the 3pGG distribution to represent both spray drop-size distributions and scale distributions of ligaments responsible for drop production. Moreover, it allows to easily perform mathematical manipulations. These characteristics make the 3pGG distribution a suitable mathematical distribution to represent the diameter and scale distributions considered in this work. Its mathematical expression is detailed in the next section, along with its main characteristics.

2.1.3.2 The 3-parameter Generalized Gamma distribution

The 3pGG number-based diameter distribution takes the following form:

$$f_0(D) = \frac{q}{\Gamma\left(\frac{\alpha}{q}\right)} \left(\frac{\alpha}{q}\right)^{\alpha/q} \frac{D^{\alpha-1}}{D_{q0}^{\alpha}} \exp\left(-\frac{\alpha}{q}\left(\frac{D}{D_{q0}}\right)^{q}\right) \tag{2.27}$$

where $\Gamma(\cdot)$ is the Gamma function. As indicated by its name, the 3pGG distribution introduces three parameters: one positional parameter (D_{q0}) that controls the position of the distribution in the diameter space and two shape parameters (α and q). Parameters α and q must be of the same sign, but may be taken positive or negative [Dumouchel, 2006]. Only positive parameter values are considered here ($\alpha > 0$ and $q > 0$).

Figure 2.8 plots a family of 3pGG distributions with constant $q = 3$ and $D_{q0} = 150$ µm, and varying α. The changes of α impact mostly the shape of the curve in the small-diameter region. As reported by Dumouchel [2006] and Lecompte and Dumouchel [2008], the distribution shows unrealistic behaviors for values of $\alpha < 1$. Moreover, the maximum of the distribution is located at $D = 0$ when $\alpha = 1$ and at diameters near D_{q0} when $\alpha > 1$.

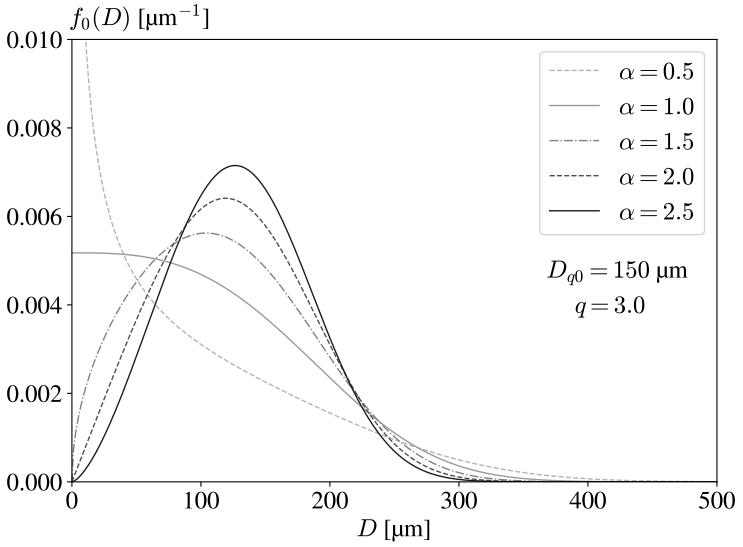

FIGURE 2.8: Influence of α on $f_0(D)$.

Similarly, Figure 2.9 plots a family of 3pGG distributions with constant $\alpha = 3$ and $D_{q0} = 150$ µm, and varying q. In this case, it is the shape of the large-diameter region that is most affected by the variation of q.

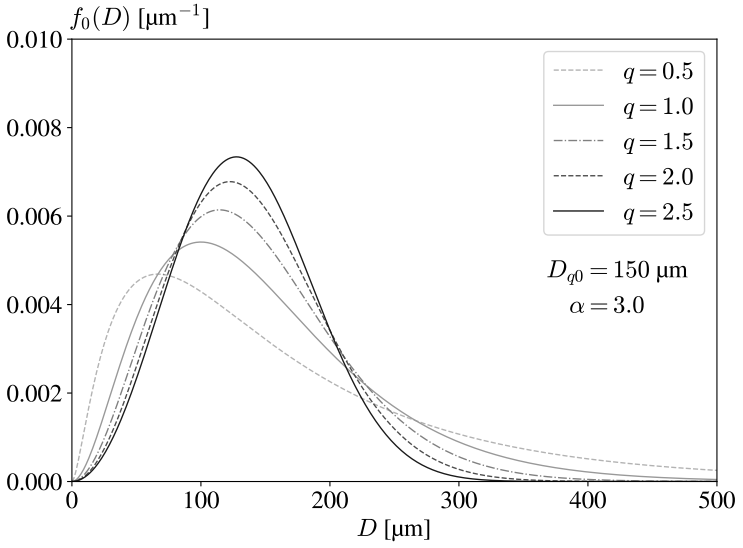

FIGURE 2.9: Influence of q on $f_0(D)$.

2.1.3.3 Scale distributions based on the 3pGG function

3pGG scale distributions of ensemble of cylinders

Equation 2.20 reports that, for an ensemble of cylinders, $e_2^c(d)_{,d}$ is proportional to the diameter distribution $f_{0c}(D)$. If we choose to represent $f_{0c}(D)$ by the 3pGG distribution from Equation 2.27, we get:

$$e_2^c(d)_{,d} = -N_c L_c \frac{q}{\Gamma\left(\frac{\alpha}{q}\right)} \left(\frac{\alpha}{q}\right)^{\alpha/q} \frac{d^{\alpha-1}}{D_c^{\alpha}} \exp\left(-\frac{\alpha}{q}\left(\frac{d}{D_c}\right)^q\right) \tag{2.28}$$

where D_c is the mean diameter D_{q0} of $f_{0c}(D)$.

The $e_2^c(d)_{,d}$ distribution has a peak positioned at scale d_p given by:

$$d_p = \left(\frac{\alpha - 1}{\alpha}\right)^{1/q} D_c \tag{2.29}$$

Figure 2.10 plots a series of $e_2^c(d)_{,d}$ distributions of ensembles of cylinders, each with a different 3pGG diameter distribution, with varying values of α and constant q and D_c. In these examples, we take $N_c L_c = 1$ µm.

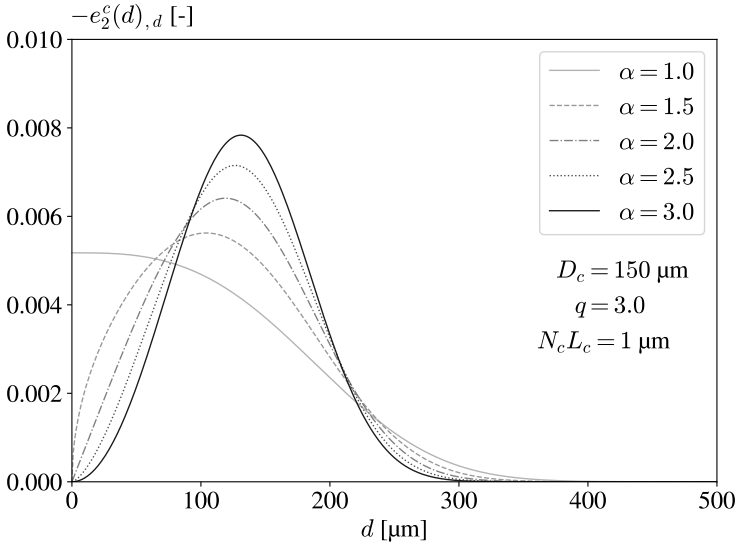

FIGURE 2.10: $e_2^c(d)_{,d}$ of ensembles of cylinders whose diameter distribution $f_{0c}(D)$ are represented by a family of 3pGG distributions with variating α, $q = 3.0$ and $D_c = 150$ µm.

3pGG scale distributions of ensemble of spheres

Equation 2.24 on the other hand reports that, in the case of an ensemble of spheres distributed according to a diameter distribution $f_{0s}(D)$, $e_2^s(d)_{,d}$ is proportional to $(1 -$

$F_{0s}(D)$), where $F_{0s}(D)$ is the cumulative diameter distribution obtained upon integration of $f_{0s}(D)$ according to Equation 2.16. If we again choose to represent $f_{0s}(D)$ by the distribution from Equation 2.27 as an example, we get:

$$e_2^s(d)_{,d} = -N_s \frac{\pi}{2} \left(1 - \frac{\Gamma\left(\frac{\alpha}{q}, \frac{\alpha}{q}\left(\frac{d}{D_s}\right)^q\right)}{\Gamma\left(\frac{\alpha}{q}\right)} \right) \tag{2.30}$$

where D_s is the mean diameter D_{q0} of $f_{0s}(D)$ and $\Gamma(\cdot,\cdot)$ is the incomplete Gamma function.

Figure 2.11 plots a series of $e_2^s(d)_{,d}$ distributions of ensembles of spheres, each with a different 3pGG diameter distribution, with varying values of α and constant q and D_s, and with $N_s \frac{\pi}{2} = 1$. The figure shows that the $e_2^s(d)_{,d}$ distributions have a peak located at $d = 0$ for all of the considered diameter distributions.

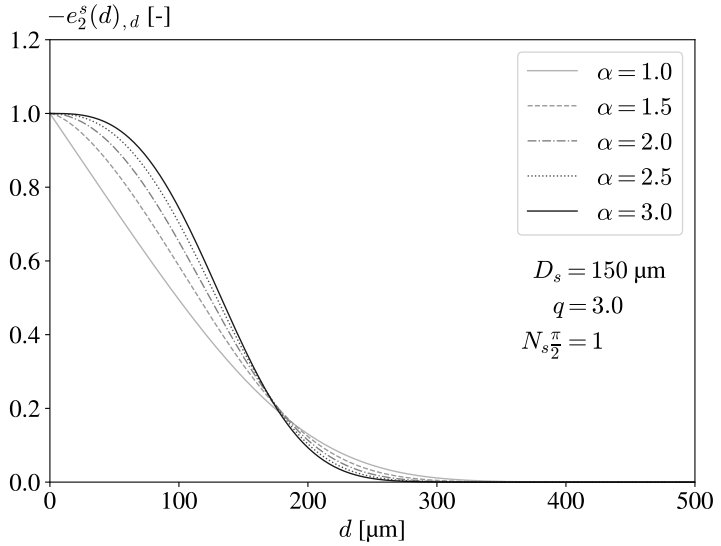

FIGURE 2.11: $e_2^s(d)_{,d}$ of ensembles of spheres whose diameter distribution $f_{0s}(D)$ are represented by a family of 3pGG distributions with variating α, $q = 3.0$ and $D_c = 150$ µm.

3pGG scale distributions of equivalent systems

As introduced previously, for a system of cylinders to be equivalent to a system of spheres, their scale distributions must be equal, and this can only happen if $f_{0c}(D)$ has a peak at $D = 0$. The same observation is true for $e_2^c(d)_{,d}$. Figure 2.10 indicates that, for a system of cylinders whose $f_{0c}(D)$ is represented by a 3pGG distribution, this can only happen when $\alpha = 1$. Indeed, from Equation 2.29, for the peak scale d_p to be equal to zero, the parameter α must be equal to one.

An ensemble of spheres can therefore be equivalent to an ensemble of cylinders if the latter is represented by a 3pGG distribution with $\alpha = 1$. Next, the diameter distribution

of the corresponding ensemble of spheres can be determined. First, setting $\alpha = 1$, $e_2^c(d)_{,d}$ becomes:

$$e_2^c(d)_{,d} = -N_c L_c \frac{q}{\Gamma\left(\frac{1}{q}\right)} \left(\frac{1}{q}\right)^{1/q} \frac{1}{D_c} \exp\left(-\frac{1}{q}\left(\frac{d}{D_c}\right)^q\right) \tag{2.31}$$

Then, since $e_2^c(d)_{,d} = e_2^s(d)_{,d}$, and using Equations 2.31 and Equation 2.24, we have:

$$N_c L_c \frac{q}{\Gamma\left(\frac{1}{q}\right)} \left(\frac{1}{q}\right)^{1/q} \frac{1}{D_c} \exp\left(-\frac{1}{q}\left(\frac{d}{D_c}\right)^q\right) = N_s \frac{\pi}{2}(1 - F_{0s}(D))_{|D=d} \tag{2.32}$$

which relates the cumulative diameter distribution of the searched ensemble of spheres to the parameters of the 3pGG distribution representing the equivalent system of cylinders.

Evaluating the equation above at $d = 0$, the number of spheres in the ensemble can be written as a function of the parameters of the equivalent system of cylinders as:

$$N_s = \frac{2N_c L_c}{\pi} \frac{q}{\Gamma\left(\frac{1}{q}\right)} \left(\frac{1}{q}\right)^{1/q} \frac{1}{D_c} \tag{2.33}$$

Substituting Equation 2.33 in Equation 2.32, we get:

$$(1 - F_{0s}(D))_{|D=d} = \exp\left(-\frac{1}{q}\left(\frac{d}{D_c}\right)^q\right) \tag{2.34}$$

whose derivative with respect to d yields the following expression for the diameter distribution $f_{0s}(D)$:

$$f_{0s}(D)) = \frac{D^{q-1}}{D_c^q} \exp\left(-\frac{1}{q}\left(\frac{D}{D_c}\right)^q\right) \tag{2.35}$$

The mean diameter family D_{m0} of the $f_{0s}(D)$ distribution can be obtained using the definition of mean diameters given in Equation 2.17. Setting $a = m$ and $b = 0$, we get:

$$D_{m0} = q^{1/q} \left[\Gamma\left(\frac{m}{q} + 1\right)\right]^{1/m} D_c \tag{2.36}$$

We recall here that D_s is the mean diameter D_{q0} of $f_{0s}(D)$. Thus, setting $m = q$ in the expression above leads to the following expression for D_s:

$$D_s = q^{1/q} D_c \tag{2.37}$$

Finally, $f_{0s}(D)$ can be rewritten in terms of its parameters q and D_s. Using Equation 2.37 to replace D_c in Equation 2.35, we obtain:

$$f_{0s}(D) = \frac{qD^{q-1}}{D_s^q} \exp\left(-\left(\frac{D}{D_s}\right)^q\right) \tag{2.38}$$

Equation 2.38 reports the diameter distribution $f_{0s}(D)$ of the ensemble of spheres equivalent to the ensemble of cylinders distributed following a 3pGG distribution with $\alpha = 1$. It is found that $f_{0s}(D)$ is coincidentally also a 3pGG distribution, but with $\alpha = q$.

2.2 Multi-scale measurements using image analysis

The description of liquid structures using the multi-scale approach described in Section 3.1 relies on measurements of the surface area $S(d)$ of the parallel systems. In the current work, these measurements are made on binary bitmap images where the liquid system is shown in black against a white background. This section is dedicated to detailing the steps leading from the bitmap image of a given system to the corresponding scale functions $E_2(d)$, $e_2(d)$, and $e_2(d)_{,d}$ as defined in Equations 2.3, 2.4, and 2.6.

2.2.1 Surface area measurements

As defined previously, the multi-scale description requires the knowledge of the surface area $S(d)$ of each parallel system at scale d. When considering systems represented as bitmap images, the surface area $S(d)$ of each parallel system is measured by applying an Euclidean Distance Map (EDM) operation on the original system. For each black pixel in the object, this operation determines the shortest distance between said pixel and the system's interface. A gray level equal to this distance is then attributed to each black pixel (see Figure 2.12 for an example). The surface area $S(d)$ corresponds to the number of pixels whose gray level is equal to or larger than $d/2$. The initial scale value is $d = 0$ and the scale increment step is $\Delta d = 2$ pixels, since d represents the diameter of the erosion disk. The surface areas $S(d)$ are therefore alway equal to integer numbers. The $S(d)$ function allows to determine the cumulative scale distribution $E_2(d)$ and its successive derivatives with respect to d, $e_2(d)$ and $e_2(d)_{,d}$, as introduced in Section 3.1. The numerical derivations are performed using a central difference scheme. Each derivation step is preceded by a smoothing of the function by a moving average over five consecutive points. The EDM algorithm applied is the FIJI Distance Map function which yields a 32-bit grayscale EDM-transformed image.

To assess this measurement method, we consider an application using the cylinder disturbed by a sinusoidal perturbation from Figure 2.4. A synthetic binary image of the

cylinder is produced with an unperturbed diameter of 70 pixels, and with a sinusoidal perturbation of 800 pixels in wavelength and 31 pixels in amplitude. The length of the image is equal to one perturbation wavelength. The corresponding EDM-transformed image is shown in Figure 2.12.

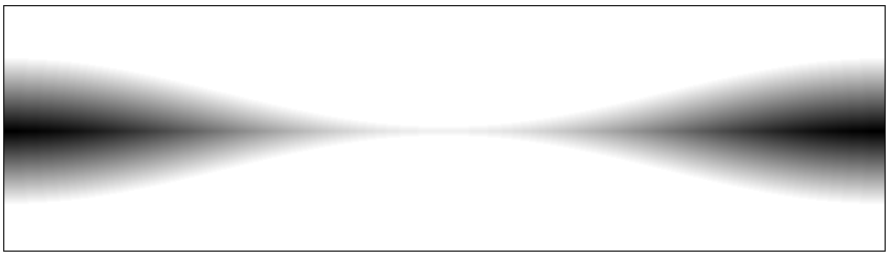

FIGURE 2.12: Euclidean Distance Map of the perturbed cylinder.

The $e_2(d)_{,d}$ distribution is then measured and compared to the theoretical distribution from Equation 2.14 in Figure 2.13. As seen in 2.1.2.2, the theoretical distribution shows two discontinuities at scales d_R and d_{max}. In this case, we have $d_R = 8$ pixels (corresponding to the diameter of the cylinder contraction section) and $d_{max} = 132$ pixels (corresponding to the diameter of the cylinder swelling section) (see Dumouchel et al. [2023]). The measured distribution shows only average agreement with the theorical solution. The scales of the discontinuities are poorly reproduced, especially the small-scale one, and the measurement shows oscillations between these two scales. Finally, we note that the measurement does not tend towards zero when d decreases towards zero, as is predicted by the theory. Indeed, as explained in Section 2.1.2.2, when d is smaller than the reach of the system, the parallel systems are homeomorphic to a cylinder and $e_2(d)_{,d}$ is expected to be equal to zero. These disagreements can be linked to the pixelated nature of the image.

The pixelated nature of the bitmap image leads to surface areas $S(d)$ that are always equal to integer numbers of pixels. This induces a bias in the measurement and leads to the oscillations observed between scales d_R and d_{max}. Added to an insufficient image spatial resolution, this also leads to the imprecise description of the theoretical peaks near the discontinuities. These differences must be addressed to allow the study of the small-scale features of the system. An improvement to the $S(d)$ measurement method can be introduced to a avoid this problem. The proposed method is detailed in the next section.

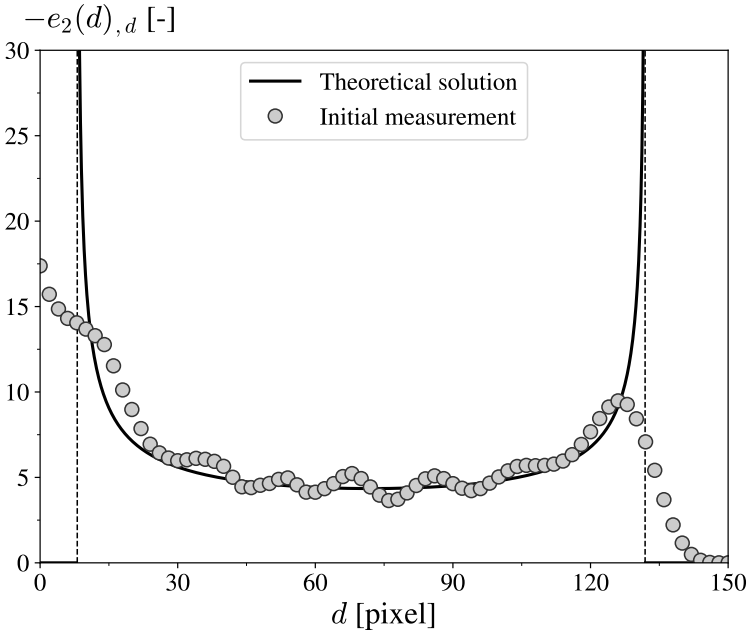

FIGURE 2.13: Application to the perturbed cylinder: comparison between measurement and theoretical $e_2(d)_{,d}$.

2.2.2 Improved method for measuring surface areas

An alternative method for measuring the surface area of the parallel systems relies on applying an EDM tranformation on the binary image and using the resulting exact distances between each object pixel and the interface to measure $S(d)$. The exact shortest distance r between a given pixel and the interface is defined as:

$$r = \sqrt{n_x^2 + n_y^2} \tag{2.39}$$

where n_x and n_y correspond to the number of pixels separating the considered object pixel from the nearest interface pixel in the x- and y-directions respectively, as shown in Figure 2.14.

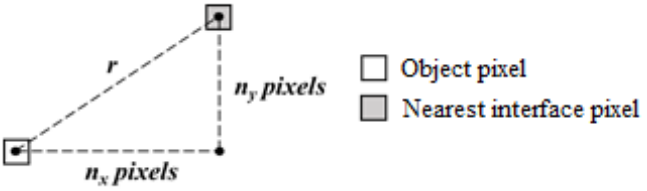

FIGURE 2.14: Definition of n_x and n_y.

The exact distances r constitute a series of discrete values, and can be rewritten as:

$$r = r_i + r_f \tag{2.40}$$

with r_i and r_f the integer and fractional parts of r, respectively.

The exact distance series r is distributed into a series of bins corresponding to the integer distances r_i. Each exact distance r is distributed into bins r_i and $r_i + 1$ according to the following proportion:

$$\begin{cases} (1 - r_f) \text{ into bin } r_i \\ r_f \quad \text{into bin } r_i + 1 \end{cases} \tag{2.41}$$

Therefore, a black pixel whose exact distance r has an integer part r_i feeds both the r_i and the $r_i + 1$ bins, in the proportion established by Equation 2.41. The surface area $S(d)$ of the eroded system at scale d can thus be expressed as:

$$S(d) = S(0) - \sum_{r_i=0}^{d/2} m(r_i) \tag{2.42}$$

where $m(r_i)$ is the total distance count in bin r_i once the contribution of all pixels has been added. The surface areas from Equation 2.42 are no longer necessarily equal to an integer number.

Figure 2.15 plots the new measured $e_2(d)_{,d}$ distribution of the perturbed cylinder, obtained using the new method for measuring $S(d)$, and compares it to the theoretical distribution. The oscillations found in the initial measurement of $e_2(d)_{,d}$ (shown in Figure 2.13) disappear when using the new method. Moreover, the discontinuity at d_R is now identified by a peak in the vicinity of this scale, in the same way as near the discontinuity at scale d_{max}. The new surface area measurement method yields, therefore, an improved $e_2(d)_{,d}$ measurement.

However, a few disagreements with respect to the theory still remain. In particular, the peaks identifying the discontinuities at scales d_R and d_{max} are wide and do not accurately reproduce the shape of the theoretical function in the near vicinity of these scales (disagreements are found in the range d_R (or d_{max}) $\pm$ 16 pixels.

The width of the peaks is largely influenced by the spatial resolution of the initial bitmap image of the object. To evaluate the impact of spatial resolution on the measurement results, and in particular on the width of the peaks, the next section focuses on the measurement of $e_2(d)_{,d}$ of the same synthetic object using images with different spatial resolutions.

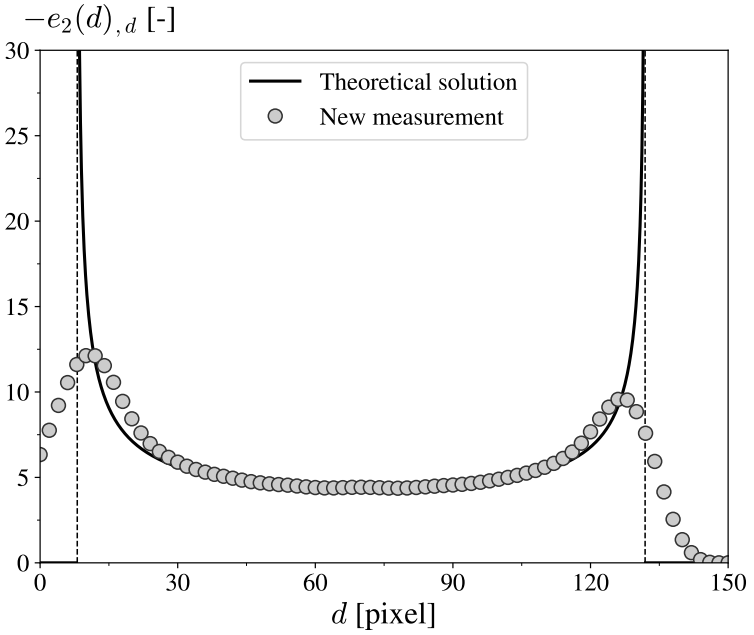

FIGURE 2.15: $e_2(d)_{,d}$ with new method of measuring S(d).

2.2.3 Effect of spatial resolution on the measurement

We define the resolution of the original image (whose measured $e_2(d)_{,d}$ distribution is the one shown in Figure 2.15) as a reference resolution R, with a pixel side size equal to 1. Next, we consider images of resolutions $4R$, $8R$ and $16R$, with pixel side sizes of 1/4, 1/8, and 1/16, respectively. Figures 2.16(a-c) plot the corresponding $e_2(d)_{,d}$ measurements with image resolution 4R, 8R and 16R, respectively, and compare the measurements with the theoretical solution. These results show that, with the increase in spatial resolution, the shape of the peaks found at the discontinuities approach the shape of the theoretical function in this zone.

In addition to the shape of the function near the discontinuities, an important aspect of the theoretical solution is that $e_2(d)_{,d} = 0$ for $d < d_R$. The measured distributions in Figure 2.16 show a surge in the values of $e_2(0)_{,d}$ in the vicinity of $d = 0$. This surge is believed to be caused by remaining pixelization effects, which are strongly reduced by the introduction of the new method for measuring $S(d)$ but persist in the very small-scale range. Figure 2.16 also shows the same measurements in the [0,50] pixels scale range (plots on the right). This allows the observation of the effect of the image resolution on the measured distributions in the very small-scale zone where pixelization effects are still present. The width of the surge near $d = 0$ decreases as the resolution increases. At resolution 4R, the distribution does not reach $e_2(d)_{,d} = 0$ at scales $d < d_R$, and the width of the surge cannot be accurately identified. For resolutions 8R and 16R, the distributions reach $e_2(d)_{,d} = 0$ just before d_R and the width of the surge decreases as the resolution increases. At resolution 8R, the distribution reaches zero at $d = 5.7$ pixels

approximately, while at resolution 16R it reaches zero at $d = 3.5$ pixels approximately. These results show that the increase in image resolution improves the measurements in two main ways: first, the shape of the distribution approches that of the theoretical solution, and second, the range of the pixelization error-zone is reduced, which allows the distribution to reach $e_2(d)_{,d} = 0$ in the very small-scale zone.

These observations are important when considering the measurement of structures of small size such as the textural liquid ligaments studied in this work. In the following subsection, a method used for increasing the spatial resolution of images is presented.

2.2.4 Sub-pixel image interpolation

Experimental images are captured with a given resolution, which is fixed by the optical arangement. If an increase in image resolution is desired, it must be achieved by an image processing method. The chosen method to increase the spatial resolution of the experimental images captured in this work (see experimental backlighting images from Chapter 3) is a bilinear image interpolation [Fadnavis, 2014]. This method is chosen because it allows to reproduce the shape of the visualized liquid structures while remaining computationally cheap when compared to other types of interpolation.

The bilinear interpolation increases the number of pixels in an image by replacing the original pixel-grid with a new grid of smaller pixels. The number and size of the new pixels depends on the desired output resolution. For each pixel in the new grid, new pixel value is calculated by a weighted average of the intensities of the four nearest pixels in the original grid. The weights are equal to the distances between the new pixel and its neighbors in the original grid. The algorithm used to perform the interpolations is the Fiji Bilinear Interpolation based on the method described by Burger and Burge [2022] and summarized below.

We wish to determine the value of a given pixel of the interpolated image positioned at (x, y), $P = I(x, y)$, where I represents the intensity value of the pixel at the given position. To do so, the following steps are used. First, the pixel values of the four nearest neighbors (A, B, C and D) in the original image are identified:

$$\begin{aligned} A &= I(u_x, v_y), \\ B &= I(u_x + 1, v_y), \\ C &= I(u_x, v_y + 1), \\ D &= I(u_x + 1, v_y + 1) \end{aligned} \tag{2.43}$$

where u_x and v_y are the integer parts of x and y, respectively.

Then, the neighbor values A, B, C and D are interpolated, first horizontally and then vertically, to yield the interpolated pixel value P given by:

$$\begin{aligned} P &= I(x,y) \\ &= A + (x-u_x)(B-A) + (y-v_y)\left(C + (x-u_x)(D-C) - A - (x-u_x)(B-A)\right) \end{aligned} \tag{2.44}$$

To obtain the desired interpolated image, this operation is performed for each pixel position (x, y) in the new pixel-grid. The result us a grayscale interpolated image. When the original image shows a binary system (such as the one in Figure 2.4 for example), the grayscale interpolated image can be made binary again by applying a simple median threshold on the pixel values.

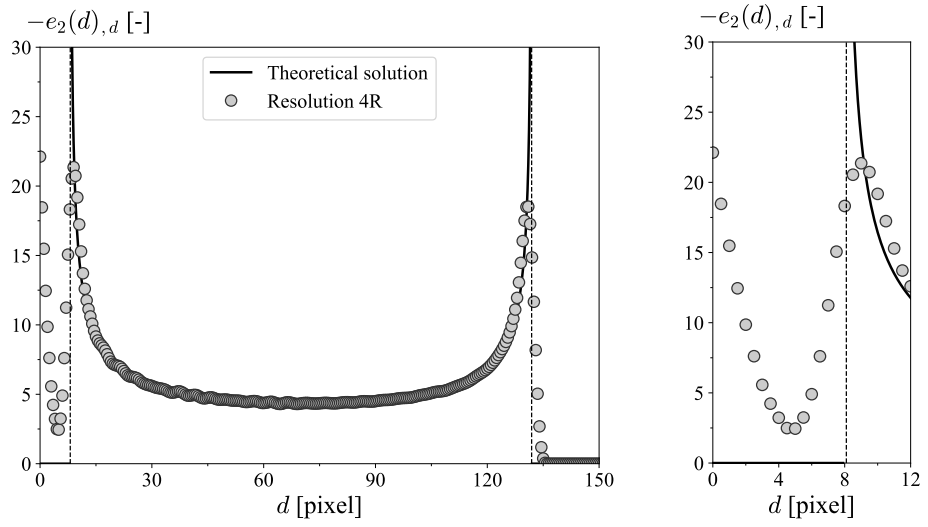

(a)

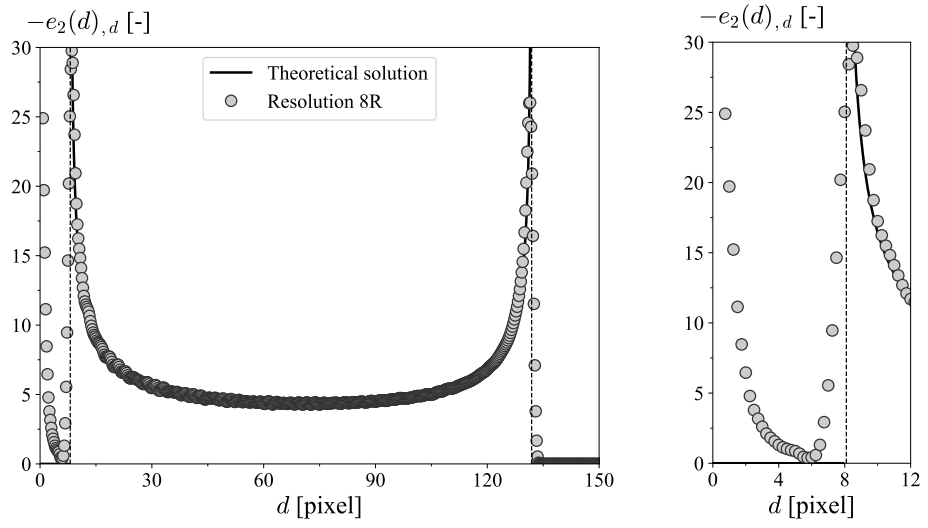

(b)

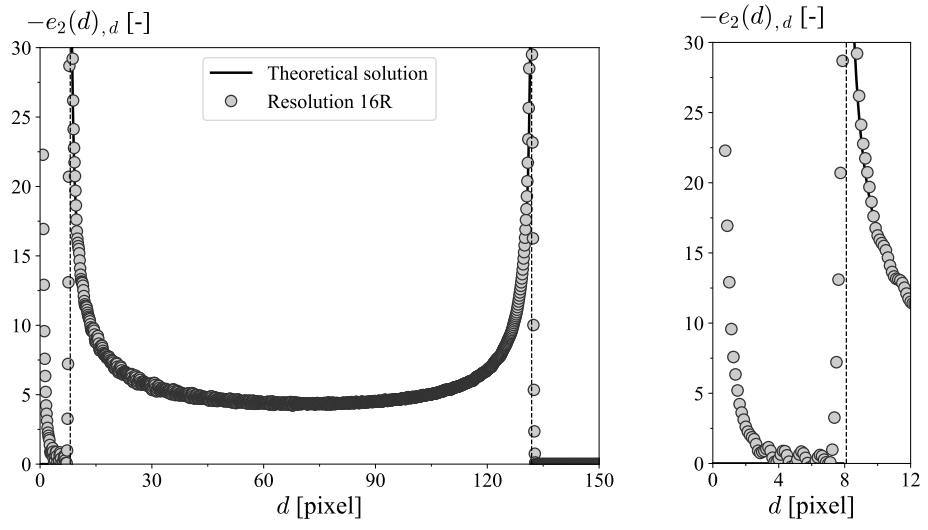

(c)

FIGURE 2.16: Effect of an increase in spatial resolution ((a) 4R, (b) 8R and (c) 16R) on the measured $e_2(d)_{,d}$ of the perturbed cylinder. Entire distributions are shown on the left, and a zoom into the small scale region is shown on the right.

The next section is dedicated to an application of the multi-scale measurement method and the improvements described above to a simulated liquid breakup event.

2.3 Scale distribution of a ligament breakup process

In his PhD thesis, Ngo [2013] measured the scale distribution of individual liquid ligaments issued from a triple-disk-injection atomization process as they undergo breakup. Measurements are made at different non-dimensional times during the breakup process. One such ligament breakup event is shown in Figure 2.17(a) where the contour of the liquid ligament and the droplets it produces is shown at each selected intermediate time. A 3pGG distribution is fitted to the experimental $e_2(d)$ measurement at each time. The associated diameter distributions $f_{0c}(D)$ of the equivalent system of cylinders is determined for each time and shown in Figure 2.17(b). Initially, before the ligament breaks up intro droplets, the associated $f_{0c}(D)$ distributions report shapes similar to those seen in Figure 2.10 for $\alpha \geq 2$. Then, as the ligament begins to break up into droplets, $f_{0c}(D)$ evolves towards the shape associated to $\alpha = 1$ in Figure 2.10, i.e. with a maximum located at $D = 0$ µm. These results from Ngo [2013] show that a liquid ligament and the droplets it produces can be represented by a 3pGG diameter distribution of cylinders whose parameter α tends to 1 as the breakup process evolves. This is in agreement with the conclusions from Section 2.1.3.3 where it was argued that the $e_2^c(d)_{,d}$ distribution of the system of cylinders equivalent to an ensemble of spheres and represented by a 3pGG distribution should have $\alpha = 1$. The reported evolution of the associated $f_{0c}(D)$ during the ligament breakup process may be used to model such atomization processes.

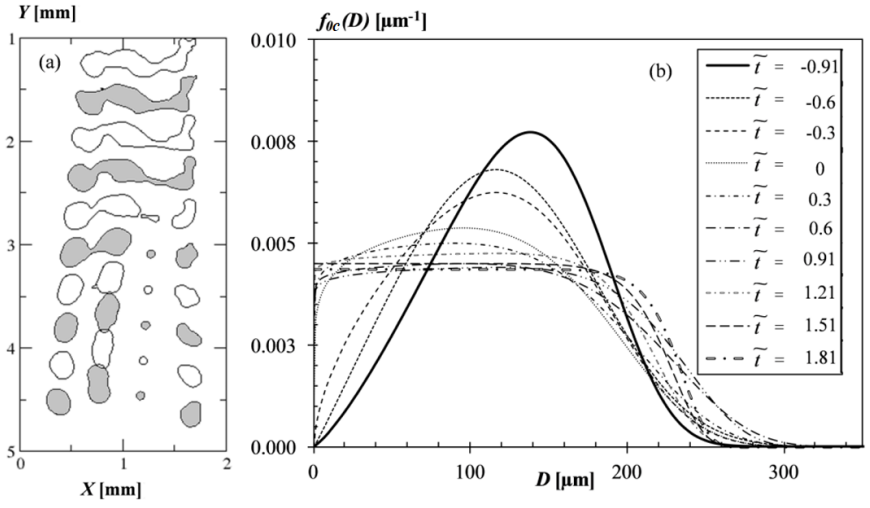

FIGURE 2.17: Ligament breakup process, adapted from Ngo [2013]: (a) contour of the liquid systems; (b) diameter distribution of the equivalent system of cylinders.

Next, we apply the image measurement technique presented earlier in this chapter to images of an individual ligament undergoing breakup, obtained from the DNS simulation

from Hoarau et al. [2024] detailed later in Chapter 3. Figure 2.18 shows the selected liquid system at different intermediate times during its breakup. The liquid system evolves from a single intact ligament at $t = t_0$ to an ensemble of droplets at $t = t_8$. In the last image ($t = t_8$), the smaller droplets are almost spherical, while larger ones are more deformed. The $e_2(d)_{,d}$ distribution is measured at three selected times: the intial time $t = t_0$, an intermediate time $t = t_3$ and the final time $t = t_8$. The characteristic sizes of some parts of the liquid system at these selected times are indicated in Figure 2.19.

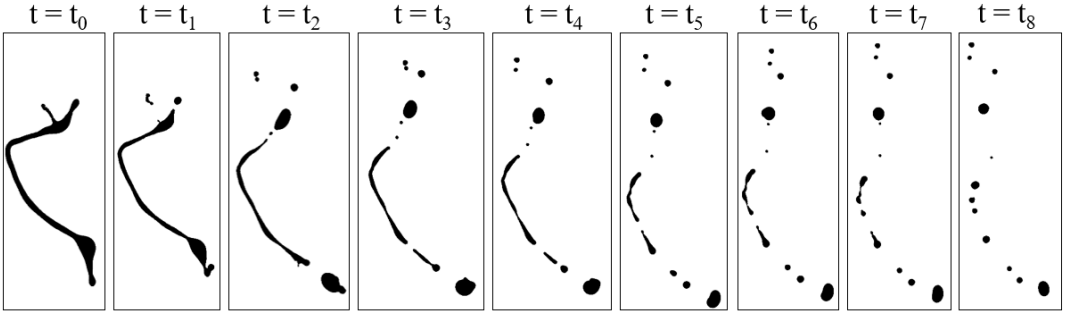

FIGURE 2.18: Ligament breakup process.

The $e_2(d)_{,d}$ distribution of the liquid system is measured at each selected time. The improved measurement method described in the previous section is used. A $4x4$ sub-pixel image interpolation is applied, leading to an increase in image resolution by a factor of 4. The resulting spatial resolution is 0.85 µm/pixel.

The measured $e_2(d)_{,d}$ distributions of the liquid system at selected times $t = t_0$, $t = t_3$ and $t = t_8$ are presented in Figure 2.20 as a semilog plot. Each distribution shows a series of peaks. These peaks are associated with the presence of contracted or swollen sections of the liquid system (as seen in Section 2.1.2.2).

The measurements reported in Figure 2.20 are divided in two regions: Region (1) contains information on the small-scale structures while Region (2) deals with larger-scale structures. Some of the distributions a maximum located at a peak in the small-scale Region (1). This peak is indicative of the presence of a long ligamentous structure, according to Equation 2.20. Figure 2.19 shows that this is indeed the case at $t = t_0$ and $t = t_3$. The distributions also report peaks in the large-scale Region (2). These peaks correspond to the scale distribution of the equivalent ensemble of cylinders representing the large structures in the liquid system. These distributions report either peak shapes with a local maximum, or step-like shapes with no local maximum and a monotonically decreasing behavior. When the distribution shows a local maximum, the represented structure is not spherical. When the distribution does not show a local maximum, then the represented structure is spherical, according to Equation 2.24.

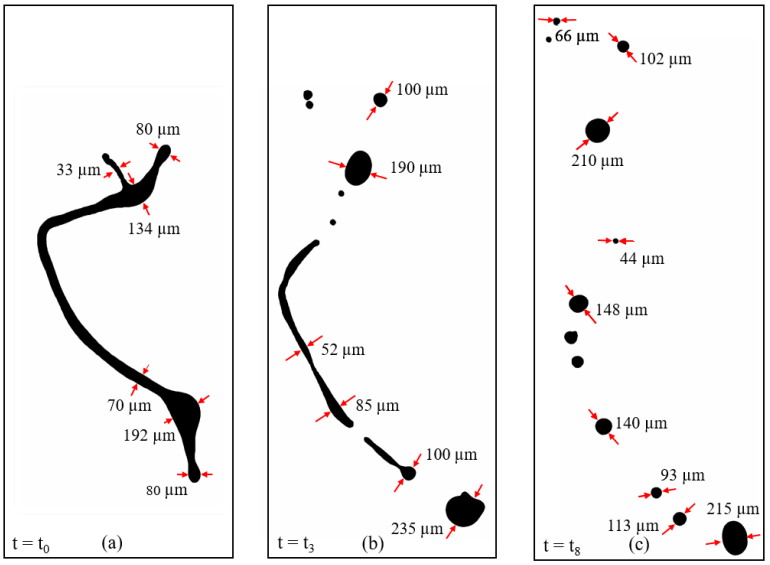

FIGURE 2.19: Size of structures at selected times: (a) $t = t_0$, (b) $t = t_3$ and (c) $t = t_8$.

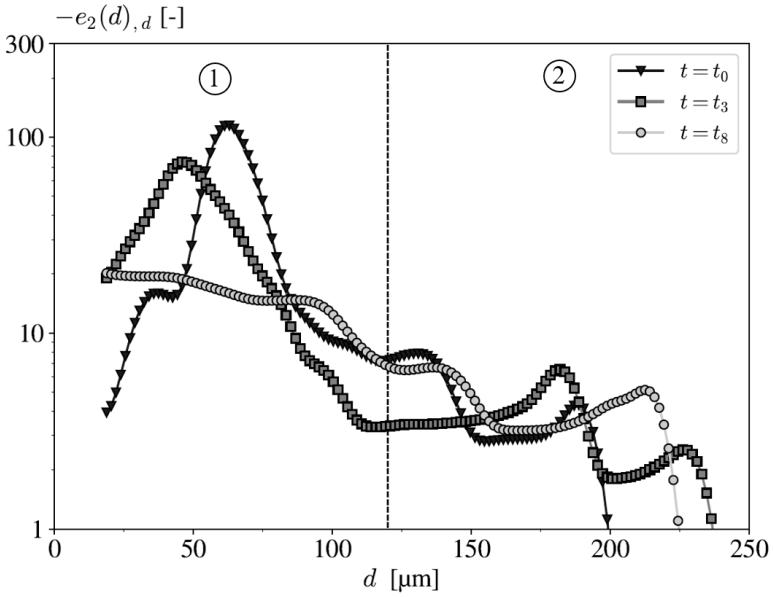

FIGURE 2.20: Semilog plot of the $-e_2(d)_{,d}$ distribution at selected times $t = t_0$, $t = t_3$ and $t = t_8$.

The evolution of $e2(d)_{,d}$ from $t = t_0$ to $t = t_8$ is indicative of the ligament breakup process observed in Figure 2.19. At $t = t_0$, the distribution shows a large small-scale peak in Region (1), which corresponds to the long and thin ligament section in Figure 2.19(a). In Region (2), the distribution reports peaks that represent the non-spherical swollen sections near the ends of the ligament.

At $t = t_3$, the distribution still reports a peak in Region (1), which represents the thin ligament section still observed in Figure 2.19(b). In Region (2), the distribution

still shows peaks, that now represent the large non-spherical droplets that have been produced.

At $t = t_8$, the distribution no longer shows a large peak in Region (1). This means that no ligamentous structure is left. Instead, the distribution is monotonically decreasing, which is indicative of the distribution of spherical structures. In Region (2), the distribution still reports peaks representative of large non-spherical structures. This is indeed the case since, as seen in Figure 2.19(c), the system is composed entirely of small, spherical droplets and of large, non-spherical droplets.

The evolution of the measured $e2(d)_{,d}$ distributions in Figure 2.20 shows that the peaks representing the large droplets are observed from $t = t_0$, when the ligament is still intact. Therefore, the signature of the large droplets appears quite before the breakup event. This signature of the large droplets, identified before the breakup of the ligament, contains information on the dispersion of droplet sizes (since the droplets can be deformed, the sizes identified are not always equal to their equivalent diameter).

2.4 Conclusion

The multi-scale description of liquid systems was presented in this chapter. Theoretical aspects of the method are introduced and used to determine scale distributions of cylinders and spheres. A mathematical representation of the scale distribution of ensembles of cylinders or spheres is also presented. The notion of equivalent systems is introduced. This notion says that systems of different shapes may report identical scale distributions. In particular, in 2D, any system can be represented by an equivalent system of cylinders.

Then, an image analysis technique allowing to measure the scale distribution of objects shown in binary images is also introduced. This image measurement technique is then used to measure the scale distributions of a liquid ligament, issuing from a direct numerical simulation, as it breaks up into droplets. The evolution of the scale distributions during the breakup process allows to draw insights into how the information about the droplets produced can be found in the ligament before the breakup even occurs.

The image measurement technique, the notion of equivalent systems, and the insights about the ligament breakup process are used in Chapter 4 to evaluate the proposed image processing method and in Chapter 5 to analyse the textural atomization process of a reactive LOx/CH_4 assisted jet.

Chapter 3

Fiber-regime coaxial assisted atomization study cases

Research on rocket engine liquid atomization focuses on understanding the associated physical phenomena both in reactive environments, representative of real rocket engine operation, and in less demanding, non-reactive environments. The study of atomization in liquid rocket engines implies reactive conditions that usually include effects from the combustion of the propellants (high temperature field, strong density gradients, etc.), turbulence from the high Reynolds and Weber number of the injected propellants, among others. These harsh conditions bring experimental and numerical difficulties that limit the amount of measurements that can be made. To study specific phenomena independently of the combustion of the propellants, and to avoid the difficulties related to these harsh conditions, many studies found in the literature are made under non-reactive conditions with water-air as replacement for the propellants and at ambient temperatures to avoid evaporation effects. This allows to reproduce the same mechanisms related to the atomization process in liquid rocket engines and can allow to obtain better-quality measurements.

This chapter aims at presenting the two fiber-regime atomization study cases considered in this thesis. A complementary approach is proposed, with representative experiments in reactive (MASCOTTE) and non-reactive (MARACA) conditions. The main study case is the reactive MASCOTTE configuration, where conditions are representative of real rocket engine subcritical operation. This configuration represents the main experimental work developed during the current PhD work. The contributions made to the experimental work on the MASCOTTE configuration includes the definition of reactive operating conditions in collaboration with the test engineer, the setup of optical diagnostics at high spatial resolutions to investigate the small scales of the atomization process, and the recording of images during the testing campaign. This is the work reported in the current chapter. The rest of the work done in this PhD related to the MASCOTTE

configuration is presented later in Chapters 4 and 5, and includes the development of a post-processing methodology to allow the characterization of the textural atomization process using the multi-scale method from Chapter 2 (Chapter 4) and the development of a model to analyze the textural atomization process (Chapter 5).

The second case considered is the non-reactive MARACA configuration, where conditions are less harsh compared to the MASCOTTE configuration, which allows both experimental and numerical investigations. In this case, the experimental images were recorded by the teams at CORIA, while the numerical DNS simulation was performed by the teams at ONERA. The specific contributions done in the current work involve the post-processing of the experimental images from CORIA and the production of images from the already-existing DNS simulation results. These images are presented in this chapter and later used (in Chapter 5) to characterize the observed textural atomization process and assess the capacity of the DNS simulation to reproduce the experiments in terms of the textural atomization. The experimental test-benches, the optical diagnostics and the resulting experimental images of the atomization process of both configurations are presented, as well as the DNS simulation protocol and the resulting visualizations.

Contents

3.1 Reactive flow: the MASCOTTE LOx/CH_4 case

Coaxial assisted atomization processes in reactive, rocket engine-like conditions, have been studied at ONERA Palaiseau Center, in the MASCOTTE test-bench, since the

1990s [Vingert et al., 2016]. Many reference cases have been established to study combustion processes in conditions representative of rocket engine combustion chambers and/or gas-generators using either LOx/H_2 or LOx/CH_4 propellants [Habiballah et al., 2006]. One of such cases is the A-10 reference point. Designed to study the combustion of liquid oxygen and gaseous hydrogen in subcritical conditions, the chamber pressure is defined at $P_c = 10$ bar. The atomization of the liquid oxygen jet is in the fiber regime according to the classification diagram from Lasheras and Hopfinger [2000] (see Figure 3.3). More recently, studies on methane-powered engines have been done considering the combustion of liquid oxygen and gaseous methane in conditions similar to the A-10 point, namely in subcritical conditions and in the fiber atomization regime as in Boulal et al. [2022]. Fdida et al. [2019] compared a LOx-H_2 and a LOx-CH_4 combustion processes in the MASCOTTE test bench. The study reported differences, in the near injector region of the flow, related to the higher density of the methane flow (the density of CH_4 is six times higher than that of H_2). However, further investigations of the subcritical combustion and atomization of the LOx-CH_4 propellant couple are still necessary.

Three operating conditions are therefore defined in the framework of this thesis, in subcritical regimes using the LOx/CH_4 couple as propellants. Experiments were performed in the MASCOTTE test-bench and have allowed to obtain backlighting and OH* chemiluminescence visualizations of the atomization and combustion processes inside the combustion chamber. These backlighting visualizations are used in Chapters 4 and 5 in the study of the textural atomization process. This section is dedicated to presenting the experimental test-bench, the tested operating conditions, the optical diagnostics and the resulting visualizations.

3.1.1 MASCOTTE test-bench

The experimental investigation of the atomization process under reactive flow conditions was performed in the MASCOTTE test-bench. The main characteristics of the test bench are presented in this section, and more information can be found in [Habiballah et al., 2006].

The MASCOTTE subscale rocket combustor is capable of reproducing operating conditions similar to those encountered inside the combustion chambers of cryogenic liquid rocket engines. It is designed to allow the study of fundamental physical processes occurring inside the combustion chamber or the gas generators of such engines. The main physical processes studied include the injection and atomization of the propellants [Fdida et al., 2016], flame strutcture [Candel et al., 2006] and the onset of combustion instabilities [Boulal et al., 2022], as well as heat transfer [Grenard et al., 2019] and soot formation in the case of LOx/CH_4 flames [Lechner, 2024, Vingert et al., 2019].

The fire-tests were conducted using the high-pressure, high-mixture ratio (BHP-HRM) combustor described by Ordonneau et al. [2011]. The combustion chamber, shown in Figure 3.1 in a sectional view, consists of a horizontal tube of 615 mm in length composed of a series of interchangeable circular modules of 56 mm in diameter. The chamber is water-cooled and designed to operate at conditions representative of real rocket engine thrust chambers, i.e. high pressures and high mixture ratios. It can reach chamber pressures of up to 70 bar under stoichiometric conditions [Grenard et al., 2019].

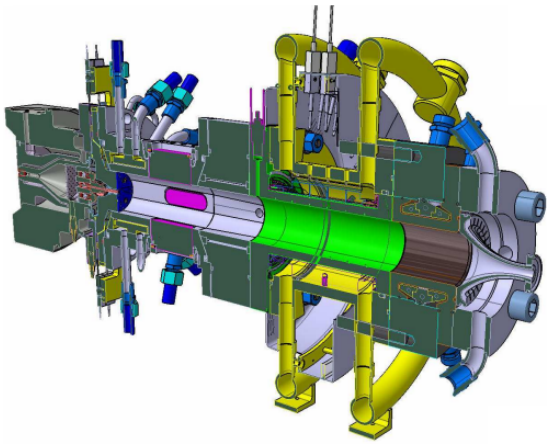

FIGURE 3.1: The BHP-HRM combustor in its visualization version, from [Ordonneau et al., 2011].

The injection system is composed of a single shear-coaxial injector, shown in Figure 3.2. It injects a liquid jet of oxidizer (liquid oxygen) through a central circular tube surrounded by a high-velocity gaseous fuel (methane) flow injected from an annular tube. There is no recess between the liquid and the gas injection-tube exit planes. The diameter at the exit of the LOx injection tube is named D_l. The inner and outer diameters of the annular CH_4 injection tube are $D_n = 1.24D_l$ and $D_g = 1.64D_l$, respectively.

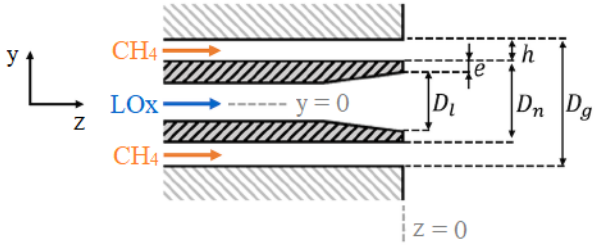

FIGURE 3.2: Coaxial injector.

The version of the BHP-HRM combustion chamber used in the experiments is equipped with two opposite rectangular quartz optical windows of 25 mm x 70 mm. These optical windows allow the visualization of the internal flow and the use of optical diagnostics.

3.1.2 Operating conditions

Experiments in the MASCOTTE test bench are costly and a limited number of testing days were available for the experimental campaign. As a consequence, the number of test runs was also limited, and the tested operating conditions had to be chosen carefully. The operating conditions tested during the experiments were defined, in collaboration with the test engineer, considering the goals of the study as well as constraints imposed by the test bench architecture. The main constraints considered are listed below:

- LOx/CH_4 propellants.
- Thrust chamber-like environment (high mixture ratio, near $M = 3.5$).
- Subcritical conditions (chamber pressure lower than the critical pressure of the propellants).
- Fiber-type atomization regime (liquid Reynolds number of the order of 10^4 or higher; gaseous Weber number of the order of 10^3 or higher).
- Variable chamber pressure and/or momentum-flux ratio.
- Fixed LOx mass-flow rate.
- Fixed injector geometry.
- Available nozzle geometries.

Additionally, the chamber pressures had to be limited to approximately 15 bar so that quality images, where the liquid-gas interface is clearly visible, could be recorded to allow the description of its deformation.

Three reactive operating conditions are chosen (RA, RB, and RC), with varying chamber pressures P_c. Table 3.1 summarizes the main parameters defining the achieved operating points. For all of them, the LOx/CH_4 propellants are injected in a subcritical state, i.e. their pressure and temperature are below their critical point values [Lux and Haidn, 2009]. The mixing ratio M is close to the stoichiometric value ($M_{st} = 4$ for LOx/CH_4 combustion) and is kept nearly constant during the experiments. The liquid Reynolds number Re_l, based on the LOx injector diameter D_l, is kept as close to constant as possible given the experimental constraints. The momentum flux ratio J, commonly used to characterize atomization processes, varies across the different operating points, decreasing as P_c is increased. Finally, as P_c increases, so does the gas density ρ_g.

The tested operating conditions place the atomization process in the fiber-type breakup regime, according to the assisted atomization regime classification from Lasheras and

TABLE 3.1: Tested operating conditions

OC	p_c (bar)	J	M	Re_l	We_R	ρ_l/ρ_g
RA	7	15	3.5	7.7x10^4	4.6x10^4	224
RB	10	10	3.5	9.1x10^4	4.4x10^4	150
RC	15	8	3.2	1.2x10^5	5.9x10^4	97

Hopfinger [2000], shown in Figure 3.3. This atomization regime is typical of liquid rocket engines. From the figure, it can be seen that the atomization regime of the tested operating conditions are very close to the one from the A-10 reference point.

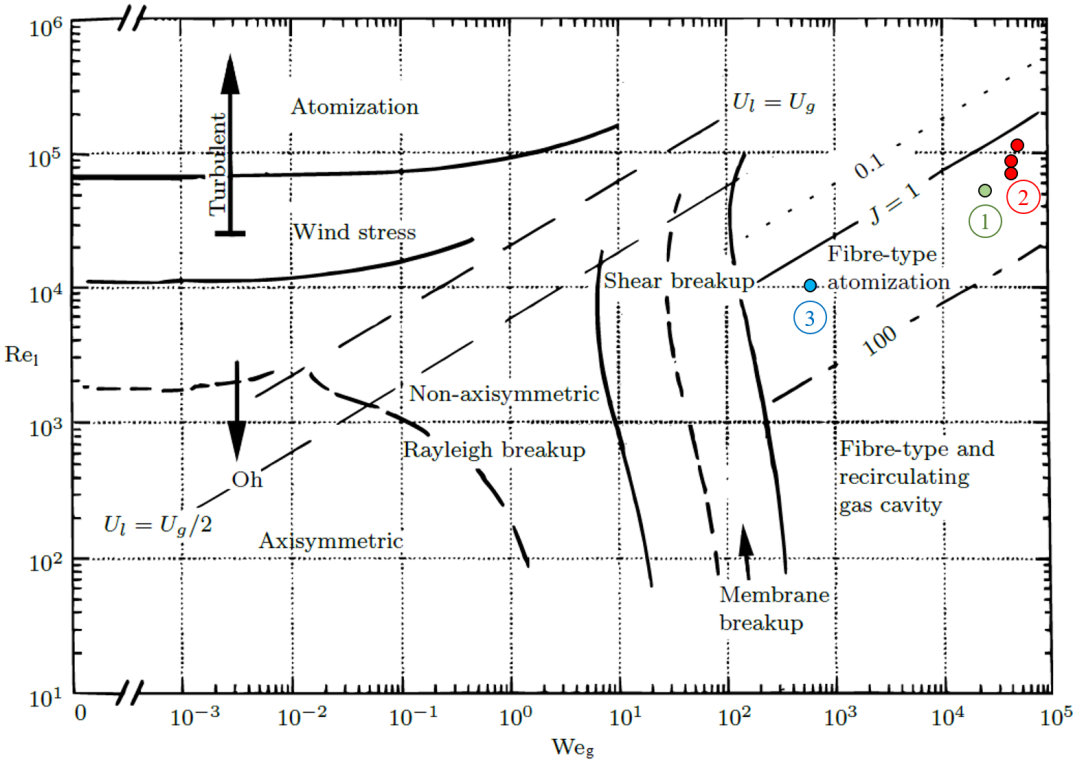

FIGURE 3.3: Atomization regime diagram from Lasheras and Hopfinger [2000]. Identification of the operating conditions considered in this thesis: (1) MASCOTTE A-10 reference point; (2) MASCOTTE *RA*, *RB* and *RC* operating conditions; (3) PF-ONERA reference point.

3.1.3 Optical diagnostics

The visualization of the reactive flow during the combustion process is performed using optical diagnostics. The chemiluminescence of the OH* radical is classically used to visualize the flame front, while a backlighting technique is usually used to visualize the liquid flow. The OH* chemiluminescence imaging setup and the backlighting setup used to record the interface topology are described in the following.

3.1.3.1 OH* chemiluminescence

Combustion processes in general involve a series of elementary chemical reactions that produce intermediate chemical species. Some of the elementary reactions occurring during the combustion process produce radicals on excited energy levels. These excited radicals then spontaneously and rapidly emit a photon and transit to a lower energy level. The light emission resulting from the energy transition is called chemiluminescence and it can be detected using dedicated optical diagnostics techniques.

The presence of some particular excited species and their chemiluminescence can therefore be used as a marker to detect the reaction zone. In the case of LOx/CH_4 combustion, the chemiluminescence of the OH* or CH* radicals is commonly used to detect the reaction zone. The spontaneous emission of the OH* radical occurs at a relatively narrow wavelength band around 320 nm, while the CH* radical emits in a band around 436 nm [Fdida et al., 2019, Lux and Haidn, 2009, Theron et al., 2019]. The studies cited above have reported that the signal-to-noise ratio is higher in the case of OH* emission. Moreover, very similar overall flame structures were observed using both OH* and CH* radicals. Therefore, the OH* chemiluminescence alone is used in this work to characterize the flame structure.

The visualization of the reaction zone using OH* chemiluminescence is made possible by an intensified UV imaging system setup, shown schematically in Figure 3.4 together with the backlighting imaging setup used simultaneously. The chemiluminescence system consists of an intensified high-speed imager (HS-IRO from LaVision) and a high-speed camera (Phantom VEO710 from Vision Research), with a lens adapted to ultraviolet light and a filter adapted to the spectral signature of the OH* radical. The focal length of the lens is fixed at 100 mm, with an aperture f/2.8. The OH* filter mounted on the UV lens has a maximum transmission of 70% at 310 nm and a 10 nm half-width. The intensifier is set with a fixed gain and an exposure time of 5 µs.

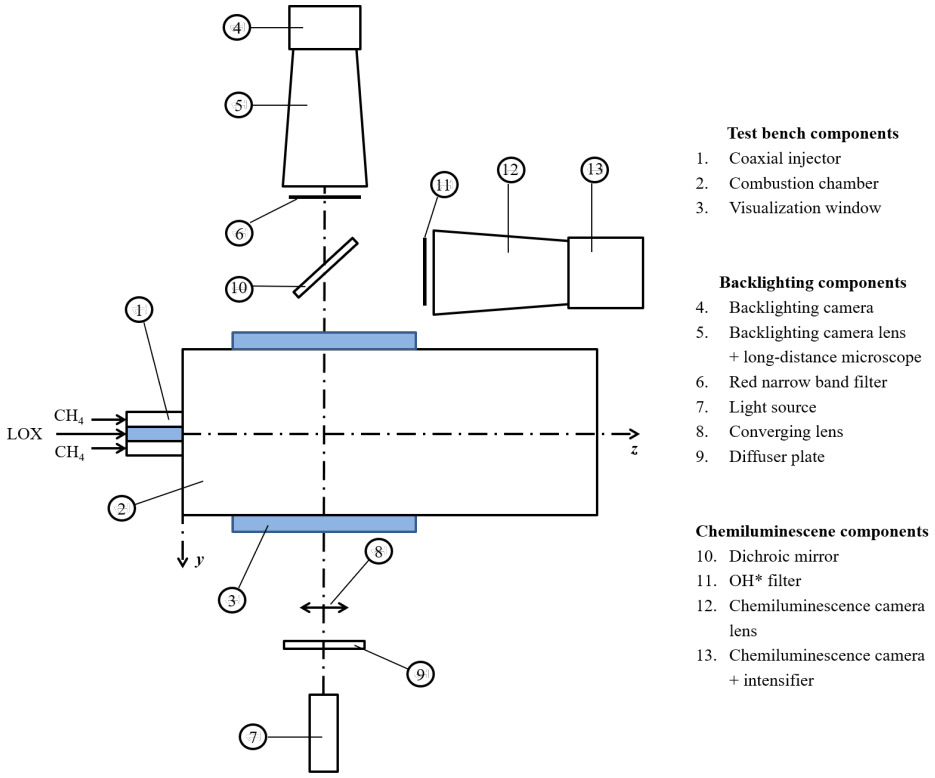

FIGURE 3.4: Backlighting and chemiluminescence imaging setup used to record images simultaneously at the MASCOTTE test bench.

3.1.3.2 Backlighting imaging

The liquid oxygen injected into the combustion chamber is visualized using a backlighting imaging technique. The visualization of the liquid phase is composed of a collimated light source positioned opposite from a recording sensor (camera), and illuminating the flow field from behind through the combustion chamber. The dense liquid phase transmits only a small amount of the incident light compared to the surrounding gaseous phase. The amount of light reaching the camera on the opposite side of the flow field depends therefore on the medium through which it passes inside the combustion chamber. This results in recorded images showing the liquid phase in black (due to the low light transmission) while the gaseous phase appears in bright colors. Figure 3.5 shows a schematic representation of the technique. It shows the backlighting visualization of a liquid jet (colored in blue) as it leaves the injector. The light from the source passes through a collimating lens before reaching the flow. The transmitted light then reaches the camera, producing an image. The recorded image shows, in black, the projected area of the illuminated liquid phase. This technique is a classic visualization method for liquid-gas flows and is commonly used in the study of liquid atomization. The high contrast of the resulting images allows to easily identify the liquid phase and its dynamics.

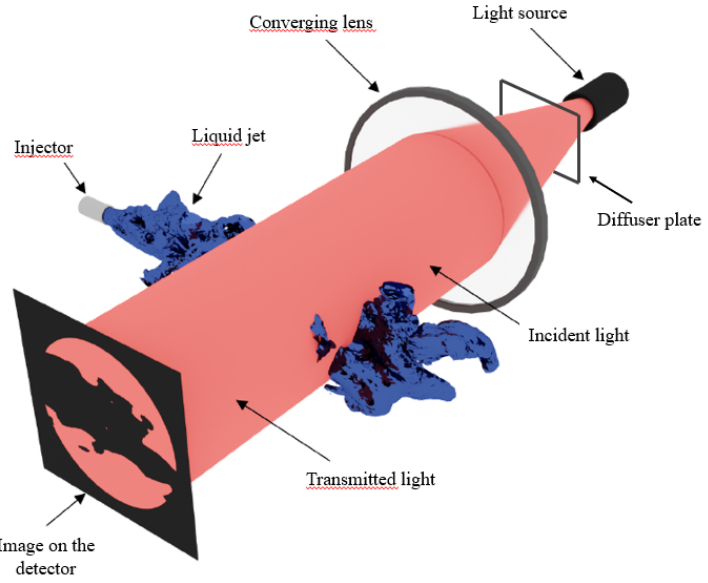

FIGURE 3.5: Schematic representation of the backlighting imaging technique from Lechner [2024].

The backlighting setup used to record images of the LOx atomization process in the MASCOTTE test-bench is shown schematically in Figure 3.4 where the main components of the setup are detailed. Two different setups were used. The first setup (1) was used to record large-field, low-resolution images covering the entire optical window of the test chamber. The second setup (2) was used to record small-field, high-resolution images showing a small portion of the liquid-gas interface. Setup 1 is used simultaneously with the OH* chemiluminescence setup presented previously, while Setup 2 is used alone, in dedicated test runs, once the large-field images are obtained.

In Setup 1, the camera used is a high-speed Phantom V711 camera from Vision Research whose CMOS sensor is composed of 1280 x 800 squared pixels of 20 µm side length. The camera is equipped with a Nikon lens of 200 mm focal length. The light source is a Cavilux Smart 400 W laser emitting a red incoherent light pulse at a wavelength of 640 ± 10 nm. The pulse duration is set at 30-40 ns to freeze the flow appropriately. A diffuser plate is placed between the light source and the converging lens to ensure a more homogeneous background. The converging lens is placed between the diffuser plate and the chamber to produce parallel light rays that pass through the combustion chamber. A narrow band filter is placed in front of the camera lens to select only the light from the laser source, while blocking light from the flame emission. This setup results in images covering a field of 76.8 mm x 48 mm with a spatial resolution of 60 µm/pixel. Images are recorded during the steady-state flow phase at a frequency of 2000 fps.

In Setup 2, the camera used is a low-frequency JAI GOX-2402 with a sensor of 1920 x 1200 squared pixels of 3.45 µm side length. The camera is equipped with a long-distance microscope Infinity K2 DistaMax with a CF1/B lens. This high magnification imaging

system has a very small depth of focus (of the order of 80 µm) whose focus plane is positioned at the vertical median plane of the injector. The light source configuration is the same as in Setup 1. The pulse duration is set at 1-1.5 µs, which allows to freeze the liquid flow. A narrow band filter is also used to block light from the flame emission. This setup results in a smaller field of view of 8.64 mm x 5.40 mm, with a spatial resolution of 4.5 µm/pixel. This near-field imaging system is positioned to capture images covering small portions of the flow near the liquid-gas interface in a zone where textural atomization is at its most intense. The high-resolution images are recorded at a frequency of 50 fps during the steady-state flow phase.

3.1.4 Visualization results

A dedicated fire-test was run for each of the operating conditions of Table 3.1 to record simultaneous backlighting and OH* chemiluminescence images during the steady-state phase of the flow. The large-field images provide a global view of the flame structure and of the atomization process from the injector exit plane to approximately 70 mm downstream. Moreover, these images are used to define the positions of the high-resolution, near-field images that are recorded using Setup 2 in dedicated test-runs for each position represented as white rectangles in Figure 3.6(a). A qualitative description of the visualized flow is provided in the following.

Large-field flow visualization

Figures 3.6–3.8 report large-field visualizations of the flow during the combustion process under the *RB* operating conditions. Figure 3.6(a) depicts an instantaneous backlighting image recorded using Setup 1. It shows the liquid oxygen jet (in black) as it is injected into the combustion chamber through the central tube of the coaxial injector (positioned at $z = 0$). The surrounding gaseous CH_4 flow is transparent, but its presence is marked by a visible contrast pattern near the liquid-gas interface close to the injector ($z < 12$ mm approximately). This contrast pattern is the result of gradients of the optical refractive index of the medium, caused by density and species gradients in the reactive flow. These gradients, in turn, originate from the combustion process taking place in this region. The figure also shows the presence of liquid deposits on the optical windows, between $z = 13$ mm and $z = 20$ mm approximately. Liquid deposits are always observed during the testing of the operating conditions considered here. These liquid deposits are likely water, produced in the combustion process, that condensated on the cold injection plate and are pushed towards the optical windows by the Helium film used to protect the windows from the strong thermal gradients. Figure 3.6(b) shows an instantaneous OH* radical chemiluminescence and indicates the position of the flame front, in false colors, at the same instant as the one depicted in Figure 3.6(a).

Time-averaged backlighting and chemiluminescence images are shown in Figures 3.7(a) and 3.7(b) respectively. Figure 3.7(a) shows in black the zones that always depict liquid phase and in gray the zones that contain either liquid or gas phases, depending on the instant. These gray regions are associated with the perturbation of the interface. These perturbations can originate from large-scale undulations of the jet or from the development of ligaments at the liquid-gas interface. The development of ligaments is at the origin of the textural atomization process, and the zones where this happens must therefore be studied in detail. The figure also shows that the liquid deposit seen in the instantaneous and time-averaged images as a vertical bead remains in the same position and has an almost identical shape as in Figure 3.6(a). This means that it does not move significantly during the image recording time sequence. The zone covered by the liquid deposits are not considered in this study as it prevents the clear visualization of the liquid oxygen flow in that region.

To locate the average reaction zone, the Abel transform of the time-averaged OH* emission image from Figure 3.7(b) is calculated. The Abel transformation is a deconvolution method used to transform the chemiluminescence images, which capture the integrated light intensity along the line of sight of the OH* flame emission, into time-averaged tomography-like images representing the radial profile of the OH* emission in a vertical median plane. The use of the Abel transform assumes that the time-averaged flame structure is axisymmetric. To test this assumption, the Abel transformation was performed separately on the top and the bottom halves of the time-average OH* emission image, and yielded similar results in both cases. Juniper et al. [2000] have studied a LOx-H_2 cryogenic flame structure using the OH* emission, and found that, even though some of the OH* emission is absorbed by the OH radicals present in the flame, the Abel transform of the OH* emission allows to detect the intense reaction zone. Figure 3.8 shows the superimposition of a time-averaged backlighting image (in grayscale) and of the Abel-transformed OH* time-averaged chemiluminescence image (in blue). The Figure 3.8 represents the average relative position between the reaction zone and the atomizing liquid jet. At the near-injector zone ($z < 15$ mm approximately), the flame is positioned very close to the liquid jet interface, inside the oxygen/methane mixing layer. At this position, the mist of fine droplets produced by textural atomization is quickly evaporated and consumed by the flame. This explains why no droplets can be observed in the near-injector zone in Figure 3.6(a). Further downstream, the flame spreads radially away from the liquid core. This is likely due to the presence of thicker liquid ligaments at the liquid-gas interface, as per the observations from the works of Wu and co-authors [Wu and Faeth, 1993, Wu et al., 1992, 1995], presented in Chapter 1. These thicker ligaments produce larger drops that take longer to evaporate. This allows the oxygen to move radially away from the liquid core axis before evaporating and being consumed by the flame.

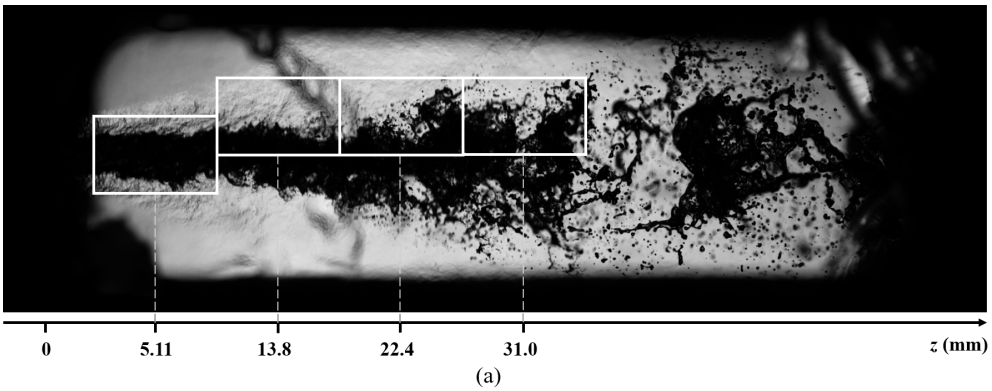

(a)

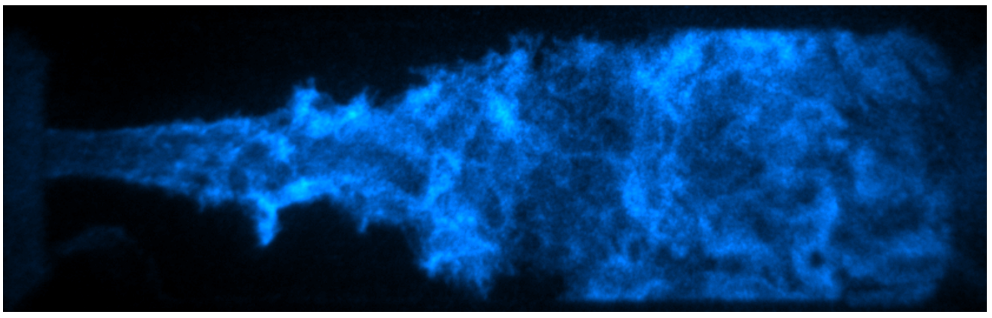

(b)

FIGURE 3.6: Large-field instantaneous images of OC *RB*: (a) backlighting; (b) OH* chemiluminescence. Both images are displayed at the same scale.

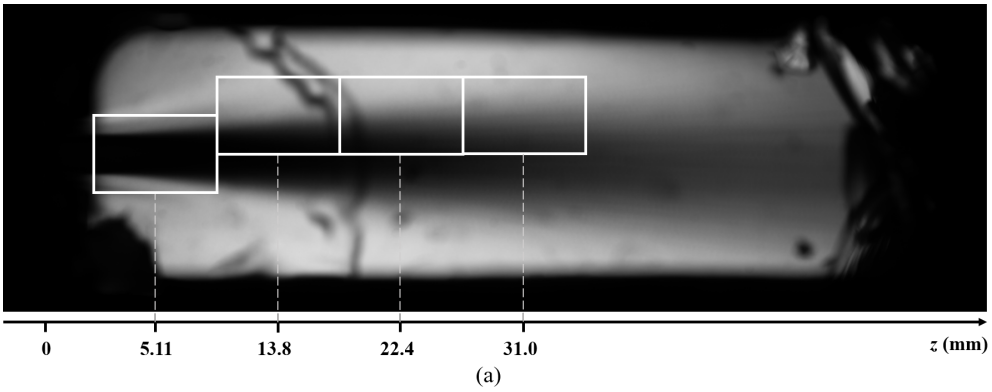

(a)

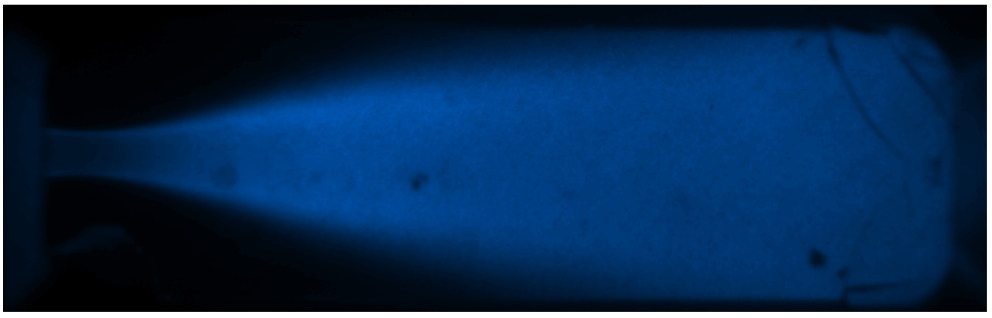

(b)

FIGURE 3.7: Large-field time-averaged images of OC *RB* recorded from the same test-run: (a) backlighting; (b) OH* chemiluminescence. Both images are displayed at the same scale.

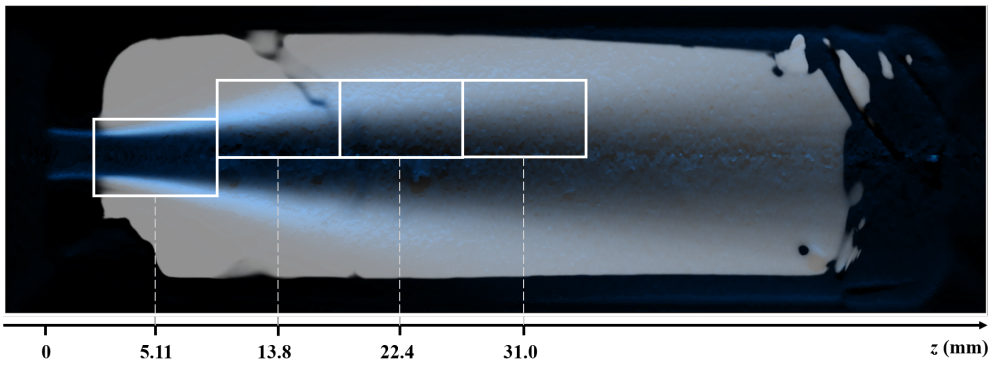

FIGURE 3.8: Superimposition of the time-averaged backlighting image and the Abel-transformed OH* chemiluminescence image of OC *RB* from the same test-run.

The presence of liquid ligaments issuing from the liquid jet can be observed in Figure 3.6(a). As observed in the works of Wu and Faeth [1993], Wu et al. [1992, 1995], very small and thin ligaments are present in the near-injector region and produce a spray of fine droplets. This has also been observed by Fdida et al. [2016] for similar operating conditions. These small-scale liquid structures and their breakup are mostly associated with a textural atomization process. As the small-scale turbulent fluctuations in the liquid phase dissipate, only larger fluctuations reach more downstream positions. As a result, thicker and longer ligaments are observed as the flow moves downstream. These thicker ligaments show less textural features and their breakup is mostly associated with a structural breakup process.

The study of textural atomization requires access to these small-scale structures in the near-injector region. From Figure 3.6(a) it can be concluded that these structures are not fully captured by the large-field visualizations obtained with Setup 1 due to the insufficient optical resolution of the considered backlighting imaging system. Moreover, it has been shown in Chapter 2 that the multi-scale description requires images of high spatial resolution in order to yield satisfactory small-scale measurements. There is therefore a strong need for images with higher spatial resolution to allow an accurate description of the textural ligaments and of their breakup. Such high-resolution images were obtained using the backlighting Setup 2. Since the backlighting Setup 2 results in images with a smaller field-of-view, multiple image positions are necessary to cover the textural atomization zone. Images were recorded at four different positions, as represented by white rectangles in Figures 3.6(a), 3.7(a) and 3.8. The distance z of the center of each image to the injector exit plane is also shown in the figures. These positions were chosen to capture the liquid-gas interface at increasing distances z from the injector. The resulting near-field, high-resolution images are presented in the following.

Near-field flow visualization

Figures 3.9(a) and 3.9(b) report instantaneous near-field, high-resolution backlighting images of OC *RA* recorded using Setup 2 at positions $z = 5.11$ mm and $z = 22.4$ mm,

respectively. Figure 3.9(a) shows the LOx jet as it leaves the injector. The image is vertically centered on the injection axis. Both the upper and lower interfaces are therefore visualized. Figure 3.9(b) on the other hand shows only the upper half of the jet, and therefore only the upper interface.

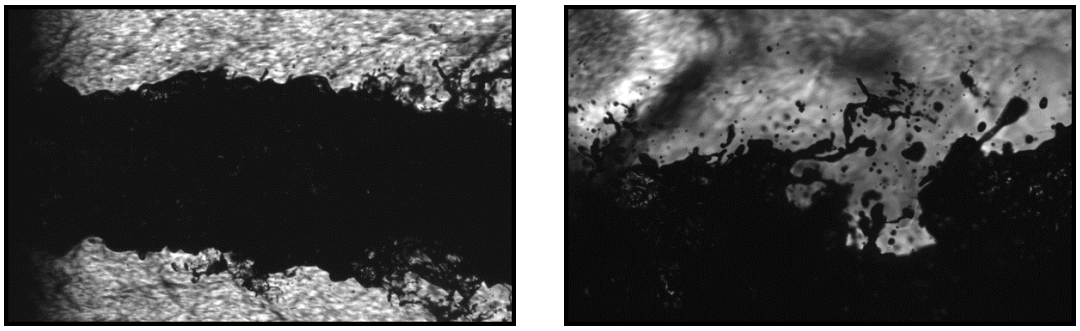

(a) (b)

FIGURE 3.9: Instantaneous high-resolution near-field backlighting images of OC *RA* at position (a) $z = 5.11$ mm and (b) $z = 22.4$ mm.

The gaseous medium around the liquid jet in Figure 3.9 appears as a corrugated grayscale ripple-pattern. Similar to the effect observed on the large-field backlighting images, this pattern is the result of optical refraction index gradients in the medium caused by the presence of the flame. These effects are more visible in the near-field visualizations, and are more intense near the injector exit, where the reaction zone sits very close to the liquid jet (as observed in Figure 3.8).

The near-field visualizations allow to observe the small-scale features of the liquid-gas interface. The observed interfaces show deformations that can be described as textural. Small, textural ligaments which themselves show textural deformation are also observed. Very few droplets can be observed in Figure 3.9(a) since these are quickly consumed by the flame. A higher number of droplets are present in Figure 3.9(b), however. These droplets are the results of the breakup of the ligaments present at the interface, and appear in various sizes. The size of the larger droplets is similar to the diameters of the thicker sections of the textural ligaments. These near-field images are later used in Chapters 4 and 5 to describe the textural atomization process.

3.2 Non-reactive flow: the MARACA air/water case

With the common goal of studying liquid rocket engine coaxial atomization, a test-case was defined in a collaboration between CNES, ONERA and CORIA. The goal of this test-case is to serve as a benchmark for experimental and numerical studies of atomization processes. The test-case is named *PF-ONERA*. A non-reactive, air-water coaxial flow is considered. The injection conditions correspond to a fiber atomization regime, representative of liquid rocket engines operating in subcritical regimes.

The *PF-ONERA* case is a particular case of an ensemble of fiber regime injection conditions studied experimentally at CORIA on the MARACA test-bench by Baillot et al. [2009] and Ficuciello et al. [2017], where liquid Reynolds numbers of up to $Re_l = 3200$ and gaseous Weber numbers of up to $We_g = 224$ were tested, with an ambient (chamber) pressure $P_c = 1$ bar. To limit the restitution time of numerical simulations, the *PF-ONERA* operating conditions have been defined by Rutard et al. [2020] with the highest possible liquid average velocity V_l at the injector exit allowed by the experimental MARACA test-bench. The air-stream average velocity at injection was also increased to maintain the fiber regime configuration. This resulted in higher Re_l and We_g numbers than those tested experimentally by Ficuciello et al. [2017] (more details on the operating conditions are given in Table 3.2).

The *PF-ONERA* (and different slightly modified versions) were tested experimentally by Herrera Leclerc [2022] and simulated numerically by Rutard et al. [2020], Granger [2023], Hoarau et al. [2024]. From the experimental point-of-view, most research has focused on the effects of acoustic forcing on the atomization process. Numerical studies have focused on the physical phenomena including acoustic effects as well as on the development of LES atomization models. Both experimental and numerical results based on the *PF-ONERA* test case are used in this thesis.

This section presents the experimental work done at CORIA by Herrera Leclerc [2022] and team, and the DNS simulation performed at ONERA by Hoarau et al. [2024]. Images issuing from these works are later used in Chapter 5 as input to the multi-scale method introduced in Chapter 2.

3.2.1 Experimental MARACA investigation

The experimental investigation of the non-reactive test-case named here *PF-ONERA-Exp* is performed at CORIA on the MARACA (Moderate Ambient pRessure Acoustic ChAmber) test bench, shown schematically in Figure 3.10. Designed with the goal of studying the effects of forced non-linear acoustics on atomization processes, the bench consists of a pressurized resonant acoustic cavity, a liquid-gas injection system, a loudspeaker system, an acoustic acquisition device and optical diagnostics.

The pressurized acoustic cavity allows to reach ambient pressures of up to 5 bar. It contains accesses to allow the connection to four loudspeakers used for the acoustic forcing (not used in the current case). It is also equipped with optical windows near the injection plane to allow the visualization of the flow. The injection system is composed of a coaxial injector of inner (liquid) post diameter D_l and outer (gaseous) diameter D_g at the outlet. Figure 3.11 shows a drawing of the injector.

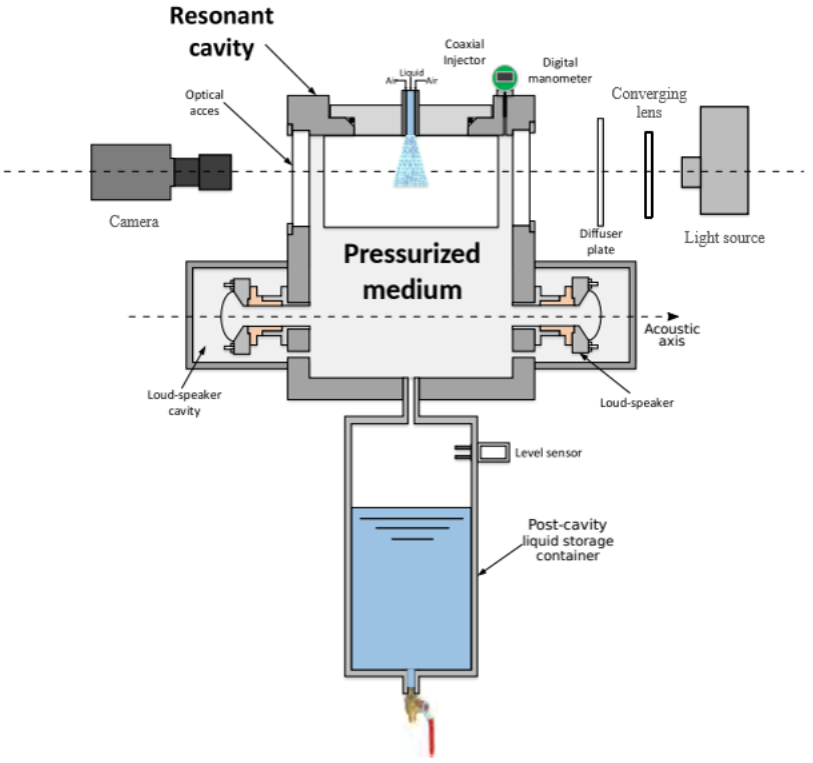

FIGURE 3.10: MARACA pressurized acoustic cavity main components and backlighting visualization setup, adapted from Herrera Leclerc [2022].

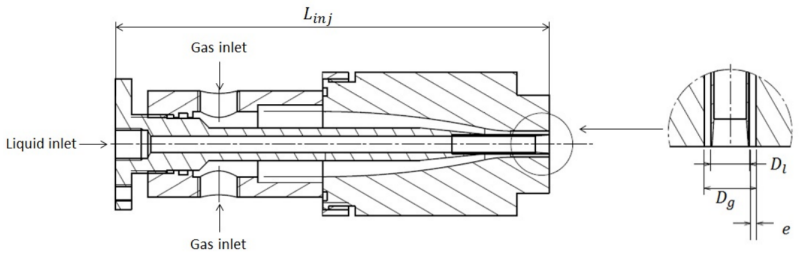

FIGURE 3.11: Drawing of the coaxial injector with a close-up view of the injector outlet, from Ficuciello et al. [2017].

The ambient pressure is $P_c = 1$ bar and the injected fluids are water and air, both at ambient temperature. The average velocity of the liquid water jet at the injector exit is $V_l = 1.1$ m/s. The liquid Reynolds number (based on D_l) is $Re_l = 6600$. The annular air stream average velocity is $V_g = 72.4$ m/s at the injector exit and the gaseous Weber number is $We_g = 520$. The parameters defining the tested operating conditions (named *PF-ONERA-Exp*) are summarized in Table 3.2.

The optical diagnostic system used for visualizing the atomization process is a diffuse backlighting system. The imaging setup seen in Figure 3.10 is composed of a pulsed light source (CaviLux 200 W laser from Cavitar), with a 10 ns pulse duration, and a

TABLE 3.2: Non-reactive flow experimenal and simulated operating conditions

OC	P_c (bar)	J	Re_l	We_g
PF-ONERA-Exp	1	5.1	6600	520
PF-ONERA	1	4	$\sim 10^4$	490
PF-ONERA-Similitude	10	4	$\sim 10^4$	490

Baumer BGAPI2 camera recording 8-bit images of 7920 x 6000 squared pixels at 5 fps. The camera is equipped with a Nikon 105 mm lens. A converging lens is used to focus the incoming light, and a diffuser plate is placed between the light source and the cavity to ensure a homogeneous background. The position of the diffuser plate constitutes the only difference with regards to the backlighting setup used for flow visualization in the MASCOTTE imaging setups presented in Section 3.1.3.2, where the diffuser plate was located between the light source and the converging lens. The positioning of the diffuser plate at the MARACA bench results in a very homogeneous background that facilitates the image post-processing procedure introduced later in Chapter 4.

The images recorded using the diffuse backlighting technique cover a field of approximately 111 mm x 84 mm with a spatial resolution of approximately 14.1 µm/pixel. An instantaneous backlighting image is presented in Figure 3.12. On the top, the figure shows a backlighting image (with some contrast correction to allow a better visualization of the flow) covering almost the entirety of the flow field.

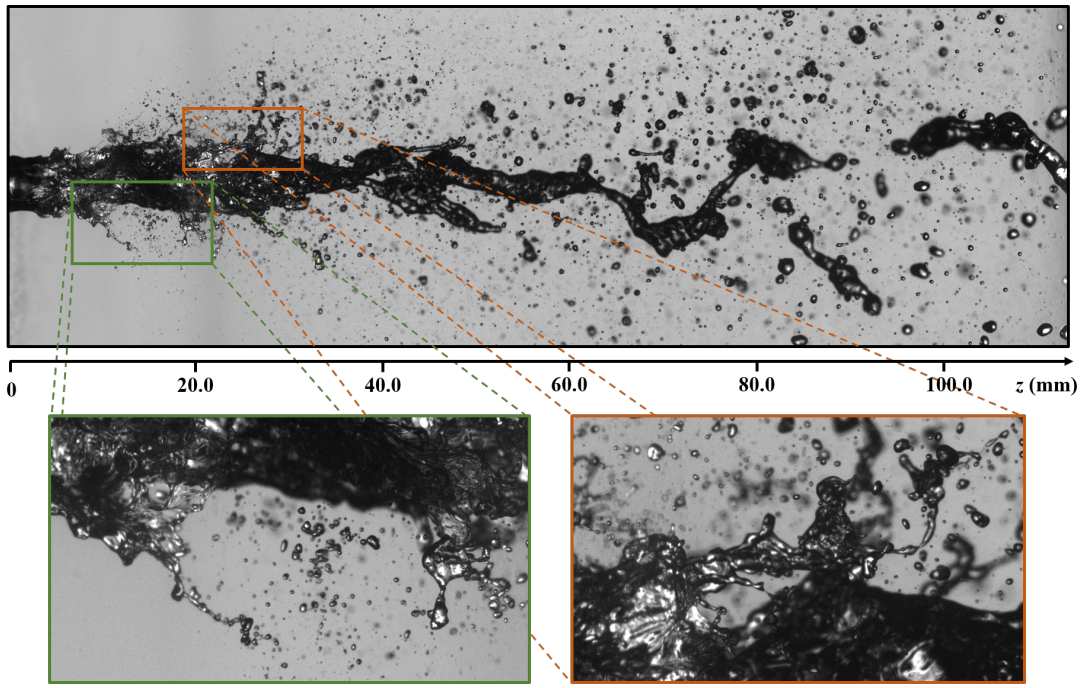

FIGURE 3.12: Diffuse backlighting image from the MARACA test-bench with two close-up views of small-scale features at the interface.

Near the injector exit ($z < 10$ mm approximately), the liquid core shows undulations related to the interface destabilization, likely in the form of a Kelvin-Helmholtz instability [Marmottant and Villermaux, 2004]. Almost no ligaments are observed in this zone. Further downstream, the interface begins to show the presence of ligaments. Two rectangular close-up views are shown at the positions indicated by the green and yellow rectangles. The close-up views show some of the small-scale ligaments located near the interface in this zone and some of the droplets they produce. Similarly to the MASCOTTE case, these ligaments show textural deformation. The textural deformation can be observed for example on Figure 3.12, where small-scale ligaments are peeled from the interface. The close up-views show that even the textural ligaments can show textural deformation. In his work on the direct numerical simulation of this atomization configuration, Hoarau et al. [2024] found that the region ranging from approximately one to four times the diameter of the liquid injector in the z direction (zone covered by the two close-up views) is responsible for the largest droplet density in the flow field. This region was called the *atomization zone*. Most of the textural ligaments observed in Figure 3.12 are inside this so-called atomization zone. As the flow moves downstream (right half of the image), the ligaments become thicker and show more structural, large-scale deformation. Very few ligaments are observed downstream, and the liquid core itself appears as a thick ligament with structural deformation.

3.2.2 Direct Numerical Simulation of the MARACA case

Simulations were performed by Hoarau et al. [2024] with the goal of studying a fiber regime atomization process in conditions representative of liquid rocket engines. The simulated configuration is based on that of the MARACA experimental investigation presented previously. The operating conditions used by Hoarau et al. [2024] correspond to a modified version of the *PF-ONERA*. For numerical robustness and stability reasons, the chamber pressure is changed to 10 bar. This modification was made to reduce the density ratio between the liquid and gas phases. Dimensionless numbers (Re_l, We_g and J) are kept identical to the *PF-ONERA* to ensure that the atomization regime remains the same. The modified *PF-ONERA* operating point is therefore named *PF-ONERA-Similitude*. The main parameters defining the *PF-ONERA-Similitude* operating conditions are summarized in Table 3.2. More recently, another simulation was performed with operating conditions identical to the *PF-ONERA* (with real liquid/gas density ratio), also summarized in Table 3.2.

This section presents the DNS code, the simulation setup, the operating conditions, and some results from simulations of the *PF-ONERA-Similitude* case reported by Hoarau et al. [2024]. Then, results from the recent *PF-ONERA* simulation are used to produce images that will be used later in Chapter 5 to study the textural atomization process and compare it with the experiments.

3.2.2.1 The DyJeAT code

The numerical code used to simulate the MARACA atomization process observed experimentally is the DyJeAT (Dynamics of Jet Atomization) code. Developed in the PhD works of Couderc [2007], Zuzio [2010] and Marter [2017], it allows the simulation of incompressible two-phase flows. Before being applied to the current coaxial assisted atomization configuration [Hoarau et al., 2024], the DyJeAT code has been used to simulate other complex two-phase processes such as the impact of droplets on dry or wet solid walls [Xavier et al., 2020], the atomization of a liquid jet in a crossflow [Zuzio et al., 2020], and the assisted atomization of liquid sheets [Averseng et al., 2019, Zuzio et al., 2018].

The simulations involve the direct numerical resolution of the incrompressible Navier-Stokes equations using a one-fluid sharp interface method. The code makes the following assumptions about the flow: the flow is incompressible, the fluids are Newtonian, there is no heat exchange and no phase transition, and the interface is infinitely thin. Using these assumptions, the Navier-Stokes equations are solved on a cartesian structured uniform mesh. The interface is tracked using a Level-Set method coupled to a Volume-of-Fluid approach (CLSVOF) to ensure mass conservation [Hoarau et al., 2024]. A piecewire linear interface calculation (PLIC) interface reconstruction method [Youngs, 1982] is used to approximate the interface topology in each cell by a plane. More details about the numerical implementation can be found in the references cited above.

3.2.2.2 Simulation setup and main results

To keep simulation costs affordable, the simulation domain is reduced to a rectangular box of side lengths $L_x = 5.8D_l$, $L_y = 5.8D_l$, $L_z = 18.6D_l$, where z is the direction defined by the injection axis. The domain includes a portion of the injector corresponding to a length of $L_{inj} = 1.8D_l$. The simulated coaxial injector is shown in Figure 3.13. Its geometry is identical to the one used in the MARACA experiments presented previously. The liquid injection post diameter is named D_l and the thickness of the inner lip is named δ_{lip}. Both the injector and the domain's back wall (back wall of the chamber) are modeled using an immersed interface method described by Marter [2017].

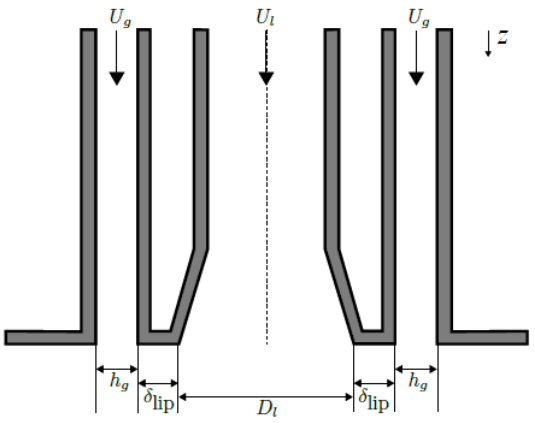

FIGURE 3.13: Simulated coaxial injector geometry.

The liquid and gas flows are injected into the domain with Dirichlet boundary conditions imposing the velocity, VoF and Level-Set fields with uniform profiles. No turbulence is injected, but the inclusion of a portion of the injector in the domain helps to establish more realistic flow conditions at the injector exit, although it is not long enough to reach well-established turbulence levels. An outflow boundary condition is set for all other faces of the domain.

The computational mesh is a uniform cartesian grid. The required mesh size dx was estimated using the correlation reported by Marmottant and Villermaux [2004] for the average "size" $\langle D_0 \rangle$ of ligaments issuing from a coaxial assisted atomization process: $\langle D_0 \rangle \approx 0.23\lambda_T$, where λ_T is the wavelength of the transverse interfacial perturbations. Considering the injected flow conditions of the *PF-ONERA-Similitude*, the correlation yields $\langle D_0 \rangle \approx 0.55\delta_{lip}$. The exceptional computational resources available allowed for a mesh size of $dx = 0.17\delta_{lip}$, which allows to impose three cell points to resolve the main liquid ligaments, for a total of nearly three billion cells.

The simulation time-step is imposed to meet the condition of a maximum CFL number of 0.5. This results in time-steps of around $1.8\text{x}10^{-7}$s once the transient regime is finished.

The analysis from Hoarau et al. [2024] is performed considering the established flow regime only. An estimation of the duration of the transient regime at the beginning of the simulation is done using a characteristic velocity that takes into account both the liquid- and gas-flow injected velocities, U_l and U_g, as well as their interaction through the momentum flux ratio J. The characteristic velocity considered is defined as:

$$U_w = \frac{U_g + JU_l}{1 + J} \tag{3.1}$$

Once this characteristic velocity is determined, the flow-through time (i.e. the time required for the main liquid structures to traverse the entire domain) is calculated as

$\tau_w = L_z/U_w$. For the operating conditions of the *PF-ONERA-Similitude* simulation, the estimated flow-through time is $\tau_w \approx 0.018$s. Hoarau et al. [2024] considered that the flow was established after two flow-through times. The transient regime was therefore considered finished at $t = 0.036$s.

Two other quantities were used to monitor the establishment of the flow: the liquid core length and the number of small droplets (droplets of characteristic length in the $[0, 5dx]$ range). Figure 3.14 plots the time evolution of both quantities. A vertical solid line represents the end of the transient regime (at $t = 0.036$s). Both plots indicate that the estimated transient time value is appropriate, since the measured quantities reach a fairly established regime after that time.

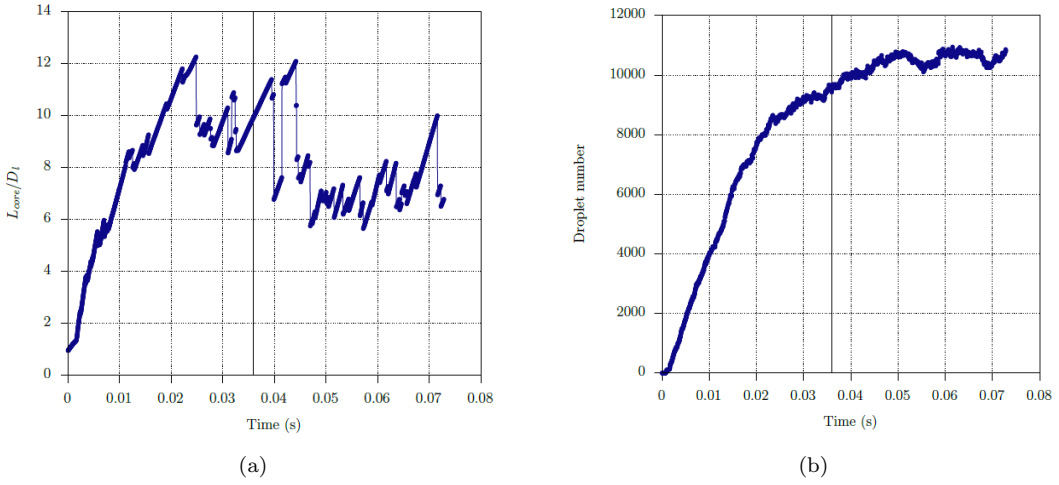

FIGURE 3.14: Convergence criteria from Hoarau et al. [2024]: (a) liquid core length normalized by D_l; (b) number of small droplets.

An instantaneous view of the simulated flow field is shown in Figure 3.15. The figure consists of a realistic visualization of the 2D projection of the 3D simulated liquid-gas flow by ray-tracing, achieved by Granger [2023].

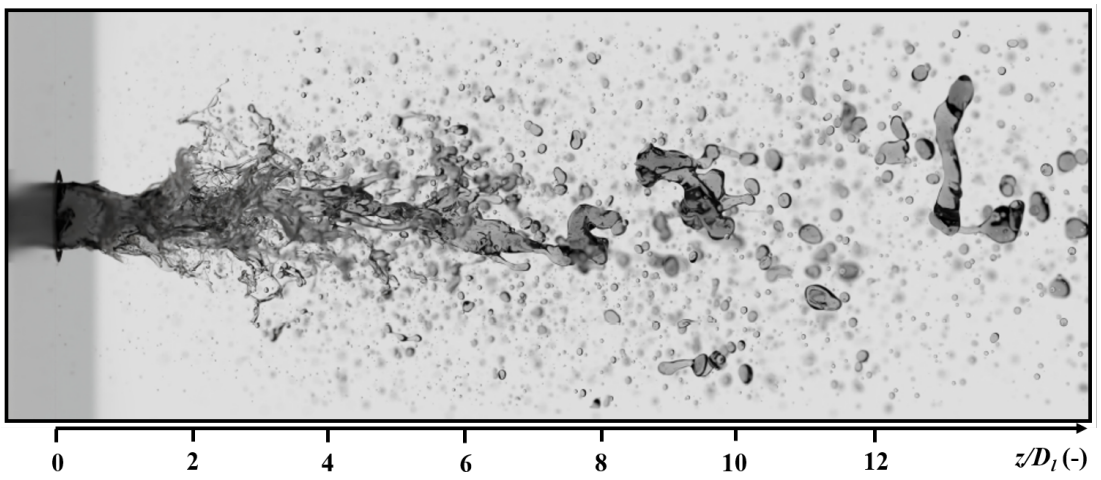

FIGURE 3.15: Ray-tracing visualization of the DNS simulation of the *PF-ONERA-Similitude*, from Granger [2023].

The results reported by Hoarau et al. [2024] include global and local information on the simulated liquid structures (liquid core, ligaments and droplets). Figure 3.16 shows the spatial distribution of droplets resulting from the measurement of the density of droplets (defined as the number $(\bar{N}b)_\theta$ of resolved droplets inside squared macro-cells of 800 µm size divided by the volume V_{MC} of the macro-cell) at different spatial positions, during the established regime. Three zones are identified by the authors. Zone 1 is named the *destabilization zone* and is characterized by the appearance of surface instabilities on the liquid core interface, but with very few ligaments and consequently very few droplets being produced. This behavior can be visualized in Figure 3.15 in the zone near the injector exit. Zone 2, named *atomization zone*, is where the droplet density is at a maximum. This is the consequence of the large number of textural ligaments produced in this zone, as seen in Figure 3.15. Zone 3, named *stabilization zone*, is characterized by the presence of larger ligaments undergoing a structural breakup process. These ligaments correspond to the part of the liquid core that did not break up as textural ligaments. These structures travel at low velocities in a direction aligned with the injection axis.

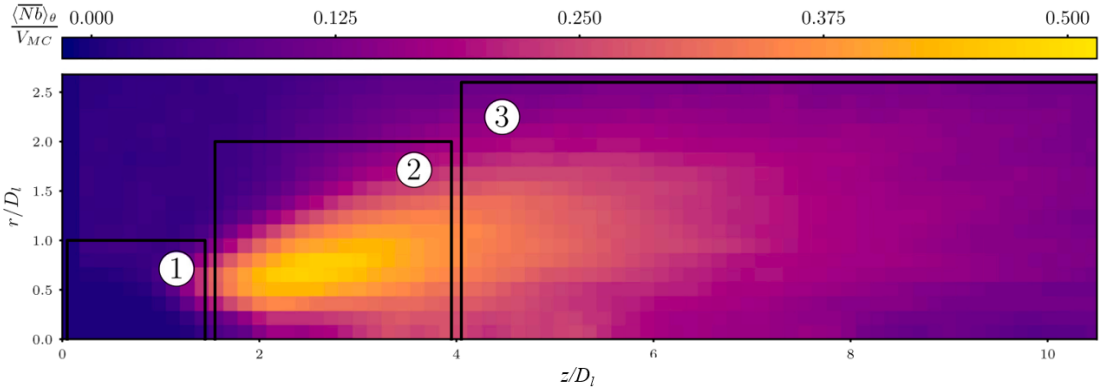

FIGURE 3.16: Droplet spatial distribution from Hoarau et al. [2024].

3.2.2.3 Simulated flow visualization for multi-scale measurements

The simulation results used in this thesis are the ones corresponding to the *PF-ONERA* operating conditions obtained recently at ONERA. To reduce the transient time, the simulation was initiated taking as initial conditions the last time-step of the *PF-ONERA-Similitude* simulation from Hoarau et al. [2024]. Using the characteristic velocity from Equation 3.1, the flow-through time was estimated as $\tau_w \approx 0.006$s, which corresponds to one-third of the flow-through time of the *PF-ONERA-Similitude* case. The transient time is expected to be shorter than in the previous case.

The total simulated time was of 0.042s. The results considered here were recorded during the established regime, starting at $t = 0.024$s (four times the flow-through time). The time-step during the established regime was of approximately 6.6x10^{-8}s.

The resulting liquid core length was measured between $t = 0.0024$s and $t = 0.0042$s using an image-based method. Figure 3.17 plots the time evolution of the liquid core length L_{core}, normalized by the liquid injector diameter D_l. The evolution of the liquid core length indicates that flow is indeed established during the considered time interval.

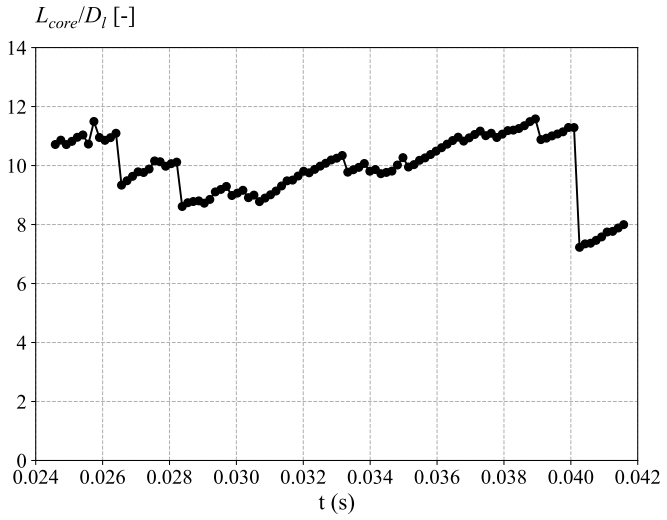

FIGURE 3.17: Time evolution of the liquid core length L_{core} normalized by D_l.

The liquid flow-field is visualized in Paraview. The liquid-gas interface is visualized as an iso-surface at zero level-set ($\phi = 0$) colored in black. Images are then produced every 2500 time-steps, or approximately every 0.165 ms, as a 2D projection of the 3D simulated interface. The visualization field is set by a digital camera setup with infinite depth-of-field. This results in structures that are always sharp and in focus. The resulting image resolution is chosen to be identical to the experimental images obtained in the MARACA test-bench. Paraview uses a bilinear interpolation technique (similar to the one described in Chapter 2) to fit the simulation data results into the desired output image pixel-grid.

Figure 3.18 shows an example of the resulting 2D projected liquid-gas interface from the *PF-ONERA* simulation. The chosen visualization method yields images similar to the backlighting technique used to record images during experiments, as described previously. The resulting images show the liquid phase in black against a white background.

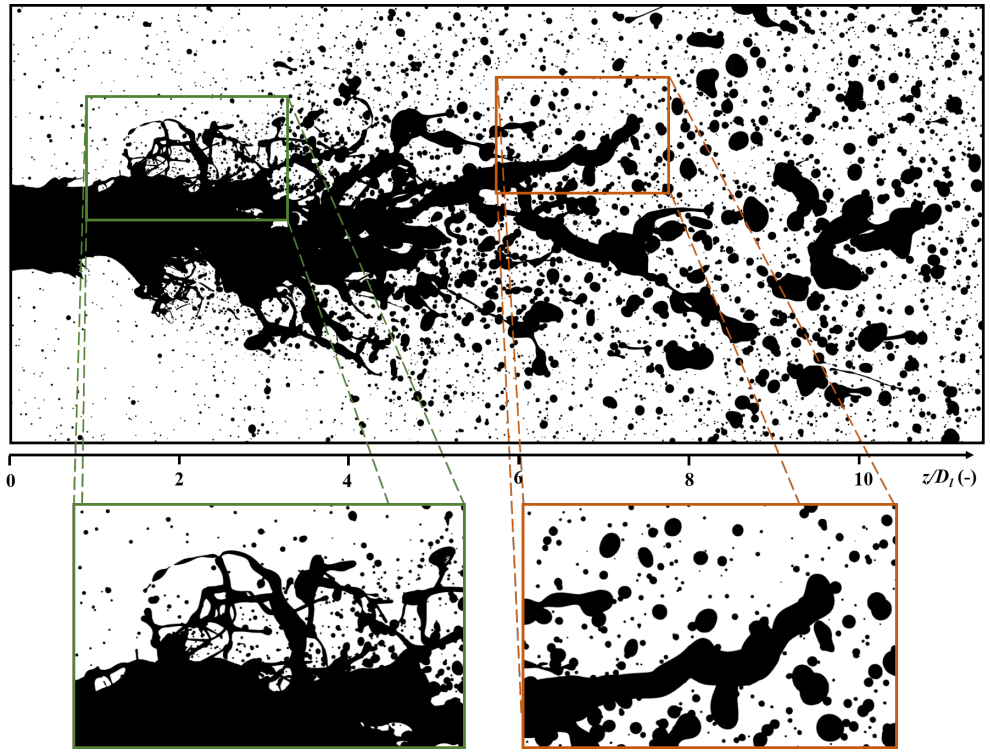

FIGURE 3.18: Instantaneous 2D projection of the $\phi = 0$ iso-surface (in black) of the *PF-ONERA* DNS simulation.

Similarly to the experiments, and to the observations from Hoarau et al. [2024], the observed liquid flow shows a region of interface destabilization near the injector exit, followed by a zone of intense textural atomization, where the interface shows a large number of thin ligaments that are peeled from the liquid bulk and that procude relatively small droplets (green close-up view window). Further downstream, a stabilization zone can be identified, where the liquid core evolves into thicker ligaments producing larger droplets (yellow close-up view). Some differences between the liquid flow visualization from the DNS (Figure 3.18) and from the experiment (Figure 3.12) can be identified. Firstly, the length of the liquid core is globally shorter in the DNS case. Another difference that can be noted is the length of ligaments in the *atomization zone*, which appear longer in the DNS compared to the experimental images. These differences may originate, at least partially, from differences in the injected flow between the two cases: as mentioned previously, no turbulence is injected in the numerical simulations, while in experiments the injector tube is sufficiently long to provide a fully developed turbulent flow at the exit. Nevertheless, these observations have to be confirmed by

deeper analyses. This is not in the scope of this thesis and will be investigated in future works.

3.3 Conclusion

Two fiber-regime assisted atomization study cases were introduced in this chapter. The main case considered is the reactive MASCOTTE case, which deals with the atomization of liquid oxygen assisted by a gaseous stream of methane. The combustion of the propellants results in conditions similar to those encountered in real liquid rocket engines operating at a subcritical regime. The experimental work done at the MASCOTTE test-bench during the PhD allowed to capture large- and near-field backlighting images of the atomization process. The high-resolution near-field images show the liquid-gas interface and its textural perturbation. The presence of textural liquid ligaments is observed in the near-injector region. These images are studied with the multi-scale method presented in Chapter 2 and the results are discussed in Chapters 4 and 5 to describe the oberseved textural ligaments and to analyze the textural atomization process.

The second case considered is the non-reactive MARACA case, which deals with the atomization of a jet of water assisted by an air flow. This case has been studied previously both experimentally and numerically. Results from previous works are presented. They include experimental backlighting images of the atomization process and backlighting-like images produced from data from a direct numerical simulation. These experimental and numerical images will be used in Chapter 5 to compare quantitatively characteristics of the atomization process observed experimentally and reproduced by the DNS simulation.

Chapter 4

Image processing and measurements

Before analyzing the textural deformation of the liquid-gas interface from the MASCOTTE LOx-CH_4 atomization case presented in Chapter 3, the experimental backlighting images must be processed. The goal of this chapter is to present the proposed post-processing methodology that allows the application of the multi-scale description introduced in Chapter 2 to capture the small-scale deformation of the interface observed experimentally. First, the main techniques used in the post-processing of the images are detailed. Next, the proposed image post-processing is applied to the recorded high-resolution experimental images at each position, allowing a qualitative description of the small-scale ligaments issuing from the textural atomization process. Finally, the multi-scale measurement technique introduced in Chapter 2 is applied to a set of processed images to determine the scale resolution obtained using the proposed methodology, and to ensure that the small-scale textural deformation is correctly captured in the measurements.

Contents

4.1 Experimental reactive image processing

As seen in Chapter 3, the experimental backlighting images recorded at the MASCOTTE test bench show the liquid phase in dark gray levels against a lighter gaseous background. The liquid phase visualized in the images includes the liquid core exiting the injector, the ligaments produced at the interface and other detached structures such as ligaments and droplets undergoing secondary breakup.

The multi-scale description of the liquid system using the technique presented in Chapter 2 requires that the system be depicted in binary images where the liquid phase appears as black pixels and the gas phase appears in white. The analysis of textural atomization processes, which is the scope of Chapter 5, focuses on the multi-scale description of the liquid ligaments before breakup. This requires that the images show only interfacial structures still attached to the liquid core. Any disconnected structures (ligaments and/or droplets) must therefore be eliminated from the binary images. Segmented images of the liquid system may show holes inside the liquid phase. These holes can have different origins: most holes are a result of light refraction during the backlighting image recording; other, less frequent holes can appear as a result of ligaments crossing each other. Indeed, in a 2D projection of the liquid system, the crossing of two ligaments appears, in the image plane, as a white hole surrounded by the liquid phase. The analysis of the liquid system, introduced in Chapter 2, considers liquid systems where the interface length $L(d)$ only decreases with the increase of the erosion scale d. For this condition to be met, the liquid system cannot contain holes inside the liquid phase. Lastly, as seen in Chapter 2, the scale distribution measurement requires high spatial resolution images in order to capture the small-scale features of the system without interference from the so-called pixelization effects. It is necessary therefore to ensure that images have a sufficient spatial resolution to allow the description of the small-scale textural ligaments at the liquid-gas interface. This is why the high-resolution backlighting images presented in Chapter 3 are used. In addition, a sub-pixel treatment is considered to increase even more the spatial resolution of these images.

The image processing steps applied to the backlighting images recorded at the MASCOTTE test bench are detailed in the following. Figure 4.1 shows the effect of each processing step on an instantaneous backlighting image of the LOx jet interface.

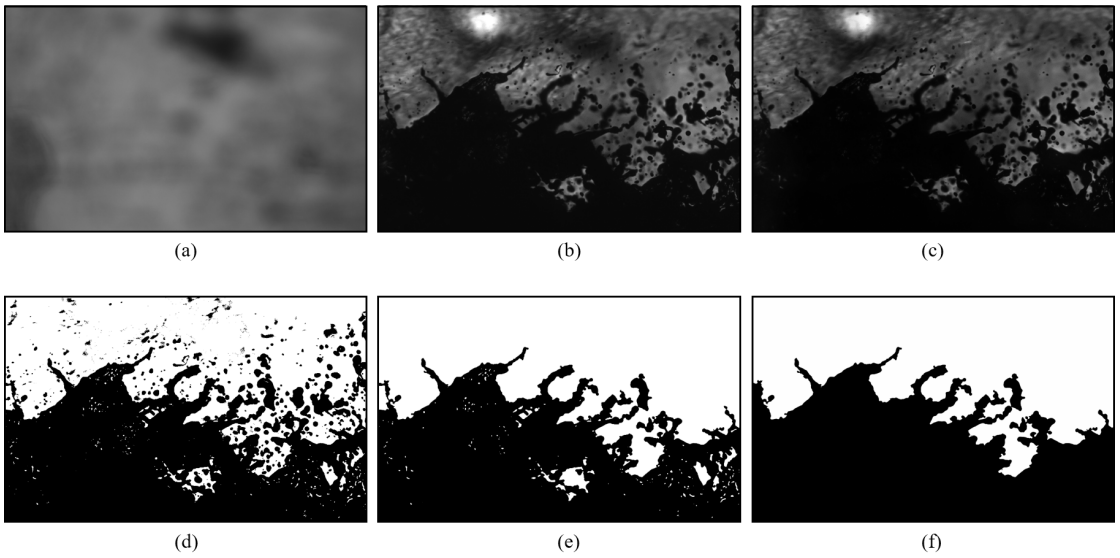

FIGURE 4.1: Image processing steps applied to an instantaneous backlighting snapshot (from OC *RA* at position $z = 22.4$ mm): (a) background image; (b) raw backlighting image; (c) normalization; (d) segmentation; (e) drop elimination; (f) hole filling. Corresponding field of view of 8.64 mm x 5.40 mm.

Normalization

The first processing applied on the raw backlighting images is called normalization. This step is performed to reduce spatial inhomogeneities of the image background which may be caused by a non-uniform lighting or by the presence of small deposits (soot, water, ...) on the optical windows. (The effect of deposits on the windows can only be eliminated by normalization if the deposits remain in a fixed position during the image recording process.) The normalization is done by dividing each pixel value of the raw backlighting image (Figure 4.1(b)) by the corresponding pixel value from the average background image recorded in the absence of the flow (Figure 4.1(a)).

The normalized image I_{norm} is obtained by applied the following operation on each image pixel:

$$I_{norm} = \frac{I - I_N}{I_{back} - I_N} \tag{4.1}$$

where I is the intensity of the raw backlighting image, I_{back} is the intensity of the average background image and I_N is the camera noise level, which is assumed to be very low here and is therefore taken as equal to zero.

The resulting normalized image (Figure 4.1(c)) shows a slightly more uniform background and better contrast between the liquid/gas phases, which facilitates the subsequent segmentation step.

Segmentation

The segmentation step consists in the separation of the liquid phase from the gaseous phase. As seen in Chapter 3, the backlighting technique yields grayscale images where the liquid phase appears in dark gray levels against a lighter background. The segmentation of the two phases relies on the definition of a threshold value that identifies each pixel as liquid or gas. Pixels whose intensities are below the threshold values are identified as liquid, and pixels whose gray levels are above the threshold are identified as gas. Once a given pixel is identified as either liquid or gas, a new intensity value is attributed to it, correspondingly: 0 for liquid or 255 for gas. This results in a binary image where the liquid pixels are black and the gas pixels are white.

The main difficulty lies in determining the threshold value. Different thresholding methods exist. In the most simple ones, commonly named *global thresholding methods*, a single global value is calculated from characteristics of the entire grayscale image. This unique threshold value is then used to classify pixels as either liquid or gas. These methods are sufficient to appropriately segment images where gray levels corresponding to either liquid or gas are easily distinguishable and uniform over the entire image.

The backlighting images considered here, however, show complex grayscale patterns introduced by variable lighting conditions, liquid evaporation, propellant combustion, etc. This means that global thresholding methods are unfit to deal with the large and inhomogeneous range of gray levels in the images. More complex methods, capable of taking into account this variation, are therefore necessary.

Local thresholding methods determine an individual threshold value for each pixel of the image, taking into account the characteristics of the neighboring region around said pixel. There are many methods available in the literature, most of which differ mainly in the local image characteristics considered in the calculation of the threshold value. Different methods were tested using ImageJ's *Auto Local Threhsold* function, and the Phansalkar Local Thresholding method, introduced by Phansalkar et al. [2011], was found to yield the best results (namely in terms of the correct segmentation of the very small ligaments observed at the interface) in the case of the MASCOTTE backlighting images. This method calculates a threshold value for each image pixel according to the following expression:

$$I_T = I_{avg}\left(1 + p\exp\left(-qI_{avg}\right) + k\left(\frac{I_\sigma}{R} - 1\right)\right) \tag{4.2}$$

where I_{avg} and I_σ are respectively the local mean and standart variation of the pixel intensities inside the neighboring region, $p = 2$ and $q = 10$ are fixed constants, and R and k are user-defined parameters. A fine-tuning of the two user-defined parameters was done to select the values yielding the best results visually. In the present case, R was taken equal to 0.5 while the k parameter varied between 0.4 and 0.7, depending on

the image position. The neighboring region used for local calculations was a circle of radius equal to 67.5 µm centered on the considered pixel. The resulting image is a binary system where the liquid is shown in black and the gas in white (Figure 4.1(d)). Note that the grayscale patters seen in the raw image, which result from optical index gradients in the gas phase, are almost completely eliminated, and the small liquid structures are correctly captured.

Droplet elimination

The detached liquid structures present in the images, i.e. ligaments and droplets undergoing breakup, must be eliminated from the analysis. The simplest way to do so is eliminating these structures from the segmented binary images. After the segmentation step, the ImageJ *Analyze particles* function is used to identify detached structures and eliminate them by coloring them white. Figure 4.1(e) shown an example segmented image after droplet elimination.

Hole filling

The white holes inside the liquid phase that persist after the segmentation step (see Figure 4.1(e)) are either a result of ligaments crossing each other or of optical effects. Holes related to optical effects are usually very small. These holes are not part of the atomization process and must be eliminated. Holes related to ligament crossing are usually larger, and are a physically relevant part of the liquid flow structure. These holes are mostly observed in regions of the flow where ligaments are long and therefore more likely to cross one another in the 2D projection. Almost no holes are seen in the near-injector region where ligaments are shorter. Farther from the injector, where the interface is more deformed and ligaments are longer, these holes are more likely to be found. The example represented in Figure 4.1 corresponds to a position far from the injector where ligament crossing is most likely (image centered at $z = 22.4$ mm).

The presence of holes in the liquid phase means that the system is likely no longer homeomorphic to a cylinder. The multi-scale method introduced in Chapter 2, however, considers only systems that are homeomorphic to 2D infinite cylinders. This means that all holes inside the liquid phase must the eliminated. This is achieved using the ImageJ *Analyze particles* function. Figure 4.1(f) shows an example segmented image after all holes are eliminated (filled with black).

To address the influence of eliminating holes formed in the 2D projection by the crossing of ligaments, the $e_2(d)_{,d}$ distribution is measured on images before and after the elimination of the corresponding holes. This is done for two example instantaneous images, one near the injector (position $z = 5.11$ mm) and one farther downstream (position $z = 22.4$ mm). Figure 4.2 shows the example images considered. Figures 4.2(a) and 4.2(b) show images positioned near the injector before and after hole elimination, respectively. Hachures are used to represent a zone removed from the analysis. Indeed,

the leftmost section of the image at position $z = 5.11$ mm reports a loss of signal due to insufficient lighting in the area caused by the shadow cast by the injector face plate and/or the borders of the optical window. Figures 4.2(c) and 4.2(d) show images positioned further downstream before and after hole elimination, respectively. Figures 4.2(a) and 4.2(c) contain only holes associated to ligament crossing. Other holes, caused by optical effects, were manually eliminated. These example images were chosen because they are representative of the flow structure at their respective positions.

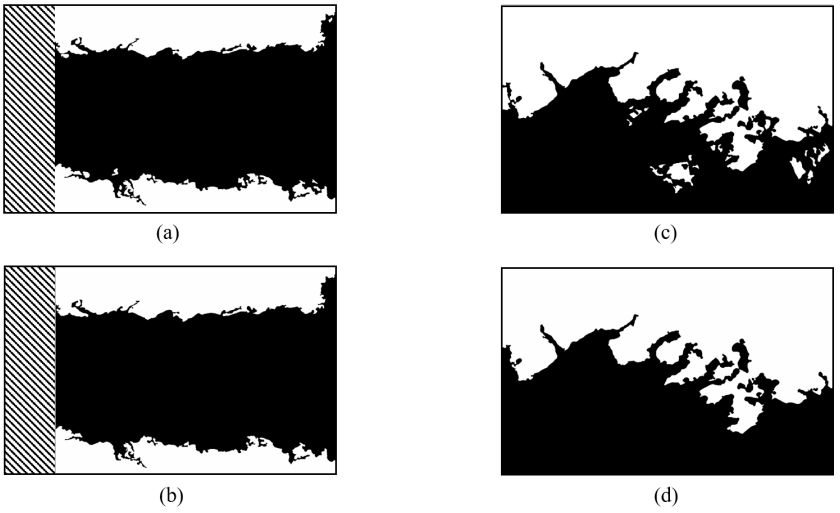

FIGURE 4.2: Segmented images from OC *RA* used to address the influence of hole elimination at different positions: (a) position $z = 5.11$ mm with holes; (b) position $z = 5.11$ mm without holes; (c) position $z = 22.4$ mm with holes; (d) position $z = 22.4$ mm without holes. All images correspond to a field of view of 8.64 mm x 5.40 mm.

The $e_2(d)_{,d}$ distributions are compared in Figure 4.3. The distributions are plotted in the [0 µm, 400 µm] scale range, where the textural information is found. Figure 4.3(a) considers the near-injector position, where very few holes are observed. The effect of the elimination of holes is therefore limited, as reported by the distributions. In Figure 4.3(b), however, which considers a more downstream zone where ligament-crossing holes are more frequent, the effect of eliminating these holes is more pronounced. Indeed, when holes are eliminated, some of the textural structures are also eliminated. This results in a loss of textural information. However, this loss seems to deal only with the number of structures visualized: the filling of holes in Figure 4.2(b) "erases" textural ligaments that have roughly the same size and deformation as the ligaments that remain. Furthermore, most of the structures erased by hole-filling are larger-scale structures that are not part of the textural atomization process. Therefore, there is possibly a reduction in the number of textural structures, but the size and the dispersion of the remaining structures whose $e_2(d)_{,d}$ is shown in Figure 4.3(b) are the same as before the filling of holes. Additionally, the effect of structures that are not part of the textural atomization process is reduced, and the resulting distributions are associated with textural ligaments only.

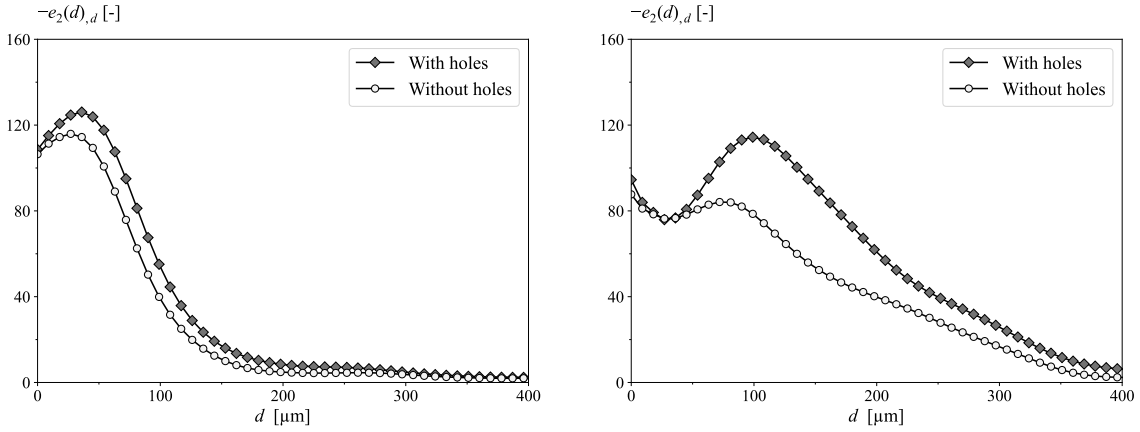

FIGURE 4.3: Influence of hole elimination on the $e_2(d)_{,d}$ distributions of instantaneous images from Figure 4.2 at: (a) position $z = 5.11$ mm; (b) position $z = 22.4$ mm.

Sub-pixel interpolation

As seen in Chapter 2, the spatial resolution of the image plays a major role in the quality of the measured scale distributions. Increasing the spatial resolution improves the measurements in two main ways: peaks in the distributions are better captured, and zone, in scale space, suffering from pixelization effects is reduced.

A 4x4 bilinear sub-pixel interpolation is applied to the normalized images, using the method presented in Chapter 2, to improve the spatial resolution by a factor 4. The resolution of the recorded backlighting images being $R = 4.5$ µm/pixel, the resulting interpolated image resolution is $R_{sub-pixel} = 1.125$ µm/pixel.

Figure 4.4 shows the effect of the sub-pixel interpolation on a given textural ligament extracted from the image shown in Figure 4.1. Figure 4.4(a) shows a close-up view of the ligament from the segmented image before the sub-pixel treatment, and Figure 4.4(b) shows the same ligament obtained after application of the sub-pixel treatment. The treatment produces a smoother interface due to the smaller size of the pixels after the interpolation step. Moreover, the treatment does not add or remove any relevant information on the resulting liquid systems. The effect of the sub-pixel treatment on the measured scale distributions is discussed later in Section 4.3.

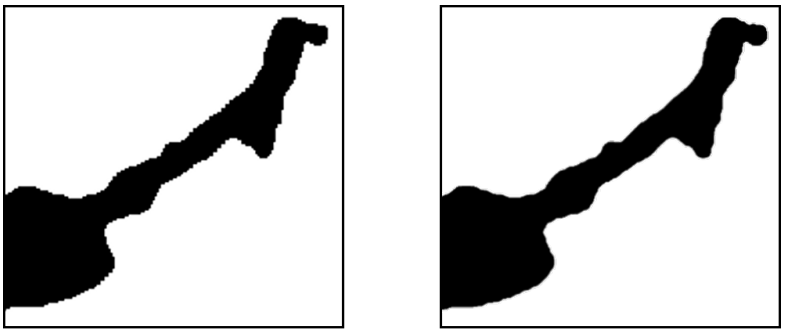

(a) (b)

FIGURE 4.4: Textural ligament (a) without and (b) with sub-pixel treatment.

4.2 Qualitative description the of textural atomization process

A series of segmented instantaneous images of the liquid oxygen jet interface are shown in Figure 4.5. The segmentation and other processing operations are done following the steps introduced previously in this chapter. Images are shown as a function of the distance z to the injector exit plane. Each row corresponds to one of the three tested operating conditions summarized in Table 3.1. The images shown are representative examples of the textural atomization process and are not correlated in time. Hachures are used to represent zones excluded from the analysis due to a lack of signal. This lack of signal in the images can be caused by insufficient lighting conditions (near the injector, for $z < 2$ mm approximately) or by the presence of deposits on the optical windows (more downstream, around $z = 15$ mm approximately for OCs *RA* and *RB* or around $z = 14$ mm approximately for OC *RC*). In addition, no images were recorded at some positions due to the limited time available during the experimental campaign. This is the case of the position labeled *Image 4* in Figure 4.5 ($z = 31.0$ mm) for OCs *RA* and *RC* and of the position labeled *Image 3* ($z = 22.4$ mm) for OC *RB*.

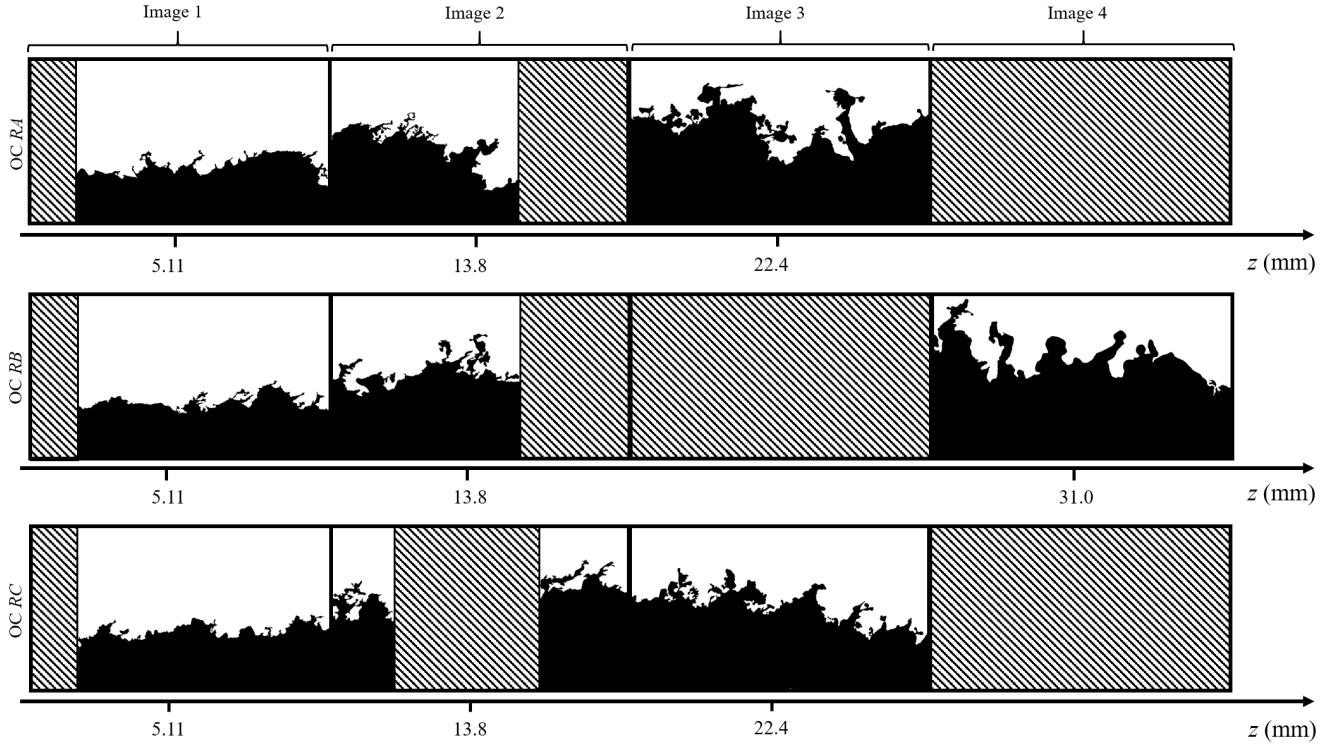

FIGURE 4.5: Snapshots of the liquid jet upper interface, after image processing from operating conditions (a) *RA*; (b) *RB*; (c) *RC*.

The observed liquid-gas interfaces show large- and small-scale deformation. The large-scale deformation can be seen as undulations with wavelengths of the order of the millimeter (as observed in the large-field view of Figure 3.6). These undulations are likely the result of the development of Kelvin-Helmholtz instabilities at the liquid surface, as reported by Marmottant and Villermaux [2004].

The small-scale deformations, on the other hand, are associated with the textural atomization process. The textural ligaments observed at the interface in Figure 4.5 are responsible for the production of droplets once they break up at the periphery of the liquid jet. Figure 4.5 also shows that the number, thickness, length, and shape of these ligaments evolve with the distance z to the injector. In general, as z increases, the ligaments tend to become more numerous, thicker, longer, and more deformed. This observation is in line with the one reported by Wu et al. [1992]. Similarly to the conclusion of their work, it can be inferred that the textural ligaments are initiated by turbulent fluctuations in the liquid. The development of the ligaments is a result of turbulent fluctuations in the liquid whose momentum is sufficient to overcome the surface tension forces at the interface. As the distance z increases, the characteristic size of the turbulent fluctuations capable of meeting this condition increases. This leads to larger and larger turbulent fluctuations breaking the surface tension, which in turn results in the production of thicker and thicker ligaments.

Another characteristic of the textural ligaments that can be observed in Figure 4.5 is that they are mainly oriented in the streamwise direction. This is particularly true near the injector (at distances up to around $z = 20$ mm). This orientation of the ligaments denotes the presence of aerodynamic effects. According to Wu and Faeth [1993], the primary breakup (here, the textural breakup) is affected by aerodynamics when the density ratio ρ_l/ρ_g is less than 500. This is the case for all three operating conditions considered here, as reported in Table 3.1. In the present case, the liquid jet is surrounded by a high-velocity gas flow that accentuates these effects and explains the orientation of the ligaments. According to Wu and Faeth [1993], near the injector, the aerodynamic effect is associated with the creation of low-pressure regions caused by the acceleration of the gas around the liquid ligaments. Further downstream, the aerodynamic effect is responsible for triggering a secondary breakup of the drops produced by the textural ligaments.

4.3 Scale resolution determination

Once the experimental backlighting images have been processed with the steps described previously, the scale distributions can be measured using the methodology presented in Chapter 2. Examples of time-averaged distributions measured on images of OC *RA* at $z = 13.8$ mm are presented in Figure 4.6. The number of images required to have statistically converged distributions is determined by plotting the average distribution as a function of the number of images on the set. Figure 4.6(a) compares the average distribution for sets of 5, 20, 50 and 100 images. It can be noted that 100 images are sufficient to reach a converged average. This was verified for all cases and positions considered and time-averaged measurements were therefore made on 100 images each time. Figure 4.6(b) compares the time-averaged $-e_2(d)_{,d}$ distribution measured on images with and without sub-pixel treatment. A 4x4 sub-pixel treatment is used. As seen in Chapter 2, the scale increment Δd of the scale distribution corresponds to 2 pixels. This results in a scale increment of $\Delta d = 2.25$ µm for the distribution with sub-pixel treatment, compared to the $\Delta d = 9$ µm of the case without sub-pixel treatment.

The distributions in Figure 4.6 are plotted in the [0 µm, 250 µm] scale range. This scale range is chosen to include all the textural scale information. The $-e_2(d)_{,d}$ distribution of a system homeomorphic to a 2D infinite cylinder, as is the case here, is expected to show a peak. Both distributions in Figure 4.6(a) show a peak at the same scale value. It is also expected that $-e_2(0)_{,d} = 0$. This, however, is not reproduced by the measured distributions. The reason is the presence of pixelization effects, as reported in Chapter 2, that provoke non-physical behavior near $d = 0$. The distribution with sub-pixel treatment, however, shows a peak that is close to satisfying this property. Indeed, the sub-pixel treatment reduces the range of the region affected by the pixelization bias, and that leads to a more accurate capture of the peak. Figure 4.6(a) also reports the

smallest scale at which the pixelization bias ceases (indicated by a vertical dashed line in Figure 4.6) and the peak of the distribution with sub-pixel treatment begins. This scale represents the scale resolution of the current procedure, i.e. the smallest structure-scale that the procedure can detect. According to Figure 4.6(a), the scale resolution is of approximately 16 µm in this case. The capture of the small-scale peak in the distribution with sub-pixel treatment in Figure 4.6(a) indicates that this resolution is sufficient to capture the main textural scales in the process.

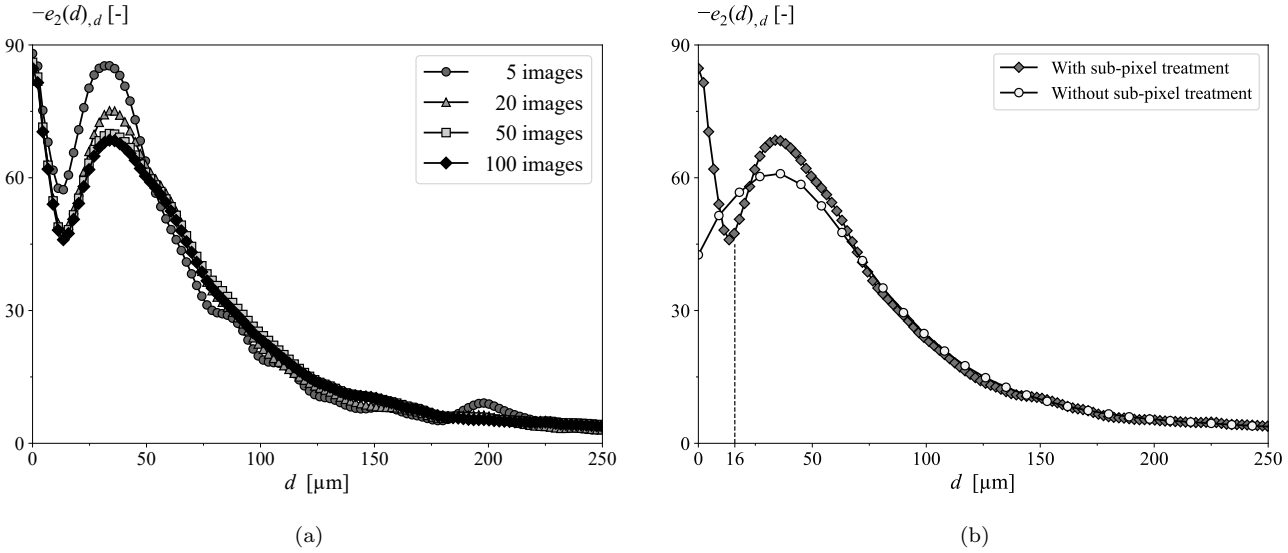

FIGURE 4.6: Time-averages $-e_2(d)_{,d}$ distributions of OC *RA* at position $z = 13.8$ mm. (a) Influence of the number of images on the average (measurements with sub-pixel treatment); (b) comparison of distributions measured on images with and without sub-pixel treatment.

4.4 Conclusion

In this chapter, the image processing applied on the experimental backlighting images from the MASCOTTE case was described. The resulting processed images were used to describe qualitatively the deformation of the liquid-gas interface, which includes both large- and small-scale features. The small-scale deformations are associated with ligaments produced by a textural atomization process that will be analyzed in Chapter 5. A measurement of a time-averaged scale distribution, introduced in Chapter 2, was then reported. This distribution was used to identify the scale resolution, i.e. the smallest scale the current technique can capture considering the image processing applied and the measurement method used. In the present case, the scale resolution is approximately 16 µm.

These results have shown that the scale resolution of the measurement technique is sufficient to measure the small-scale textural structures found at the interface. The

multi-scale description of these structures is presented in the next chapter, as well as an analysis leading to the estimation of the size distribution of the drops they may produce.

Chapter 5

Multi-scale analysis of textural atomization processes

This chapter presents the analysis of the textural atomization processes presented in Chapter 3: the experimental reactive process, named the MASCOTTE case, and the two non-reactive MARACA experimental and simulated cases. The visualization of these liquid systems shows the presence of textural ligaments which are responsible for the drop production. The analysis proposed here includes the measurement of scale distributions (as defined in Chapter 2) of the observed liquid systems to characterize their shape, size and dispersion. It then associates these measurements with equivalent systems of blobs. A model is then proposed to select the blob populations that are likely to produce drops as the atomization process unfolds, and to estimate their diameter distribution. The spatial evolution of the textural atomization processes is then discussed, and comparisons are made to assess the influence of the tested operating conditions on the process. The capacity of the DNS simulation to reproduce the production of textural ligaments is also discussed.

Contents

5.1 Reactive flow textural atomization

This section focuses on the multi-scale description of the textural ligaments observed at the liquid-gas interface of the reactive LOx-CH_4 configuration studied at the MASCOTTE test-bench and presented in Chapter 3. This multi-scale description allows to characterize the size, number, and deformation of the observed textural ligaments by measuring their scale distributions. The aim of this description is to provide information about the drops these textural ligaments may produce, based on the characterization of the shape of the ligaments.

A ligament undergoing breakup shows both contracted sections and swollen sections. The swollen sections of a ligament are usually a signature of a droplet being produced. Figure 5.1 shows a ligament where contracted and swollen sections can be observed. Some of the swollen sections are represented schematically by circular blobs in the figure. The analysis presented in this chapter aims at estimating the size distribution of these circular blobs, which is indicative of the diameter distribution of the large drops produced by the textural ligaments.

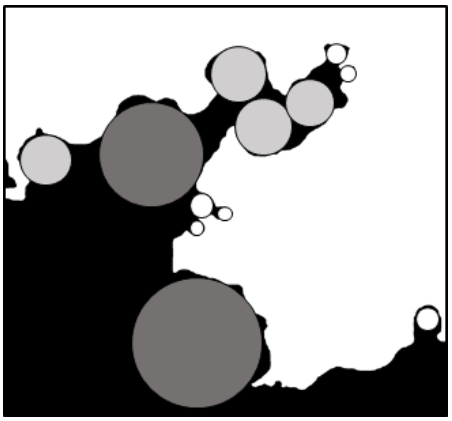

FIGURE 5.1: Identification of circular blobs on a textural ligament.

5.1.1 Measured scale distributions

The textural blob size distributions are obtained by analyzing the scale distributions ($e_2(d)$ and $e_2(d)_{,d}$) of the textural ligaments at the LOx jet interface seen in Figure 5.2. To study the spatial evolution of the textural atomization process, the images are divided into Regions of Interest (ROI) of approximately 2 mm in length. The width of the ROIs is not constant, and varies between 1.74 mm and 2.67 mm. Each of the considered ROI is represented in Figure 5.2 by a gray rectangle at the corresponding position. The z

position of the center of each ROI is also indicated in the figure. The scale distributions are measured at each of the ROI and are divided by the width w_{ROI} of the ROI to allow direct comparisons between distributions from ROIs with different widths. As explained in Chapter 4, the regions covered with hachures in Figure 5.2 are excluded from the analysis because of a lack of signal due to either insufficient lighting or to the presence of deposits on the optical window, or because images were not recorded.

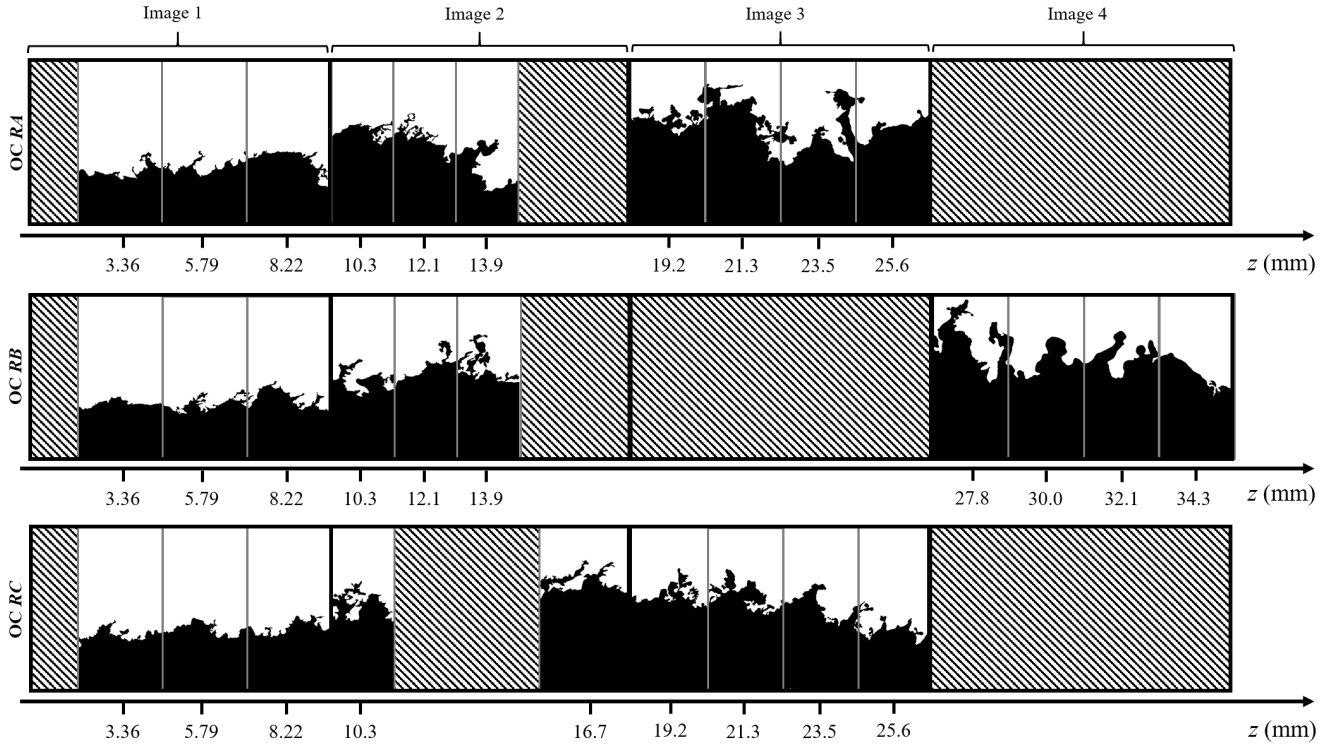

FIGURE 5.2: Snapshots of the liquid jet upper interface, after image processing, divided into ROIs as a function of the distance z to the injector. From top to bottom: Operating conditions *RA*; *RB*; *RC*.

Figures 5.3(a)-(c) plot the time-averaged normalized $e_2(d)$ distributions at all ROI positions from operating condtions *RA*, *RB* and *RC* respectively (see Table 3.1 for a summary of the operating conditions). The average is calculated using 100 images decorrelated in time. Distributions are plotted in the [16 µm, 350 µm] scale range to include all textural structures that can be spatially resolved by the technique. As introduced in Chapter 2, the $e_2(d)$ distributions represent half of the circumference of the eroded system at scale d. Figure 5.3 reports distributions that are monotonically decreasing functions of d. This decrease contains information on the size and deformation of the textutal ligaments at the interface: the thinner the ligaments, the smaller the scales at which the distributions decay. Moreover, the distributions all reach a constant value near the upper limit of the plotted scale range. The scale at which a distribution reaches a constant value corresponds to the largest scale of the textural ligaments at that position.

The evolution of the distributions with z shows that when z increases, the scale at which the distributions reach a constant value is larger. This indicates an increase of the size of the textural ligaments as the distance from the injector increases. This is consistent with the qualitative observations made in Chapter 4. Furthermore, the height of the distributions tend to increase with z from the first positions up to an intermediate position, at around $z = 20$ mm. After these positions, the distribution decrease in height until the last measured position. The $e_2(d)$ distributions contain information on the volume of the textural liquid ligaments. An increase in $e_2(d)$ at a given scale is therefore associated with an increase in the volume carried by the ligaments of that size. We can deduce from this that the volume of liquid involved in the textural atomoization process initially increases, reaches a maximum and then decreases as the distance z increases.

The behavior of the $e_2(d)$ distributions described above is observed for all operating conditions. It is interesting to note that, in Figure 5.3(b) corresponding to measurements of OC *RB*, at positions $z = 27.8$ mm and beyond, the decay of the distributions is much slower in the small-scale zone compared to positions more upstream. In addition, the distributions only reach a constant value at the very end of the plotted scale range. These observations are indicative of a lower amount of small-scale structures and of the presence of larger structures at those distances.

The derivatives $-e_2(d)_{,d}$ of the scale distributions $e_2(d)$ are plotted in Figure 5.4 in the [16 µm, 350 µm] scale range. The distributions show bell shapes that are proportional to the number-based diameter distribution $f_{0c}(D)$ of the equivalent ensemble of cylinders, as in Equation 2.20, which is reminded here:

$$e_2^c(d)_{,d} = -N_c L_c f_{0c}(D)_{|D=d} \tag{2.20}$$

The textural liquid structures, whose $-e_2(d)_{,d}$ distributions are plotted in Figure 5.4, can therefore be seen as an ensemble of cylinders whose population depends on the distance z from the injector. Moreover, we impose $L_c = 1$ µm in Equation 2.20. Doing this, the proportionality coefficient is equal to the number N_c of cylinders of length $L_c = 1$ µm that contribute to this distribution. The measured $-e_2(d)_{,d}$ distributions therefore inform on the number, size and dispersion of cylinders in the equivalent system.

Near the injector ($z = 3.36$ mm), the $-e_2(d)_{,d}$ distributions in Figures 5.4(a)-(c) show a maximum near the bottom limit of the scale range, at approximately $d = 25$ µm. The value of this maximum is the lowest, compared to other positions. The width of the distributions at this position is also small. As the distance z increases, the $-e_2(d)_{,d}$ distributions evolve and report maxima at larger and larger scales. The value of the maximum also evolves with z: it increases until a certain z position, and then decrease

until the last measured positions. Lastly, the width of the distributions increases with the increase of z.

It is interesting to note that, for OC *RB*, where measurements are made on ROIs that reach farther distances than the other cases, the measured distributions are somewhat different. At these positions (z = 27.8 mm, z = 30.0 mm, z = 32.1 mm, and z = 34.3 mm), the distributions are very wide and nearly flat between d = 50 µm and d = 150 µm approximately. This behavior approaches the characteristic shape of the $-e_2(d)_{,d}$ distribution of an ensemble of spheres (see Figure 2.11 for example). The liquid system can therefore be seen as an ensemble of spheres of diameters larger then 150 µm that are connected to each other. In this case, very little textural deformation is observed. This last observation is in agreement with the liquid system observed at those positions in Figure 5.2 and indicates that the textural atomization process stops at an earlier position z.

For all operating conditions, the evolution of the measured $-e_2(d)_{,d}$ distributions characterize the textural ligaments as a function of the distance z. In general, the distributions indicate that near the injector the textural ligaments are short and/or few in number, that they are thin and that their deformation is limited. As the distance z increases, the distributions indicate that the ligaments become thicker and more deformed. Their number and/or length seems to increase at first, reach a maximum, and then decrease until no more textural deformation is observed.

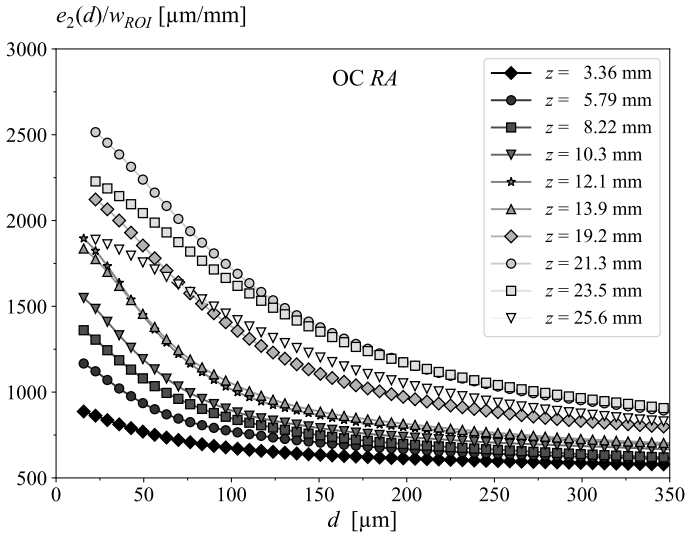

(a)

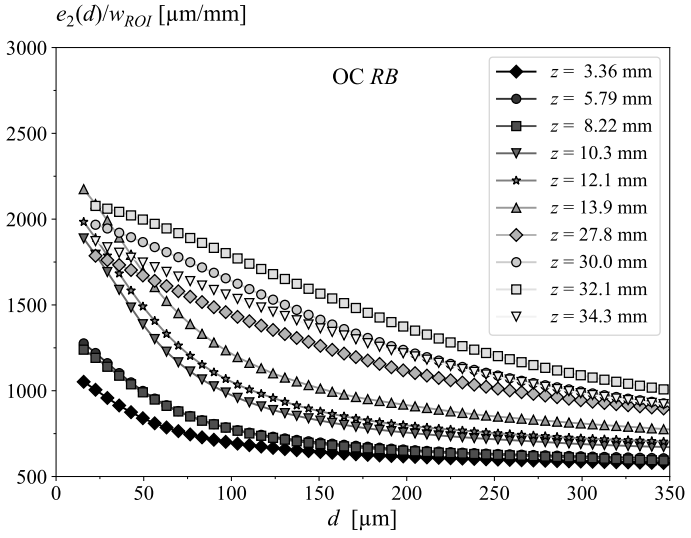

(b)

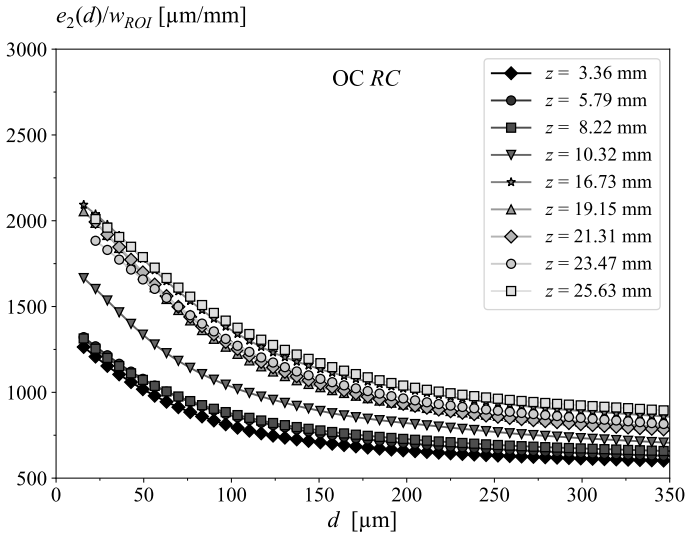

(c)

FIGURE 5.3: Distributions $e_2(d)/w_{ROI}$ at each z position for operating conditions (a)RA, (b)RB, and (c)RC. (Curves show every third point).

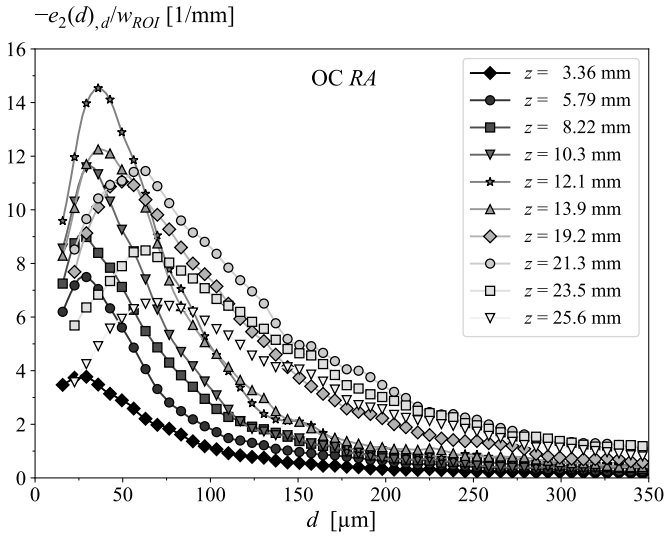

(a)

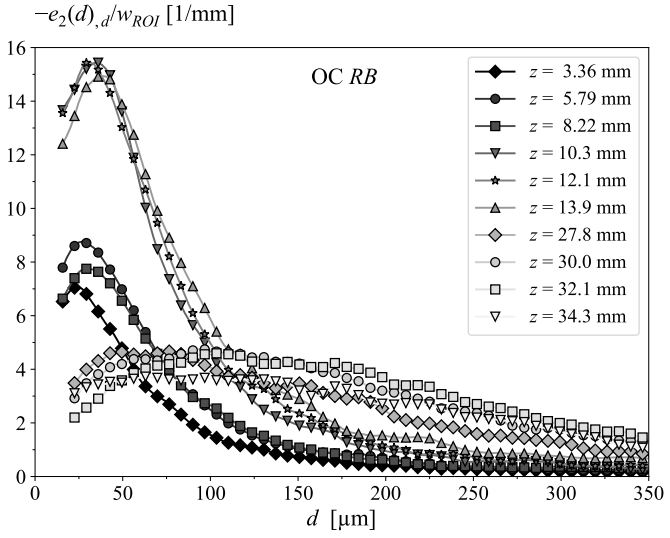

(b)

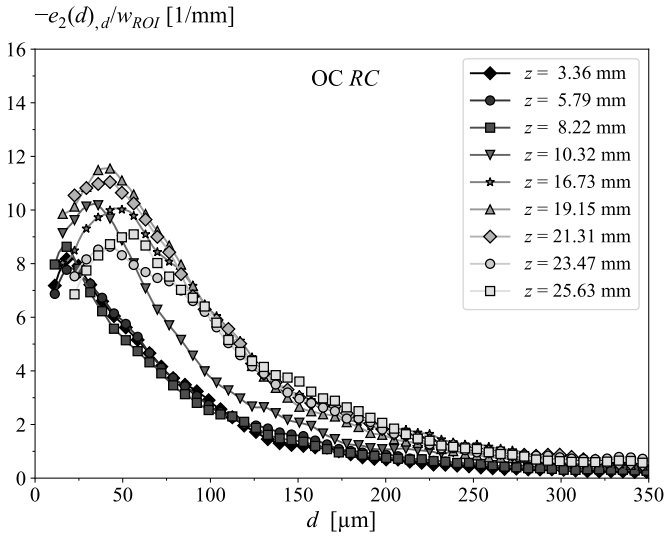

(c)

FIGURE 5.4: Distributions $-e_2(d)_{,d}/w_{ROI}$ at each z position for operating conditions (a)RA, (b)RB, and (c)RC. (Curves show every third point).

5.1.2 Identification of blob populations

As mentionned previsouly, the textural ligaments are composed of contracted sections and swollen sections. The right-hand part of the $-e_2(d)_{,d}$ distributions (i.e. for scales greater than the peak scale d_p) contains information on the swollen sections of the ligaments, represented schematically in Figure 5.1. It is therefore in this part of the distribution that the information concerning the blob size distribution can be found. As done in Chapter 2, the blob diameter distribution can be represented by a 3pGG distribution. Since the blobs are assumed circular, they can be seen as an ensemble of spheres. In Chapter 2, we have seen that an ensemble of spheres can be represented by an equivalent system of cylinders whose scale distribution can be expressed using a 3pGG distribution with $\alpha = 1$. The measured scale distributions can therefore be expressed in terms of their equivalent system of cylinders as in Equation 2.31, reminded below:

$$e_2(d)_{,d} = -N_c L_c \frac{q}{\Gamma\left(\frac{1}{q}\right)} \left(\frac{1}{q}\right)^{1/q} \frac{1}{D_c} \exp\left(-\frac{1}{q}\left(\frac{d}{D_c}\right)^q\right), \tag{2.31}$$

recalling that N_c and D_c correspond to the number and mean diameter D_{q0} of cylinders in the equivalent system, respectively, while q is a parameter of the 3pGG distribution. This equation can be rewritten as:

$$e_2(d)_{,d} = e_2(0)_{,d} \exp\left(-\frac{1}{q}\left(\frac{d}{D_c}\right)^q\right) \tag{5.1}$$

Taking the logarithm of this expression twice, it becomes:

$$\ln\left(\left|\ln\left(\frac{e_2(d)_{,d}}{e_2(0)_{,d}}\right)\right|\right) = q\ln(d) - q\ln(D_c) - \ln(q) \tag{5.2}$$

Equation 5.2 expresses a linear evolution, in a log-log frame, of the logarithm of the distribution $e_2(d)_{,d}$ with the scale d. In the present case, we wish to analyse the right-hand side of the measured $e_2(d)_{,d}$ distributions from Figure 5.4 by associating it to an equivalent ensemble of blobs. Replacing $e_2(0)_{,d}$ by $e_2(d_p)_{,d}$ (i.e. the maximum value of the distribution, located at the peak scale d_p) allows to apply the model from Equation 5.2 and evaluate its relevance to the measurements.

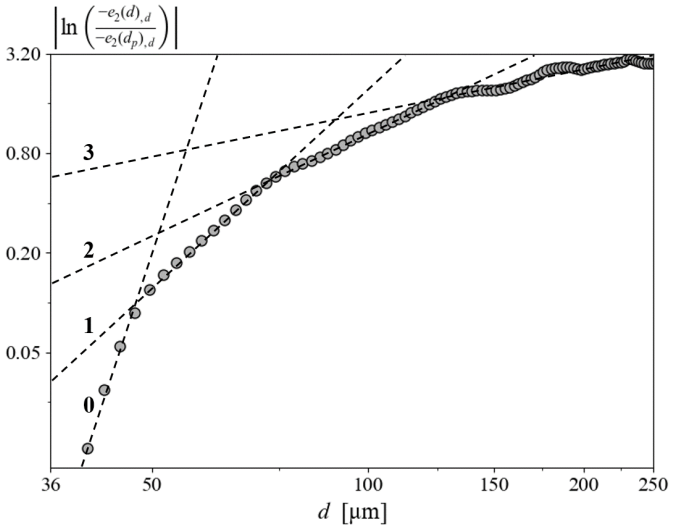

FIGURE 5.5: $\ln\left(\left|\ln\left(\frac{e_2(d)_{,d}}{e_2(d_p)_{,d}}\right)\right|\right) = f(\ln(d))$ (OC *RA* at $z = 12.1$ mm).

As an example, we consider the $e_2(d)_{,d}$ distribution from OC *RA* at position $z = 12.1$ mm. Figure 5.5 plots the left-hand side term of Equation 5.2 applied to the measured distribution as a function of $\ln(d)$. The figure reports four regions where the curve shows a linear evolution. The presence of linear regions indicates that the model from Equation 5.2 is in agreement with the measurements. Each of the four linear regions represents a family of blobs. Region 0 in Figure 5.5 is defined by only a few points in the current case, and its presence is not reported by all of the measured distributions. In addition, an examination of the backlighting images reveals only very few blobs of sizes corresponding to the scales covered by this region. Region 1 relates to a family of small blobs usually found at the interface of ligaments, such as the ones shown in white in Figure 5.1. Region 2 corresponds to a family of blobs formed on the body of the ligaments, as the ones shown in light gray in Figure 5.1. Region 3 corresponds to blobs formed at the base of the ligaments, as shown in dark gray in Figure 5.1.

Considering the four families of blobs reported by Figure 5.5, it is blobs from the families associated to regions 1 and 2 (and part of region 3) that are most likely to produce drops of similar sizes when the ligament undergoes breakup. A model is therefore proposed to identify and characterize two blob populations from two consecutive regions (in scale space). The proposed model introduces two components to the $e_2(d)_{,d}$ distribution:

$$-e_2(d)_{,d} = N_{ci} f_{0ci}(d) + N_{c(i+1)} f_{0c(i+1)}(d) \tag{5.3}$$

The model can refers to different regions (or blob families), depending on the value of i. Taking $i = 1$ or 2 refers to the analysis of regions 1 and 2 or 2 and 3, respectively. The distribution $f_{0ci}(d)$ from Equation 5.3 is given by (see Equation 2.31):

$$f_{0ci}(d) = \frac{q_i}{\Gamma\left(\frac{1}{q_i}\right)} \left(\frac{1}{q_i}\right)^{1/q_i} \frac{1}{D_{ci}} \exp\left(-\frac{1}{q_i}\left(\frac{d}{D_{ci}}\right)^{q_i}\right) \tag{5.4}$$

Six parameters must be determined to fit the measured $-e_2(d)_{,d}$ distribution with the model from Equation 5.3: N_{ci}, q_i and D_{ci} for the first component and $N_{c(i+1)}$, $q_{(i+1)}$ and $D_{c(i+1)}$ for the second. Introducing in the model a value for $e_2(0)_{,d}$ in Equation 5.1 allows to express one of the parameters as a function of the five others. This reduces the total number of parameters that must be determined to five. The model is applied for a given scale range $[d_1, d_2]$ covering the two regions of interest. The limits d_1 and d_2 are determined on curves such as the one in Figure 5.5. The $e_2(0)_{,d}$ value is taken as equal to the experimental value of $e_2(d_1 - \Delta d)_{,d}$, i.e. the value of the distribution at the point preceding d_1. As seen in Chapter 4 (Section 4.3), the scale increment Δd corresponds to two image pixels, which in the current case is equivalent to 2.25 µm. The parameters ensuring the best fit with the measurements are then determined using the Python *scipy.optimize.minimize* routine.

Once the six parameters of the model are determined, the blob diameter distribution of each component, $f_{0si}(D)$ and $f_{0s(i+1)}(D)$ can also be determined, using Equation 2.35. Then, the mean diameters D_{si} and $D_{s(i+1)}$ of the two blob families can be determined with Equation 2.37, and the blob numbers N_{si} and $N_{s(i+1)}$ can be determined with Equation 2.33. It is important to note that the blob numbers N_{si} and $N_{s(i+1)}$ do not actually represent the number of blobs since they depend on the value of L_c which was arbitrarily taken equal to 1 µm in the current model. However, N_{si} and $N_{s(i+1)}$ are proportional to the real number of blobs in the same way for all cases considered here, which allows to perform comparisons.

Let us consider again the example distribution from OC *RA* at $z = 12.1$ mm, whose blob population are identified in Figure 5.5. The model is applied to regions 1 and 2 (taking $i = 1$) and then to regions 2 and 3 (taking $i = 2$). The result of these applications are shown in Figure 5.6.

Figures 5.6(a) and 5.6(b) report the results from regions 1 and 2. In each plot, the analyzed scale range $[d_1, d_2]$ is delimited by vertical dashed lines. Figure 5.6(a) indicates that the model yields a very acceptable fit of the $e_2(d)_{,d}$ distribution in the analyzed scale interval. The resulting number-weighed diameter distributions in Figure 5.6(b) show that the blob populations from regions 1 and 2 are very distinct. The peak diameters are equal to 70 µm and 100 µm for populations 1 and 2, respectively. The distribution of blobs from population 1 is far more narrow than that of blobs from population 2. The surface area delimited by each number-weighed blob diameter distribution is equal to the number of blobs of each population. The sum $N_{si} + N_{s(i+1)}$ corresponds to the total blob number. In the case shown in Figure 5.6(b), population 2 contains a larger proportion of blobs, totalling 73% of the total blob number.

Figures 5.6(c) and 5.6(d) report the results of the application of the model to regions 2 and 3. Figure 5.6(c) reports that, just as in the previous case, the model provides a good fit of the measured distribution in the analyzed scale interval $[d_1, d_2]$. Regions 2 and 3 show distinctive blob populations and the global distribution is bi-modal. The two distributions overlap less than in the previous application. The peak diameter of the populations from regions 1 and 2 are equal to 100 µm and 190 µm, respectively, and the distribution of population 2 is wider than that of population 3. Population 2 contains the greater number of blobs, totalling 74% of the total blob number.

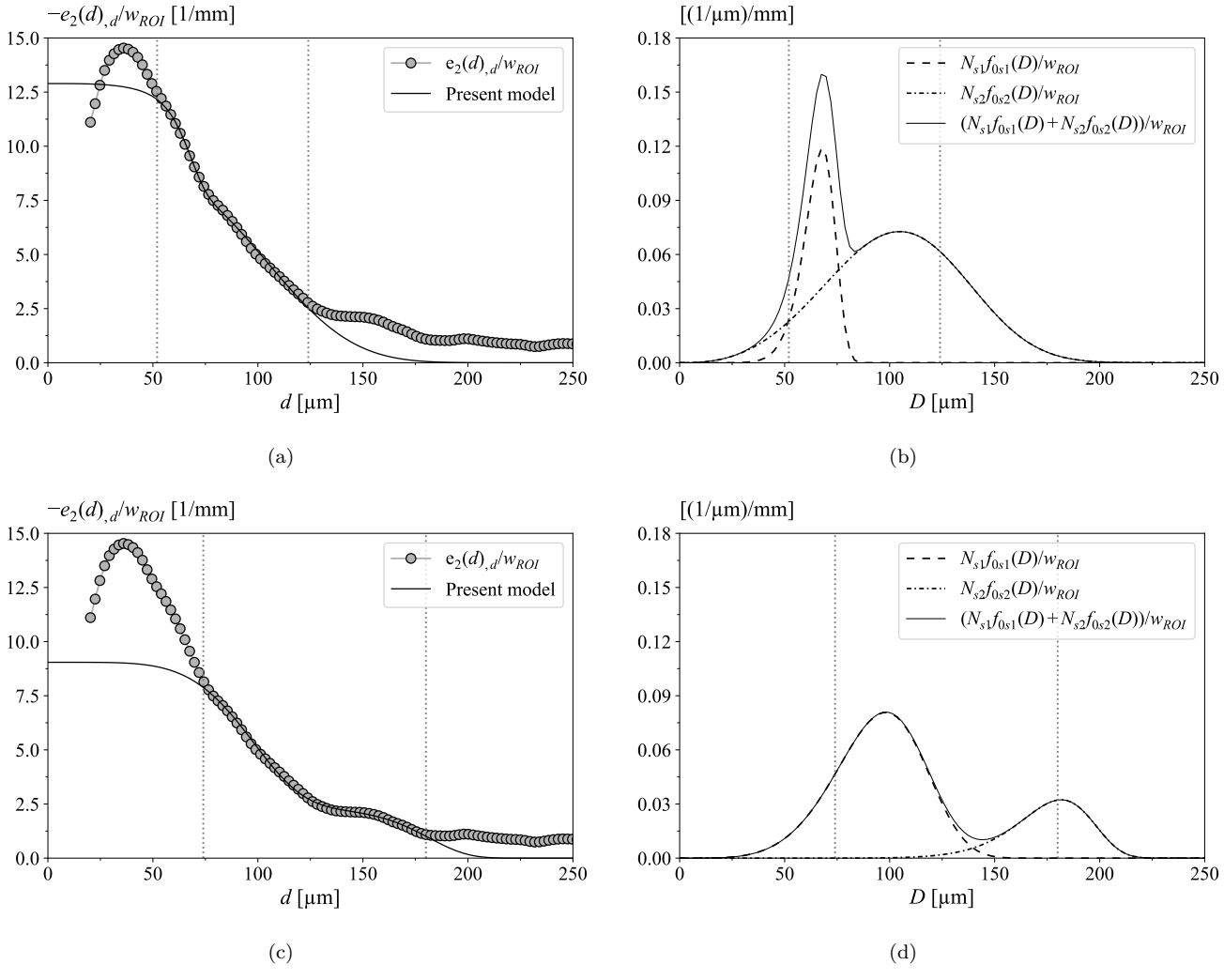

FIGURE 5.6: Fit of the measured $e_2(d)_{,d}$ distribution from OC *RA* at $z = 12.1$ mm with the proposed model (graphs on the left) and the corresponding number-weighted blob diameter distributions (graphs on the right).
(a) and (b): populations 1 and 2, scale range [52 µm, 124 µm];
(c) and (d): populations 2 and 3, scale range [74 µm, 180 µm].

The two applications of the model reported in Figure 5.6 capture the region 2 blob population. The two corresponding blob diameter distributions are quite similar, but differ in width: the one in Figure 5.6(b) is wider, extending to diameters near the peak

diameter of region 3, i.e. 190 µm. This difference is due to the fact that the model extends the distribution beyond d_2 insofar as $e_2(d_2)_{,d}$ is never zero. Thus, the diameter distribution of blobs in region 2 obtained by analyzing regions 1 and 2 includes some small blobs from region 3. Figure 5.1 suggests that some small region 3 blobs may also produce drops once the ligament breaks up. Therefore, the analysis considering regions 1 and 2 is considered to report the best estimation of the diameter distribution of the blobs that will become drops.

5.1.3 Preliminary validation of the two-population ligament blob model

The development of the proposed two-population blob model is based on the following key hypotheses:

1. The blobs from Regions 1 and 2 are responsible for generating the main primary droplets.

2. The size of these blobs correlates with the size of the resulting droplets.

To assess the validity of these hypotheses—and, by extension, the ability of the proposed method to determine blob diameter distributions that can be used to accurately model the textural drop production process—the local ligament blob diameter distributions are compared to the diameter distributions of droplets produced within the same spatial zone and time interval. This comparison is established using the set of 100 backlighting images centered at position $z = 12.1$ mm. The measurement of the droplet diameter distribution is performed using a similar methodology as the one used to measure the ligament blob diameter distributions from Figures 5.6(a) and 5.6(b). First, the detached liquid structures/droplets removed from the backlighting images during the image processing described in Chapter 4 are retrieved and isolated. Then, these liquid structures are filtered in order to remove the very small droplets (which are not directly produced by blobs from the selected regions) as well as structures whose shape is far from a sphere. This is done by applying a surface-based filter, that eliminates droplets of equivalent diameter inferior to 40 µm, and a circularity-based filter that eliminates structures of circularity below 0.5 (here, circularity is defined as $C = 4piS/L^2$, where S and L are the surface area and the perimeter of the object, respectively). An example is shown in Figure 5.7 where an instantaneous backlighting image is shown next to the corresponding isolated droplets. Next, the time-averaged $-e_2(d)_{,d}$ distribution of the droplets is measured on 100 images such as the example in Figure 5.7. Figure 5.8(a) shows the measured time-averaged distribution. The Finally, the two-population blob model is applied to fit the time-averaged $-e_2(d)_{,d}$ over the entire scale range of the distribution (i.e. from 30 µm to 150 µm). The modeled $-e_2(d)_{,d}$ distribution is represented by the black curve in Figure 5.8(a). The corresponding blob diameter distribution of the droplets are shown in Figure 5.8(b).

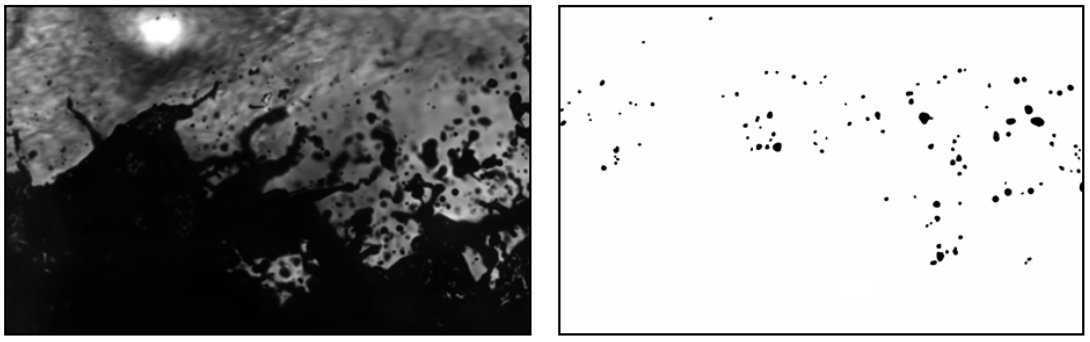

FIGURE 5.7: Instantaneous image at position $z = 12.1$ mm (left) and the corresponsing isolated and filtered droplets (right).

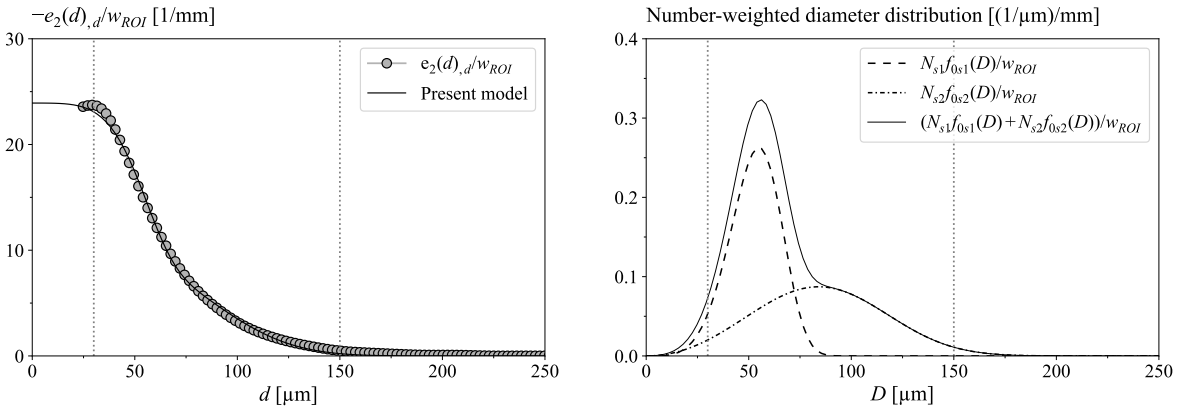

(a) (b)

FIGURE 5.8: Time-averaged measurement and the associated blob model of the isolated droplets at $z = 12.1$ mm: (a) fit of the measured $e_2(d)_{,d}$ distribution of the droplet system with the proposed blob model; (b) the corresponding number-weighted blob diameter distributions.

Comparing the diameter distribution of the droplets, reported in Figure 5.8(b), with that of the corresponding ligament blobs from Figure 5.6(b), very similar results are found. Both distributions share a similar bi-modal shape with the distributions of each population centered on similar scales and covering similar scale ranges. Slight differences are observed in the height of the distribution (higher in the case of the droplets, indicating a higher number of droplets than ligament blobs) and in the width of each population. The difference in height can be explained by the inclusion of droplets that were produced in more upstream positions in addition to those produced by the ligaments observed in the current position. Moreover, the difference in width can be explained by the inclusion of some of the smaller, satellite droplets produced by the contracted sections of the ligaments and/or of droplets resulting from secondary atomization of larger structures, which are not included in the ligament-blob distribution in Figure 5.6(b).

Overall, this preliminary comparison is satisfactory and shows that the local ligament blob diameter distributions obtained using the proposed model are representative of the local droplet diameter distribution. This indicates that the ligament blob diameter distributions obtained can be used to quantify the local textural drop production and to develop models of the process.

5.1.4 Spatial evolution of blob diameter distributions

The analysis of regions 1 and 2, presented above for the measured scale distribution from OC *RA* at $z = 12.1$ mm is now performed at each z position of that OC. The number-weighted diameter distributions of the blobs of each population, as well as their sum, are plotted in Figure 5.9. On each graph, the scale interval $[d_1, d_2]$ consideredin the analysis is indicated by vertical dashed lines. The resulting blob diameter distibution are divided by the ROI width w_{ROI} to allow comparisons of curves from one position to another. For downstream positions $z = 23.5$ mm and $z = 25.6$ mm no region 1 blobs were found. Therefore, for these positions, only region 2 was analyzed, using a reduced, one-component model. The scale intervals $[d_1, d_2]$ for these two mono-modal applications were defined on the basis of the evolution of $d_1(z)$ and $d_2(z)$, built from the preceding positions. Figure 5.10 plots the evolution of the d_1 and d_2 scale limits with the position z. A linear fit of values between $z = 3.36$ mm and $z = 21.31$ mm is proposed and used to determine the scale interval limits of the two furthest positions.

The diameter distribution of blobs of population 1 varies little with the position. Indeed, the peak diameter of the distribution remains nearly the same. On the other hand, the number of blobs in this population varies significantly. It increases from $z = 3.36$ mm to $z = 12.1$ mm and then collapses between $z = 12.1$ mm and $z = 21.3$ mm. Based on the hypothesis that these blobs become drops, it is therefore between 10 and 13 mm from the injector that the production of small droplets is most intense. As mentioned above, this population is no longer observed at the two farthest positions.

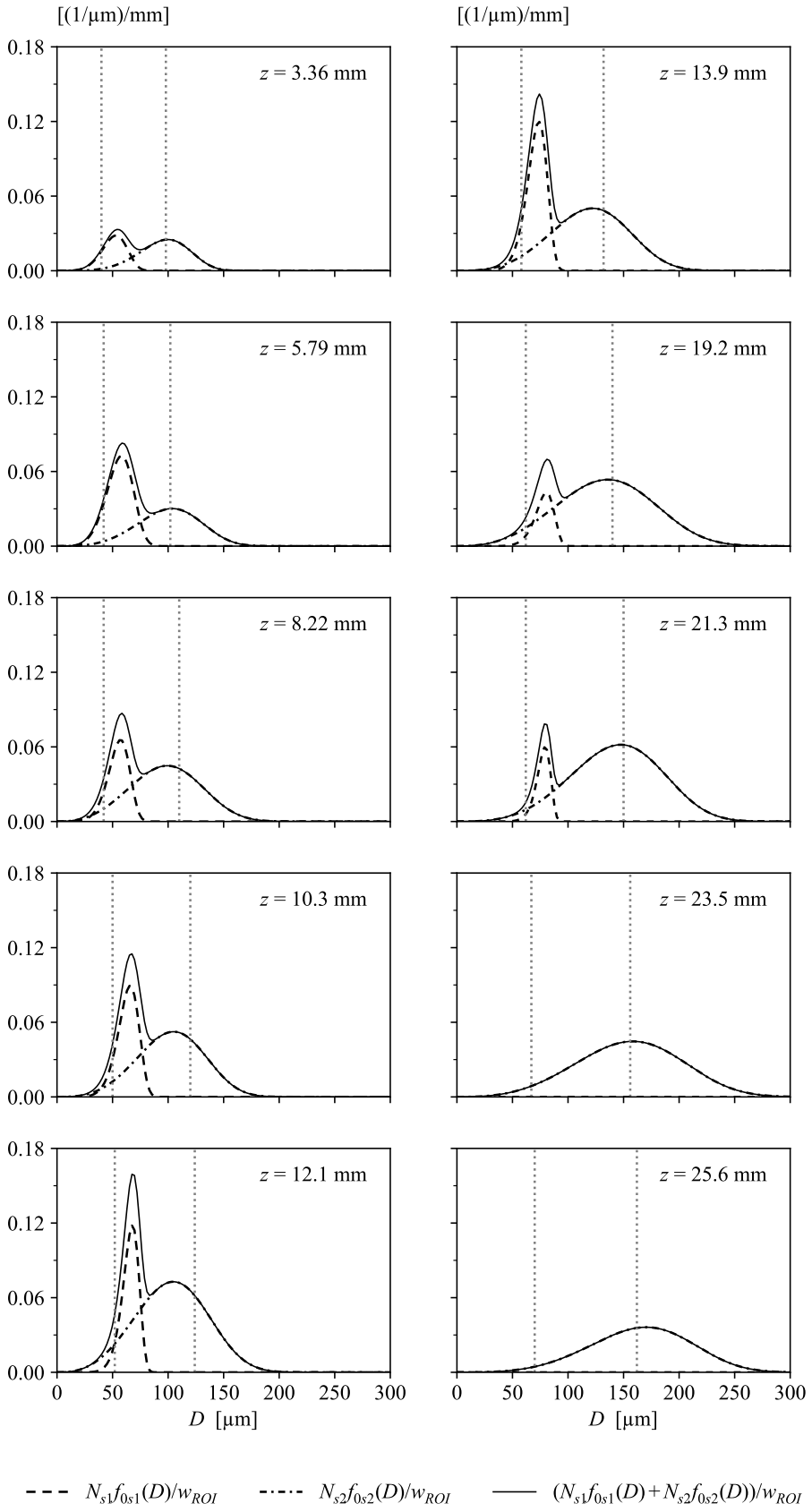

FIGURE 5.9: Number-weighted blob diameter distribution of populations 1 and 2, and their sum, for each z position of OC *RA*.

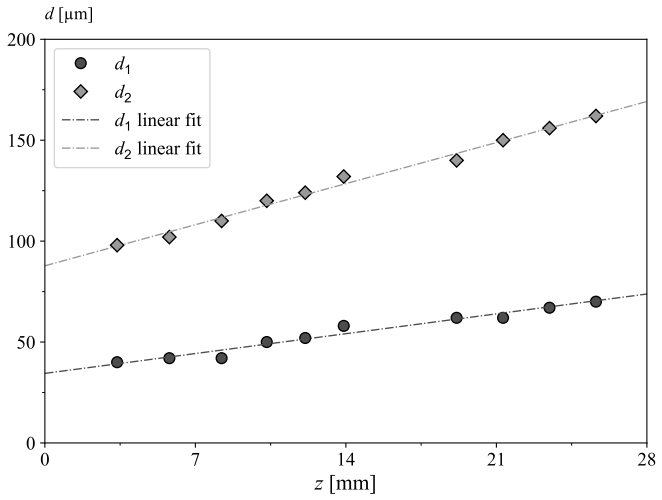

FIGURE 5.10: Scale interval limits d_1 and d_2 at each z position (OC *RA*).

The diameter distribution of blobs from population 2 varies continuously with the position. The peak diameter and width of the distribution both increase. Furthermore, the distribution first swells from $z = 3.36$ mm to $z = 21.3$ mm and then deflates from $z = 21.3$ mm to $z = 25.6$ mm. Thus, the drops produced by blobs from this population continuously increase in diameter, while their number first increases and then decreases as we move away from the injector. The observed increase in diameter of population 2 is identical to that of drops resulting from the primary atomization process described by Wu and Faeth [1993]. Therefore, the drops associated to this blob diameter distribution seem to be those resulting directly from the turbulence of the liquid flow.

The sum of the diameter distributions from the two components shown in Figure 5.9 is representative of the diameter distribution of drops issued from the textural atomization process. The present analysis shows that these drops combine two mechanisms of production near the injector that result in a bi-modal diameter distribution. Finally, further downstream, the textural atomization process fades away, as shown in the case considered here by a marked decrease of the number of blobs in the distribution from position $z = 21.3$ mm onwards.

The blob diameter distributions reported in Figure 5.9 are, as expressed by Equation 2.38, 3pGG distributions. The study of the parameters of the distributions and of their spatial evolution assesses the possibility of proposing a model for the local drop diameter distribution issuing from the textural atomization process. The evolution of these parameters with the position z are plotted in Figure 5.11.

Parameters q_1, q_2, D_{s1} and D_{s2} all report linear spatial evolutions, with D_{s2} reporting a change of slope at $z = 12.1$ mm. The increase of q_1 denotes a distribution with an increasingly smaller dispersion (the dispersion being a dimensionless distribution width). On the other hand, the almost constant q_2 denotes a distribution with a rather constant

dispersion. The linear evolution of D_{s2} is almost identical to the one from D_{s1} until $z = 12.1$ mm, after which position the slope of D_{s2} increases. Finally, the spatial evolutions of the numbers N_{s1}/w_{ROI} and N_{s2}/w_{ROI} are not monotonous. This is the case since these parameters reflect the presence and intensity of the textural atomization process. The spatial evolution of these two parameters indicate that the production of drops from the textural atomization process is the most intense at approximately 16 mm from the injector for the small droplets and at approximately 21 mm for the main drops. Furthermore, the decrease of N_{s1} coincides with the change of slope in the evolution of the mean diameter D_{s2}. The spatial evolutions of these parameters reported in Figure 5.11 suggest the possibility of designing a model to predict the drop production due to textural atomization from the blob populations identified using the multi-scale description of the liquid-gas interface considered in this thesis.

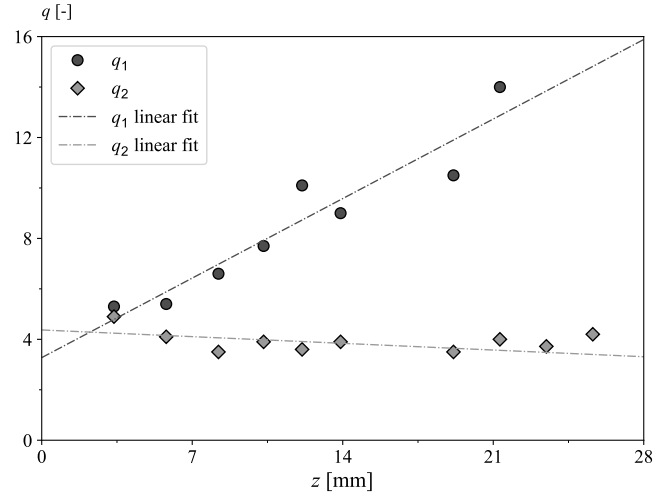

(a)

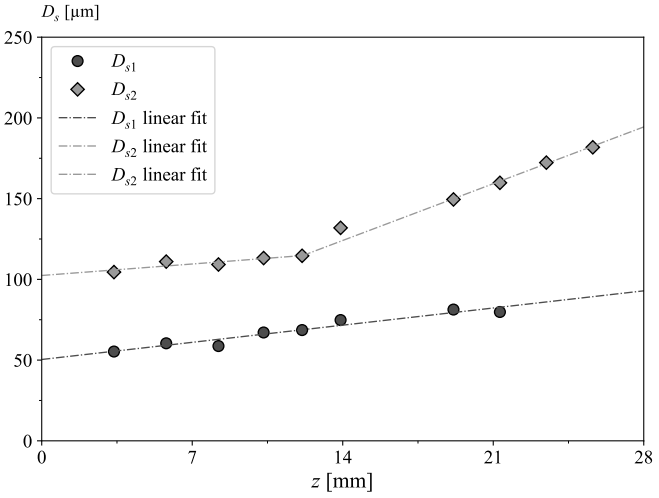

(b)

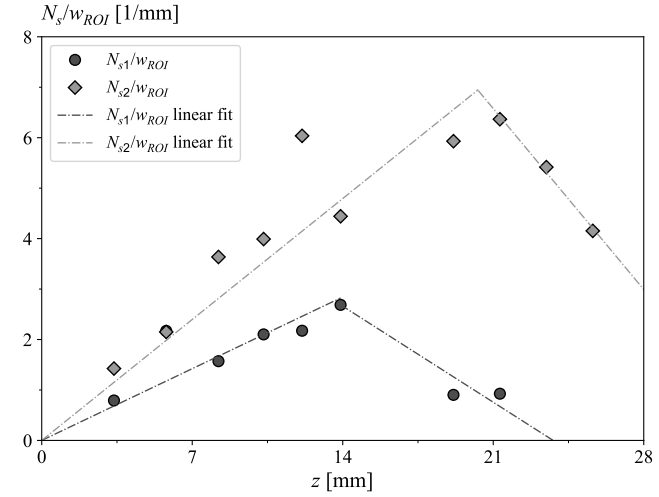

(c)

FIGURE 5.11: Spatial evolution of the parameters of the blob diameter distributions: (a) parameter q, (b) parameter D_s and (c) parameter N_s.

5.1.5 Influence of operating condition on blob diameter distributions

The liquid-gas interface observed in Figure 5.2 shows the presence of textural ligaments with similar characteristics for all of the operating conditions represented. This is confirmed by the $e_2(d)$ and $e_2(d)_{,d}$ measurements reported in Figures 5.3 and 5.4 respectively. The distributions show similar shapes and similar dependencies on the position z. Similar populations are also identified using the model from Figure 5.5 in all three cases. The similarities reported are due to the operating conditions representing the same global regime, with a small range of variation of the dimensionless parameters. Given the similarity between the three operating conditions, we propose to use the same analysis performed in the previous section for images of the OC *RA* to characterize the textural atomization process of the two other tested operating conditions from Table 3.1.

Thus, the proposed two-blob-population model, which yielded the number-weighted blob diameter distributions reported in Figure 5.9 for OC *RA*, is now applied to measurements from OCs *RB* and *RC* (from Figures 5.4(b) and 5.4(c)). The resulting blob diameter distributions can be found in Appendix A. The parameters of the resulting blob diameter distributions are plotted in Figures 5.12, 5.13 and 5.14 as a function of the distance z to the injector for the three operating conditions.

For all operating conditions, two blob populations are observed at distances close to the injector. The population 1 evolves in diameter, number and dispersion until, once a given z position is reached, it is no longer observed. From this position on, only population 2 is observed. Figures 5.12(a), 5.13(a) and 5.14(a) report the parameters associated to the blob population 1. The graphs report similar spatial evolutions of most of the distribution parameters between the different operating conditions. The parameter q_1 represents the dispersion of the distribution (or a relative width). It increases significantly with z for OC *RA* but remains rather constant for the other two OCs. This indicates that the dispersion of distributions from OC *RA* decreases as the distance increases, while those of the other cases do not change significantly. The values of the mean diameter D_{s1} and its spatial evolution are almost identical for all operating conditions. Finally, the evolution of the blob number N_{s1} shows that, for all operating conditions, the amount of population 1 blobs increases up to a certain distance (somewhere between $z = 14$ mm and $z = 18$ mm approxamately) and then decreases until the population disappears completely. As the momentum flux ratio J decreases from OC *RA* to OC *RC* (see Table 3.1), the dynamic pressure of the gas, $\rho_g U_g^2$, also decreases while that of the liquid remains nearly unchanged. The parameters obtained for population 1 seem to indicate an effect of the gaseous dynamic pressure on the dispersion and number of blobs from that population. Meanwhile, the mean diameter of these blobs is not significantly affected by this variation of the gaseous dynamic pressure.

Parameters from blob population 2 are shown in Figures 5.12(b), 5.13(b) and 5.14(b). Population 2 parameters also report similar spatial evolutions among the three operating

conditions. Parameter q_2 does not change with the increase of z, and similar values are reported for all cases. This indicates distributions whose dispersion changes very little with the position. The mean diameter D_{s2} reports fairly linear evolutions with z in all cases. The OC *RB* extends the evolution further downstream than the other cases. D_{s2} shows that the mean diameter of population 2 blobs continues to increase up to the most distant measured position. The blob number N_{s2} increases linearly with z until a certain position (around $z = 21$ mm). After this position, OCs *RA* and *RB* show a decrease in the blob number, while that of OC *RC* continues to increase. As mentioned previously, the evolution of the blob numbers N_{s1} and N_{s2} indicates that the textural atomization process includes more and more blobs as z increases, until reaching a position where the blob number is maximum. After this position, the blob number decreases. We note that the maximum blob number of OC *RA* is the hightest among the different cases. Also, the location of the maximum blob number for population 2 of OC *RC* is possibly not yet reached at the last measured position. The little effect of the changes in operating conditions on the parameters indicate that the characteristics of population 2 blobs are very weakly affected by the change in gaseous dynamic pressure. Indeed, their characteristics are more likely controled by the turbulence level in the liquid.

These observations indicate that the observed blob populations 1 and 2 have rather similar characteristics in all considered operating conditions. Indeed, pressure and momentum flux variations (due mostly to the variation of the dynamic pressure in the gas) distinguish one OC from another (see Table 3.1). Some difference can be observed in the dispersion and number of blobs from population 1, which is likely the effect of the changing dynamic pressure of the gas from one OC to the other. Meanwhile, the variation of the liquid Reynolds number is small and the amount of turbulence in the liquid is expected to be similar in all three cases. Therefore, the similarity between the blob diameter distributions (specially from population 2 blobs), in all the three operating conditions considered seems to indicate that the textural ligaments responsible for drop production are indeed initiated by the liquid turbulence, as reported by Wu et al. [1992].

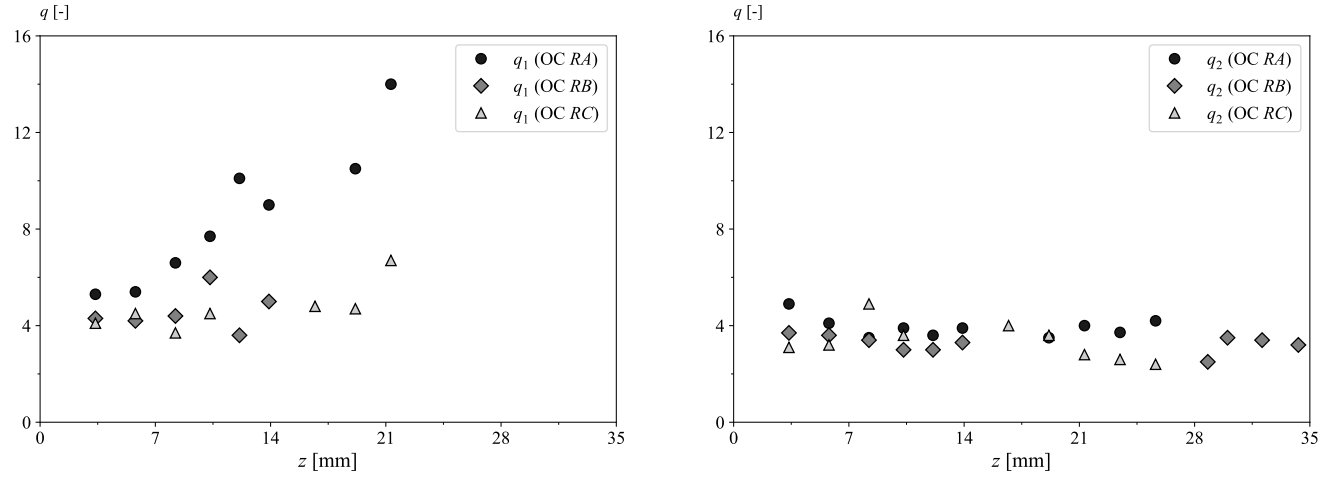

(a) (b)

FIGURE 5.12: Spatial evolution of the parameter q of the blob diameter distributions of (a) population 1 and (b) population 2, for all three operating conditions.

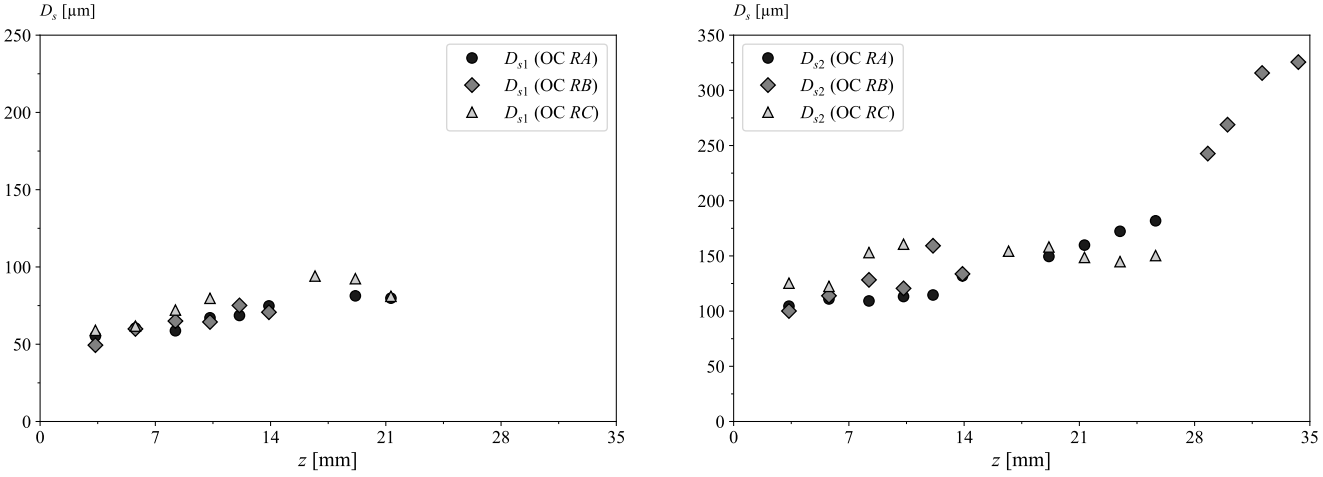

(a) (b)

FIGURE 5.13: Spatial evolution of the mean diameter D_s of the blob diameter distributions of (a) population 1 and (b) population 2, for all three operating conditions.

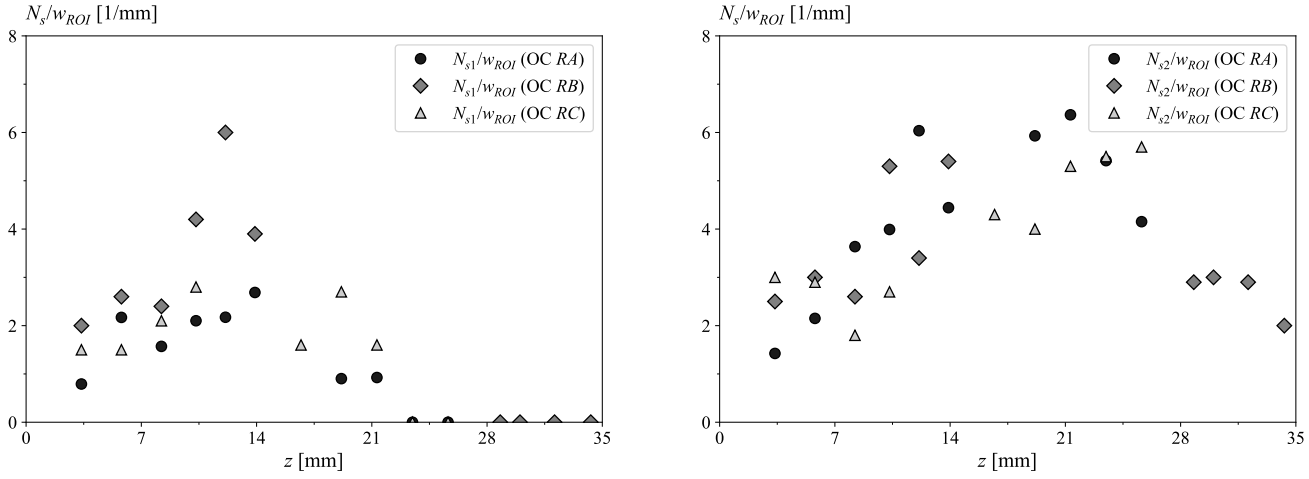

FIGURE 5.14: Spatial evolution of the weighed blob number N_s of the blob diameter distributions of (a) population 1 and (b) population 2, for all three operating conditions.

5.2 Non-reactive flow textural and structural atomization

The MARACA air-water fiber-regime atomization process (*PF-ONERA*, presented in Chapter 3, is considered here. The aim of this section is to present the analysis of the textural atomization process visualized experimentally at the MARACA test-bench by Herrera Leclerc [2022] and team and simulated numerically at ONERA by Hoarau et al. [2024]. Similarly to the analysis of the MASCOTTE textural atomization process, the goal is to describe the liquid ligaments involved in the textural atomization process and to provide an estimation of the size distribution of blobs in the liquid system that may become drops as the breakup process unfolds. Additionally, the comparison of the experimental and simulation cases can be used to validate the DNS simulation in terms of textural ligament production in the near-injector region.

5.2.1 Image processing and measurements

The experimental backlighting images from the MARACA case are processed using the same methodology described in Chapter 4 and used to process the MASCOTTE images, which includes the following steps: normalization, 4x4 sub-pixel interpolation, segmentation, droplet emilination and hole filling. The images produced from the DNS results are also processed with the methodology from Chapter 4. DNS images show the liquid phase with the desired spatial resolution against a white background (images are binary). This means that the sub-pixel treatment as well as the normalization and

segmentation steps are not necessary. Therefore the only processing applied includes the droplet elimination and hole filling steps.

An example image of each case is shown in Figure 5.15. On the top, a processed snapshot of the liquid system visualized experimentally in the MARACA test-bench is presented. On the bottom, a snapshot of a DNS image showing the 2D projection of the simulated liquid system. It is important to note that, in the DNS case, the liquid system contains long ligaments, mostly in the zone between $z = 12$ mm and $z = 25$ mm approximately. As discussed in Chapter 4, these long ligaments can cross one another in the 2D projection, resulting in the creation of holes in the liquid system. These holes are filled by the image post-processing. As in the MASCOTTE case, this may result in a reduction of the number captured structures, but it should not affect the size and dispersion of the remaining textural structures. Furthermore, other zones of the flow contain none, or nearly none of these holes and therefore do not suffer from this loss of information.

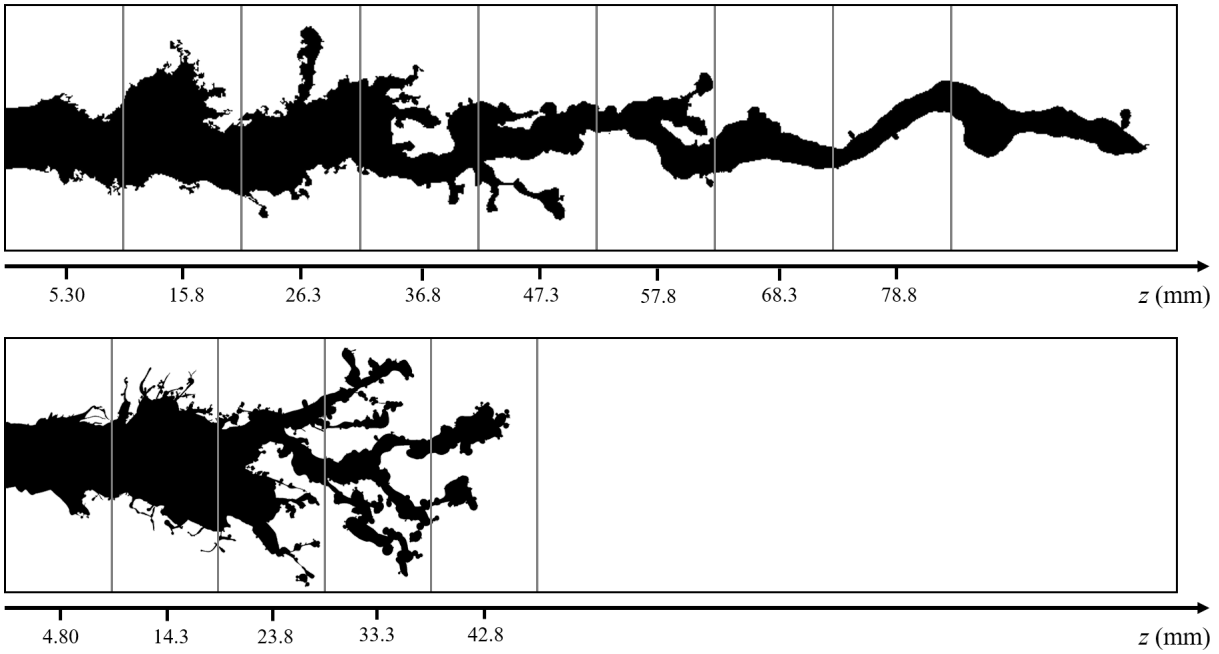

FIGURE 5.15: Snapshots of the visualized liquid core after image processing, and position of the defined ROIs. On the top: experimental image; on the bottom: DNS simulation image of the *PF-ONERA* case.

Differently from the MASCOTTE images considered in the previous section, the MARACA images show not only the liquid-gas interface but the entire liquid core. As Figure 5.15 suggests, the liquid core is much longer in the experimental images than in the simulation. Indeed, the large-scale structures detach at positions closer to the injector in the DNS case, leading to a shorter liquid core. These detached large-scale structures are eliminated by the image post-processing and therefore are not shown in Figure 5.15.

Small textural ligaments observed mostly in positions up to $z = 30$ mm approximately are thin and show little deformation. The main difference between experiments and simulation seems to be in the length of these ligaments, that seem longer in the simulated case. Thicker ligaments are also observed in positions between $z = 25$ mm and $z = 45$ mm approximately. These ligaments seem to have similar thicknesses and shapes in the two cases. As for the small ligaments near the injector, they seem longer in the simulation images.

As done in the MASCOTTE case study, images are divided into ROIs. In this case, their width is constant (10.5 mm for the experimental images and 9.5 mm for the DNS images). The ROIs are indicated in Figure 5.15 by gray rectangles. The z position of the center of each ROI is also indicated in the figure. In the experimental case, at positions between $z = 5.30$ mm and $z = 47.3$ mm approximately, small-scale textural ligaments are observed. We propose therefore to describe these textural ligaments by measuring the corresponding scale distributions.

Experimental image measurements

The $e_2(d)_{,d}$ distribution is measured at each ROI for a series of approximately 100 images in each case. The resulting time-averaged $-e_2(d)_{,d}$ distributions from the experimental case are plotted in Figure 5.16 as a function of the position z. All distributions are divided by the ROI width w_{ROI}. Figure 5.16 shows the measured $-e_2(d)_{,d}$ distributions from $z = 5.30$ mm to $z = 47.3$ mm. Differently from the MASCOTTE case, the distributions can now be shown in both the small- and large-scale ranges. For visualization purposes, the small-scale range [50 µm, 2000 µm] is plotted in Figure 5.16(a), while the large-scale range [2000 µm, 9000 µm] is shown in Figure 5.16(b). The small-scale range distributions show shapes and a spatial evolution similar to those observed in the MASCOTTE case: distributions show one peak, and become wider and decay at scales larger and larger as the distance z increases. This increase in the scale at which the distributions decay is indicative of the presence of larger and larger structures in the liquid system. In addition, the maximum value of the distribution first increases with z, then decreases. As explained in the description of the MASCOTTE process, this is indicative of an initial increase, and then decrease in the number and/or length of ligaments involved in the textural atomization process as the distance increases. The large-scale range distributions in Figure 5.16(b) show different shapes. Following a zone where very little structures are observed (and $-e_2(d)_{,d}$ is nearly equal to zero), the distributions show peaks at scales associated with the diameter of the liquid core at the respective positions. At $z = 5.30$ mm, where the liquid core shows low-amplitude, large-scale deformation, the distribution is fairly narrow. As the distance increases, the diameter of the liquid core begins to show more variation in time, which results in the distributions being more wide.

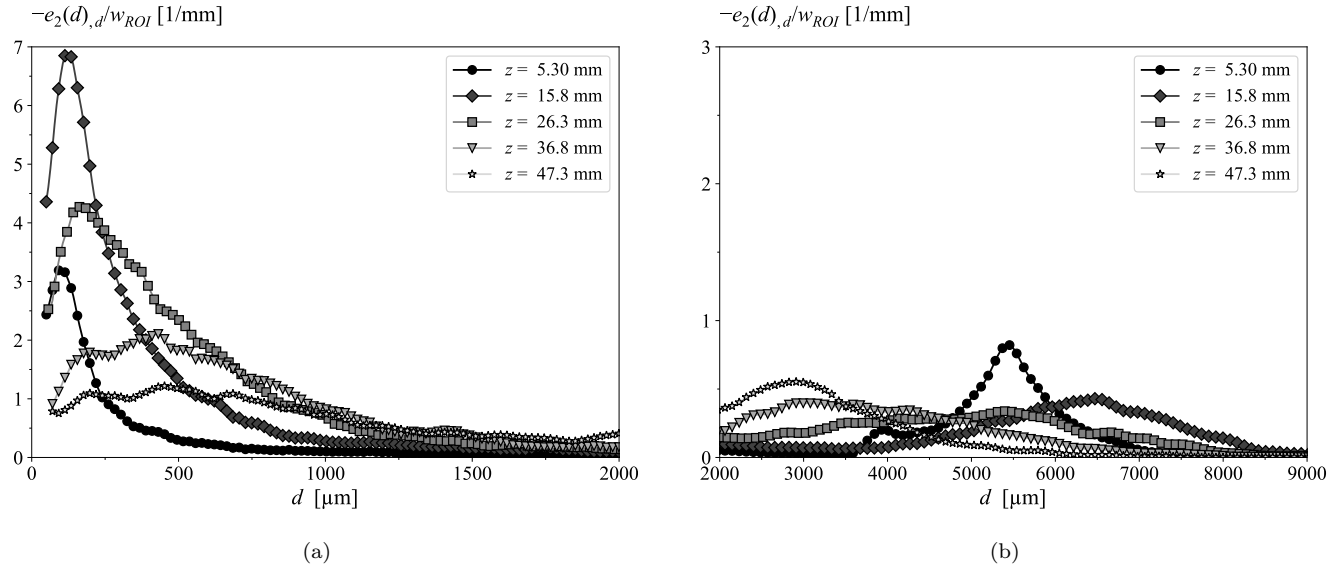

FIGURE 5.16: Distributions $-e_2(d)_{,d}/w_{ROI}$ at first four z positions of the experimental *PF-ONERA-Exp* case.

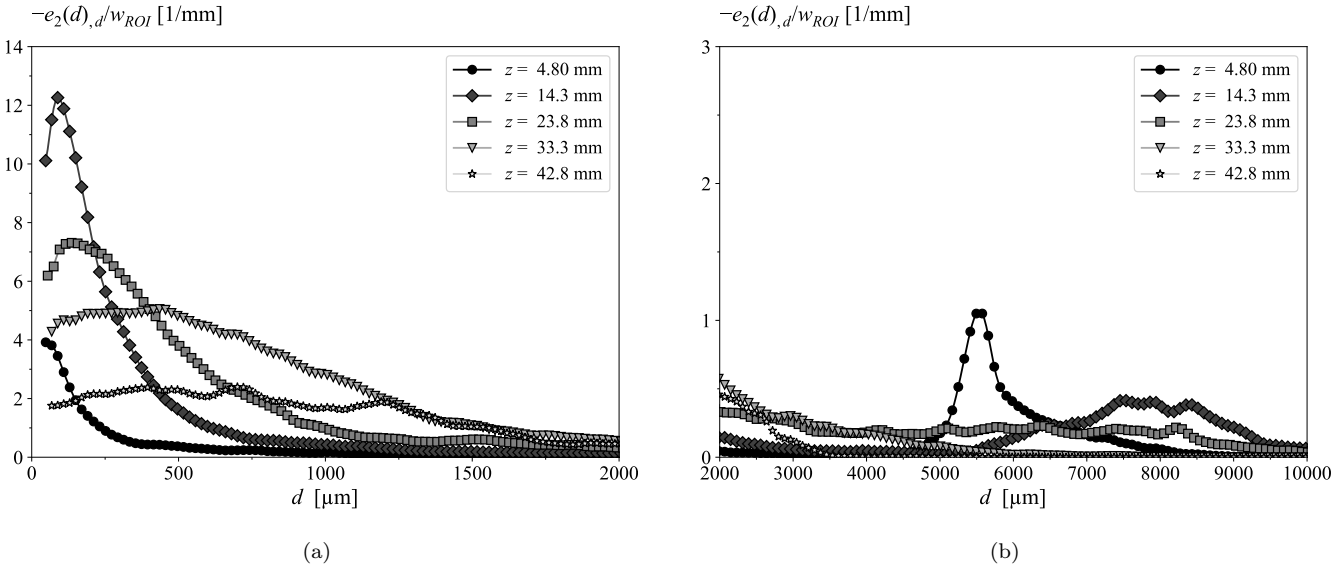

FIGURE 5.17: Distributions $-e_2(d)_{,d}/w_{ROI}$ at each z positions of the DNS *PF-ONERA* case.

DNS image measurements

As in the experimental case, the time-averaged $e_2(d)_{,d}$ distribution is measured at eat ROI for a series of approximately 100 images. The resulting distributions are plotted in Figure 5.17 as a function of the z position. As before, all distributions are divided by the ROI width w_{ROI}. Figure 5.17(a) covers the small-scale range [50 µm, 2000 µm] while Figure 5.17(b) covers the large-scale range [2000 µm, 10000 µm]. It can be seen that the distributions show very similar shapes and a similar spatial evolution as the

ones from the experimental case above, specially in the small-scale region. The same global observations as those for the distributions of the experimental case can therefore also be made here.

In the large-scale distributions (Figures 5.16(b) and 5.17(b)), some differences can be observed. At positions near $z = 15$ mm and $z = 25$ mm, the distributions in the large-scale zone extend to larger scales in the DNS case compared to the experiments. This indicated that, at these positions, the liquid core is wider in the DNS images. This is likely linked with the filling of holes created by the crossing of ligaments in the 2D projection. In addition, at the two farthest positions, near $z = 35$ mm and $z = 45$ mm, the distributions associated to the DNS decay at smaller scales compared to the experimental case. As observed earlier in the description of Figure 5.15, this is due to the presence of the a long intact liquid core at this positions in the experimental image, whereas in the DNS simulation this large structure detaches from the intact liquid core at shorter distances z, and is therefore eliminated from the images. The measured distributions allow to quantity large-scale differences observed in the images.

Since the goal of this section is to analyse the textural atomization process of these two cases, we focus our attention to the small-scale regions of the measured distributions. In this region, as mentioned previsouly, the global behavior of the distributions (shape and dependency on z) seems to be very similar for both cases. Note, however, that the scale of the ordinate axis of the small-scale graphs is different between the two cases (Figures 5.16(a) and 5.17(a)). Indeed, distributions from the DNS case are higher than those from the experimental case. This indicates that the number and/or length of the textural ligaments is greater in the DNS images. To further quantify the differences and similarities between the scale distributions in the small-scale region where the textural information is found, the analysis of the textural atomization process introduced in Section 5.1.2 is applied to the measured distributions of the current cases in the next section.

5.2.2 Comparison of experimental and simulation-based blob diameter distributions

The 2-blob-population model proposed and applied on the MASCOTTE images in Section 5.1.2 is again considered here. Previously, the model was used to estimate the diameter distribution of two families of blobs that are indicative of the drops produced by a textural atomization process. Here, the same model is applied to the measured $e_2(d)_{,d}$ distributions from the MARACA-case images reported in Figures 5.16(a) and 5.17(a).

Figure 5.18(a) reports the number-weighted blob diameter distributions resulting from the application of the 2-blob-population model on measurements from the experimental

images from positions $z = 5.30$ mm to $z = 47.3$ mm. Figure 5.18(b) reports the number-weighted blob diameter distributions resulting from the measurements made on DNS images as a function of the position z.

In both cases, the resulting blob diameter distributons have similar shapes and evolve similarly as a function of z. As noted in the description of the $e_2(d)_{,d}$ distributions, where distributions of the DNS case were higher than those of the experimental case, here the blob diameter distributions also report this difference. The parameters associated with the blob diameter distributions from these two cases are discussed in the following.

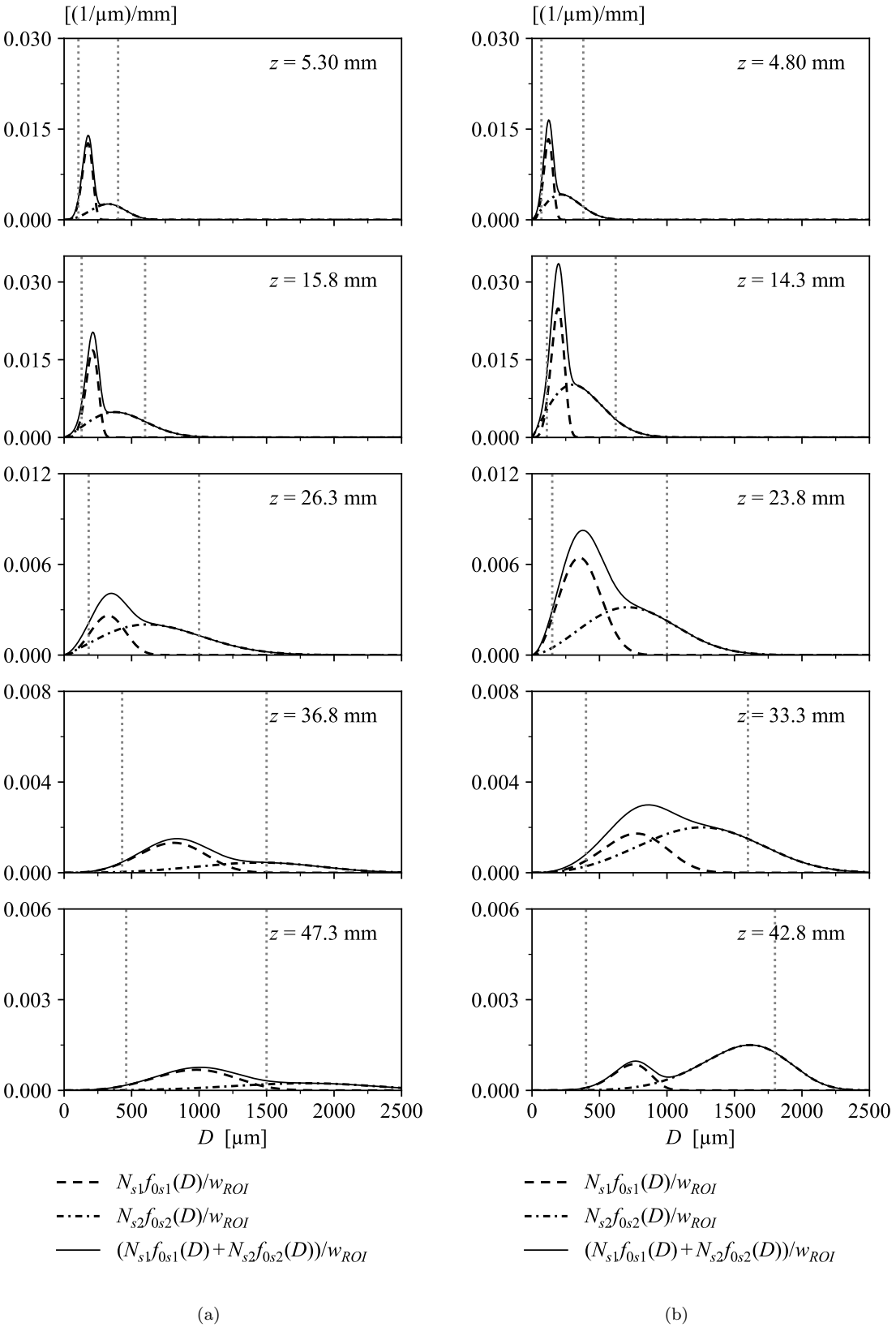

FIGURE 5.18: Number-weighted blob diameter distribution of populations 1 and 2, and their sum, for each z position of (a) the experimental *PF-ONERA-Exp* case (b) the DNS *PF-ONERA* case.

The parameters of the resulting number-weighted blob diameter distributions are plotted, as a funcion of z, in Figures 5.19-5.21 for both the experimental and DNS cases. Figures 5.19(a) and 5.19(b) report the spatial evolution of parameter q from populations 1 and 2 respectively. Figure 5.20(a) and 5.20(b) report the evolution of the mean diameter D_s from populations 1 and 2 respectively. Figures 5.21(a) and 5.21(b) report the weighed blob number N_s/w_{ROI} for populations 1 and 2 respectively.

The spatial evolutions of the parameters are very similar between both cases. Parameter q_1 does not show a clear dependency on z, while parameter q_2 shows a slow increase with z. The dispersion of population 1 is therefore fairly uniform in both cases, while that of population 2 seems to decrease with z. The mean diameters D_{s1} and D_{s2} show linear evolutions with z for both cases. The slope of this increase is higher for population 2. Finally, the blob numbers N_{s1}/w_{ROI} and N_{s2}/w_{ROI} first increase until approximately $z = 14$ mm where it reaches a maximum and then slowly decrease until almost reaching a zero value as z continues to increase. Note that, even with the loss of information due to the filling of holes created by ligament crossing in the DNS images, which are most frequent near $z = 14$ mm, this position is still associated with the highest blob numbers. This estimated position of the maximum reported blob numbers is in agreement with the drop number measurements in the DNS simulation from Hoarau et al. [2024] shown in Figure 3.16 where the zone of maximum number of droplets in the simulation is reported.

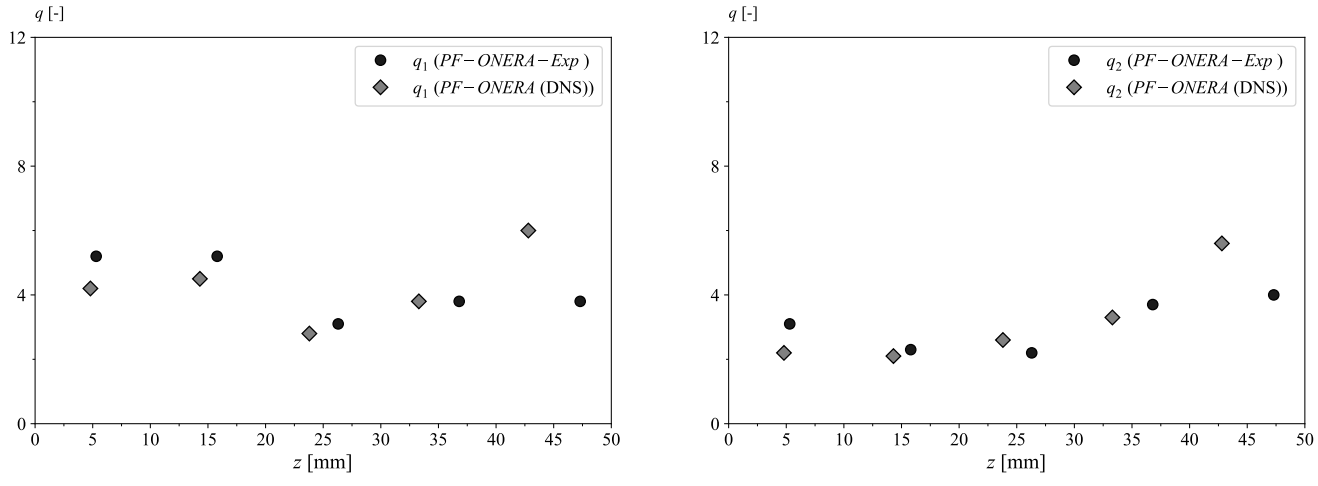

FIGURE 5.19: Spatial evolution of the parameter q of the blob diameter distributions of (a) population 1 and (b) population 2, for both the experimental and the DNS cases.

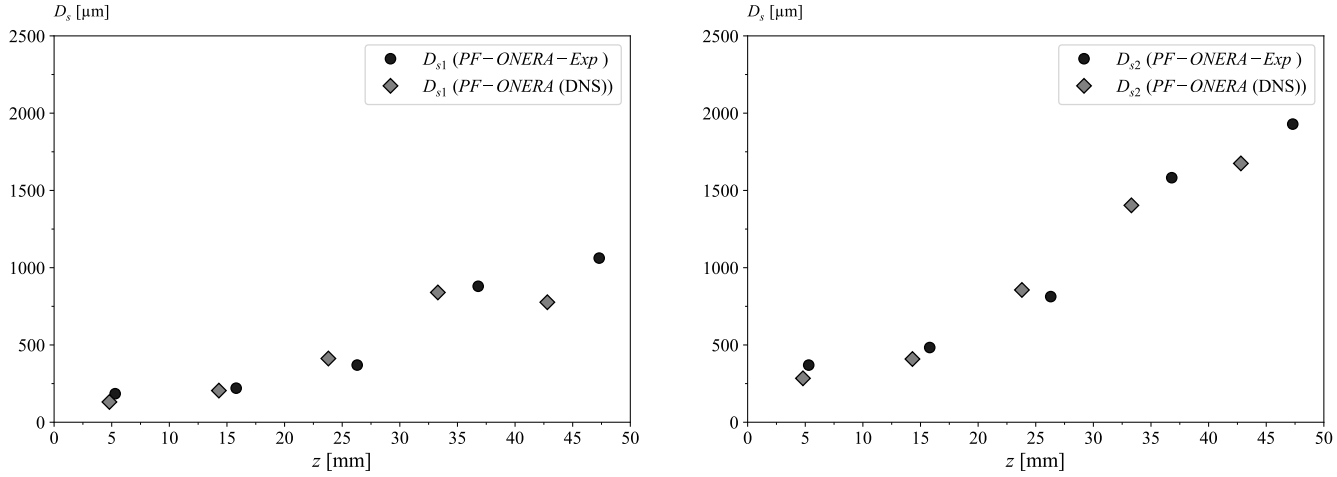

FIGURE 5.20: Spatial evolution of the mean diameter D_s of the blob diameter distributions of (a) population 1 and (b) population 2, for both the experimental and the DNS cases.

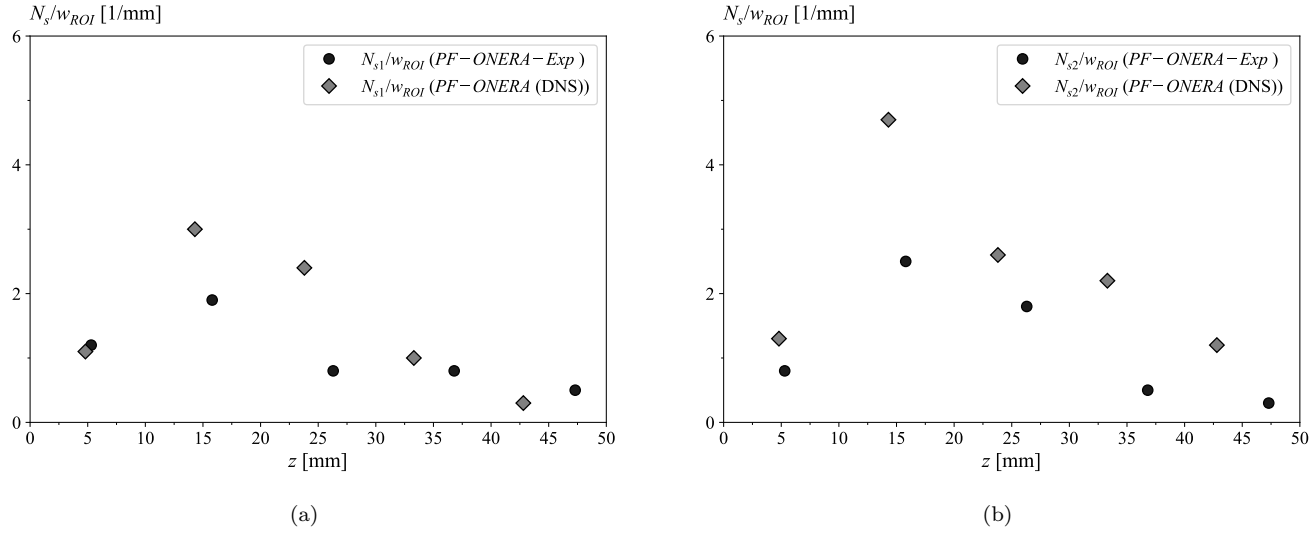

FIGURE 5.21: Spatial evolution of the weighed blob number $N_s/wROI$ of the blob diameter distributions of (a) population 1 and (b) population 2, for both the experimental and the DNS cases.

5.3 Conclusion

In this chapter, an analysis of textural atomization processes is proposed. Two different scenarios are considered: an experimental reactive flow textural atomization process named the MASCOTTE case, and a non-reactive atomization process, named the

MARACA case, which include experimental visualizations as well as visualizations produced from a DNS simulation.

The analysis of the textural atomization process includes a description of the liquid ligaments located at the liquid-gas interface by measuring their scale distribution at different distances from the injector exit plane. The measured time-averaged scale distributions contain information on the shape, the size and on the dispersion on these ligaments.

The observed ligaments are then associated with equivalent systems of constitutive circular blobs. Different families of blobs are identified in the measurements. Among these families, two populations of blobs that are associated with structures that are likely to produce drops of similar sizes when the ligament undergoes break up are identified. A model is then proposed where two blob populations are identified and characterized, based on the measured scale distributions. The model allows to estimate the size distribution of blobs of each population, as a function of the distance to the injector. A preliminary validation of the ligament-blob diameter distributions is proposed by applying the blob model to the droplets observed at a specific position and time interval. The results show that the resulting blob distributions of the droplet system is very similar to the ligament-blob diameter distributions found at that same position, indicating that the ligament-blobs are representative of the actual droplets produced in the textural atomization process.

The application of the model on measurements from the reactive MASCOTTE case allows to identify two blob populations that are associated with textural and structural deformations of the textural ligaments observed at the liquid-gas interface. The evolution of these blob diameter distributions allows to identify, for example, regions of the flow where drop production is more, or less, intense, and even regions where the textural process stops. The spatial evolution of the parameters of the resulting blob diameter distribution also seem to allow the development of models. The comparison of the three tested operating conditions shows that the influence of the chamber pressure and of the momentum flux ratio on the textural atomization process is limited and seems to only affect the dispersion and number of blobs from population 1. Meanwhile, parameters from population 2 blobs are not significatly affected by the changes in momentum flux ratio. Indeed, the similarities found in the measurements from different operating conditions seem to indicate that it is the turbulent fluctuations in the liquid phase (whose levels do not change significantly) that control the production of textural ligaments in this type of flow.

Next, the application of the model on measurements from the non-reactive MARACA case allows to compare the textural liquid ligaments observed at the interface of the liquid-gas flow both experimentally and in a DNS simulation. Results indicate that the characteristics of the textural ligaments reproduced by the simulation are very similar to the ones observed experimentally. The main difference found is related to the number

of blobs which is higher in the simulation results. This comparison indicates that the production of textural ligaments are correctly reproduced in the simulation, but that the ligaments seem to be longer on average than the ones observed experimentally, therefore resulting in a higher number of blobs. The study of the reactive MASCOTTE test-case has indicated that the liquid turbulence controls the production of textural ligaments. Therefore, the small differences reported between the DNS and experiments in the non-reactive MARACA case may be due to an incorrect reproduction of the liquid turbulence levels in the DNS simulation. We recall that, as described in Chapter 3, no turbulence is injected into the simulation domain. The turbulence in the liquid is therefore a result of the development of the flow inside the injector length that is included in the simulation domain. Finally, this work shows that the multi-scale analysis proposed in this chapter can be successfuly used to validate the textural atomization process reproduced by a DNS simulation.

Conclusion and perspectives

The work presented in this thesis is part of a general research effort to better understand the physical processes related to the subcritical combustion of propellants in liquid rocket engines. The main objective of the thesis was to develop a method to characterize the fiber-regime textural atomization process occurring inside the combustion chamber of these engines. To do so, the proposed method must be capable of capturing the small-scale deformation of the liquid-gas interface associated with the textural atomization process. The textural atomization of coaxial jets in the fiber regime is associated with the development of liquid ligaments at the interface. To better understand the primary atomization process, a description of the production of these ligaments and of how they break up into drops must be provided. Doing this, the method should allow the description of ligaments related to textural atomization processes in reactive conditions, which are representative of the environment found inside real rocket engine combustion chambers, but also in non-reactive conditions, which are commonly found in the literature related to atomization. The proposed method should allow not only the experimental description of the textural ligaments, but of any atomization system, including those reproduced by numerical simulations. The experimental description of the textural atomization process should help in the development of numerical primary atomization models. The comparison of the description of simulated textural ligaments to that of ligaments observed experimentally should allow to validate the numerical reproduction of the process.

The method proposed in this thesis to characterize the textural atomization process is based on a morphological multi-scale description of liquid systems found in the literature. The thesis starts with a brief contextualization of the research and a presentation of the state of the art on the primary atomization of coaxial assisted jets in Chapter 1. Then, in Chapter 2, the multi-scale method is introduced. The chapter begins with a presentation of the theoretical aspects of the multi-scale description from the literature. Then, an image analysis method is proposed to measure the scale distribution of liquid systems, particularly in the small-scale range associated with textural atomization processes. The importance of high-spatial-resolution in the images is highlighted and the methodology is adapted to improve the resolution of the measured scale distribution. Finally, the developed method is used to describe the breakup process of an isolated liquid ligament.

This allowed to draw insights about how the signature of the drops produced can be found in the scale distribution of the ligament before its breakup.

Chapter 3 is dedicated to the presentation of the atomization processes studied in the thesis. The main application is a reactive configuration studied experimentally in the MASCOTTE test-bench at ONERA using liquid oxygen and methane as propellants. The experimental work on this configuration performed during this PhD allowed to record high-resolution and high-quality images of the liquid-gas interface topology, as a function of the distance to the injector, in the reactive environment of the MASCOTTE test-bench. Three operating conditions in the subcritical regime were defined and tested. The second application is the non-reactive, air-water atomization process studied in the MARACA test-bench at CORIA. Images obtained by experimental and direct numerical simulation studies conducted prior to this thesis by CORIA and ONERA teams, showing the liquid-gas interface during the atomization process, are presented.

Next, in Chapter 4, a methodology is developed to allow the post-processing of the raw images of the liquid-gas interface presented in Chapter 3. The proposed method allowed to isolate and resolve the small-scale, textural ligaments observed in images of the liquid-gas interface. The application of the post-processing on images of the reactive MASCOTTE configuration allowed to make a qualitative description of the textural atomization process based on the resulting post-processed images. Finally, the application of the measurement technique, introduced in Chapter 2, on the post-processed images of the MASCOTTE configuration enabled the identification of the smallest resolved scale of the measured scale distributions.

Finally, in Chapter 5, the results of the application of the multi-scale method on the post-processed images of both reactive and non-reactive configurations are presented. Scale distributions are measured and used to describe the shape, size and number of the observed textural ligaments and their evolution as a function of the distance to the injector. These ligaments are then associated with families of constitutive circular blobs. A model is proposed to associate the measured scale distributions of the ligaments with two populations of blobs and to estimate their diameter distributions. The application of the model to measurements from the reactive MASCOTTE configuration reported that the mean blob diameter increases with the distance to the injector. The number of blobs, on the other hand, increases until a given position where it reaches a maximum, and then decreases. This indicates that the observed textural ligaments are thicker and thicker as the distance increases. At the same time, their number and/or length first increases, reaches a maximum and then decreases until the textural atomization reaches a stop. The comparison of the three operating conditions tested in the MASCOTTE test-bench showed only a limited dependency on the chamber pressure or on the momentum flux ratio in the value ranges considered here. Further tests with operating conditions reaching up to 30 or 40 bars of pressure and with a larger range of momentum flux ratios would be required in order to have a more complete understanding of the effect of

these parameters on the ligament characteristics. As concluded by other studies in the literature [Wu and Faeth, 1993, Wu et al., 1992, 1995], the results seem to indicate that the production of textural ligaments is initiated by the turbulence in the liquid phase. The same methodology was applied to the non-reactive MARACA configuration in order to compare the textural atomization processes observed experimentally and reproduced in the direct numerical simulation. The results from the comparison report that the observed textural ligaments have very similar sizes and deformations, and very similar spatial evolutions. The main difference reported is the number of blobs, related to the length of the textural ligaments which is higher in the numerical simulation. These results indicate that the textural process is correctly reproduced by the simulation, validating the simulation methodology regarding the textural ligament production.

The blobs from the two populations reported by the model proposed in Chapter 5 correspond to sections of the ligaments that will likely break up into drops of sizes similar to the diameter of the associated blobs. The diameter distribution of these blobs can therefore be seen as indicative of the local size distribution of the main drops produced by the textural ligaments. These results can therefore be very useful to the development of numerical models for primary atomization, where initial local drop diameter distributions must be estimated.

The work presented in this thesis answers to most of the objectives identified previously. The proposed multi-scale method provides a quantitative and detailed characterization of the textural atomization process in reactive and non-reactive conditions, and in both experimental and numerical frameworks. It gave access to the spatial evolution of the different textural processes considered and allowed to compare different cases and to validate results from a numerical simulation. Despite these contributions, the work also opens many doors for further complementing studies and developments.

The experimental work done in the MASCOTTE test-bench raised several difficulties related to the quality of the recorded backlighting images. These difficulties are mostly related to the effects of the strong optical index gradients produced by the extreme conditions of the reactive environment. The study of the textural atomization process could benefit from further development in the backlighting imaging technique to reduce these effects, facilitating the post-processing of the images and possibly allowing to reach higher pressures without losing too much signal. The backlighting technique seems to be too sensitive to optical index gradients, as a in a schlieren setup, even with the use of a collimated and diffuse incident light. These schlieren gradients are difficult to suppress as they originate from effects caused by the flame, but also from the turbulence and gas composition in the gas flow [Fdida et al., 2019]. A diffuser plate producing less collimated light could be developed to decrease the optical index gradients in images. Furthermore, a more comprehensive experimental campaign would allow to record images of the zones in the flow that were not studied in this thesis due to a limited number of tests allowed

at the test-bench. A more complete parametric study could also be done to study the influence of certain injection parameters on the textural atomization process.

Another interesting perspective of this work is the analysis of the liquid system without the filling of holes produced by ligaments crossing one another as an effect of the 2D projection. This would require some theoretical advances in the multi-scale model proposed to also consider systems that are not homeomorphic to cylinders.

The work also raised interesting ideas for the description of liquid-gas interfaces reproduced by LES simulations, which could allow the validation of the textural atomization process reproduced in this type of simulation. The diffuse interface methods in particular pose difficulties related to the determination of the precise position of the interface, which is necessary in the current multi-scale method. An interesting solution would be the use of an interface reconstruction technique to estimate the precise location of the interface from diffuse-interface simulation results. Alternatively, the 3D version of the multi-scale method considered in this thesis can be developped. A volume-based scale distribution was recently presented in the literature and could be used in the current framework to compare results from the 2D and 3D approaches for the DNS simulation case, for example. The multi-scale description of the textural atomization process, which allows quantitative and detailed estimations of the size of structures involved, is a promising approach for the experimental description of the process, for the validation of results from numerical simulations and even for the development of models of the textural atomization process.

Number-weighted blob diameter distributions

This appendix presents the complete number-weighted blob diameter distributions, as a function of the distance to the injector, from all three operating conditions tested in the MASCOTTE test-bench and summarized in Table 3.1.

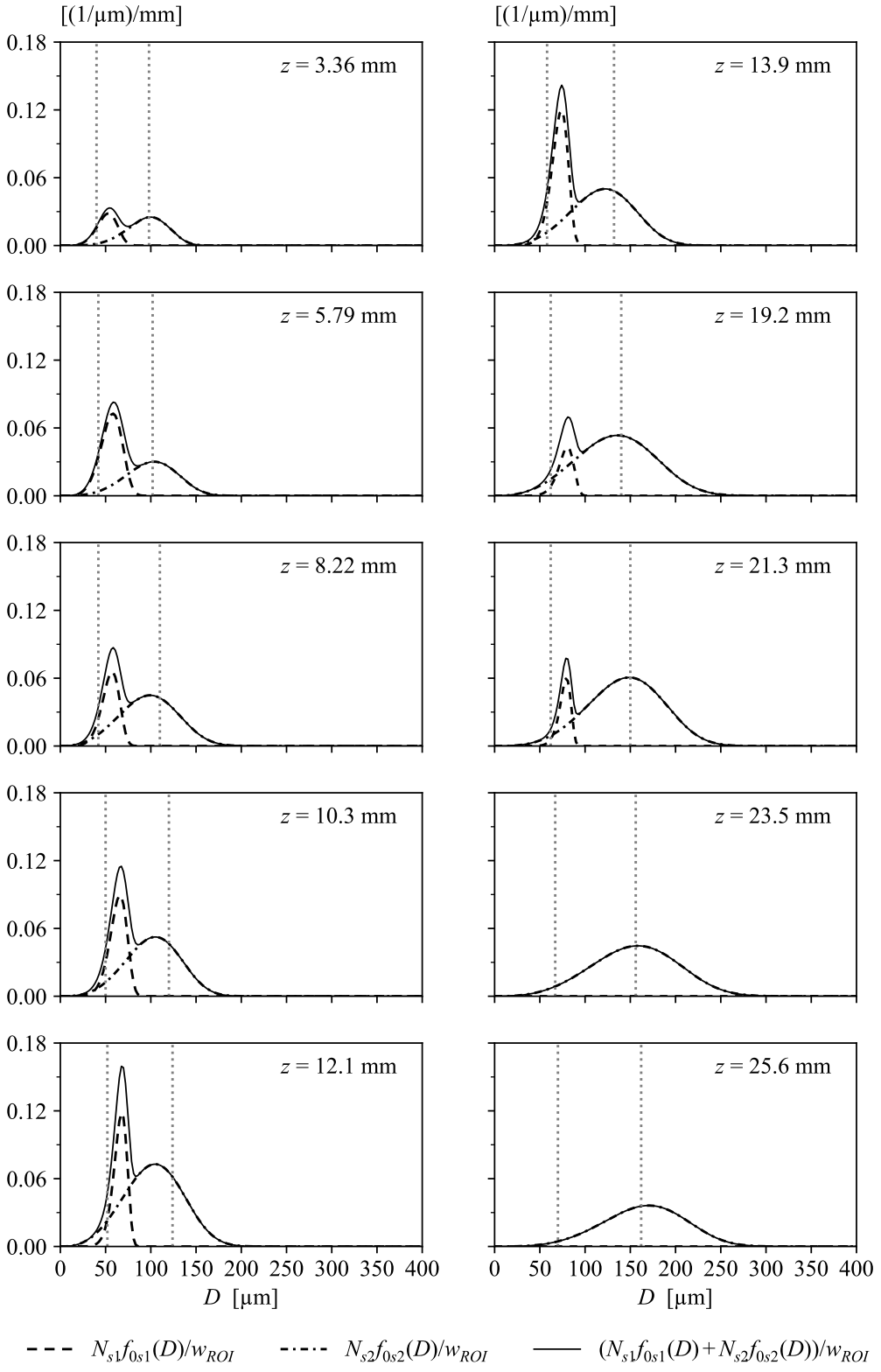

FIGURE A.1: Weighed blob diameter distribution of populations 1 and 2, and their sum, for each z position of OC *RA*.

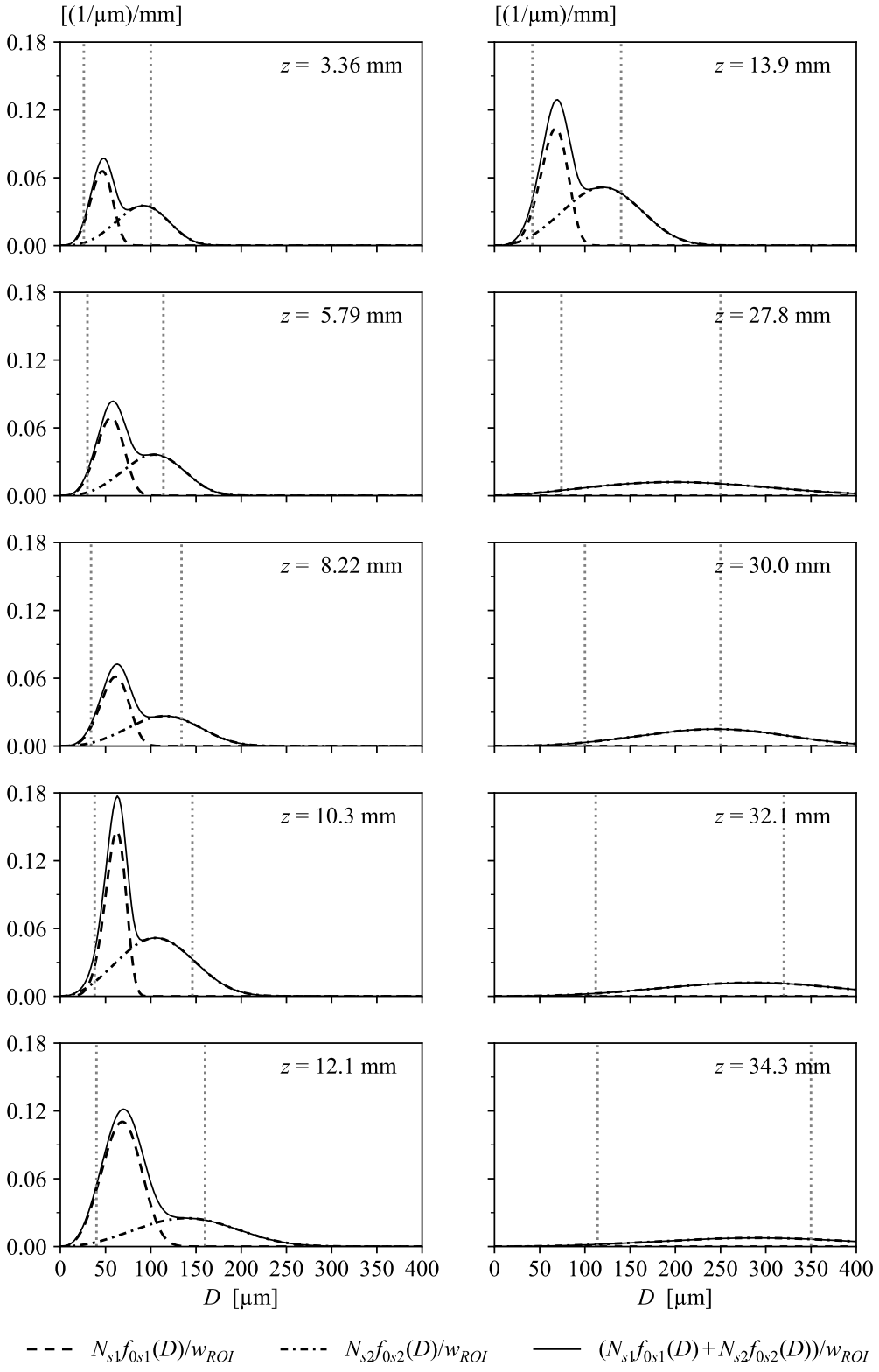

FIGURE A.2: Weighed blob diameter distribution of populations 1 and 2, and their sum, for each z position of OC *RB*.

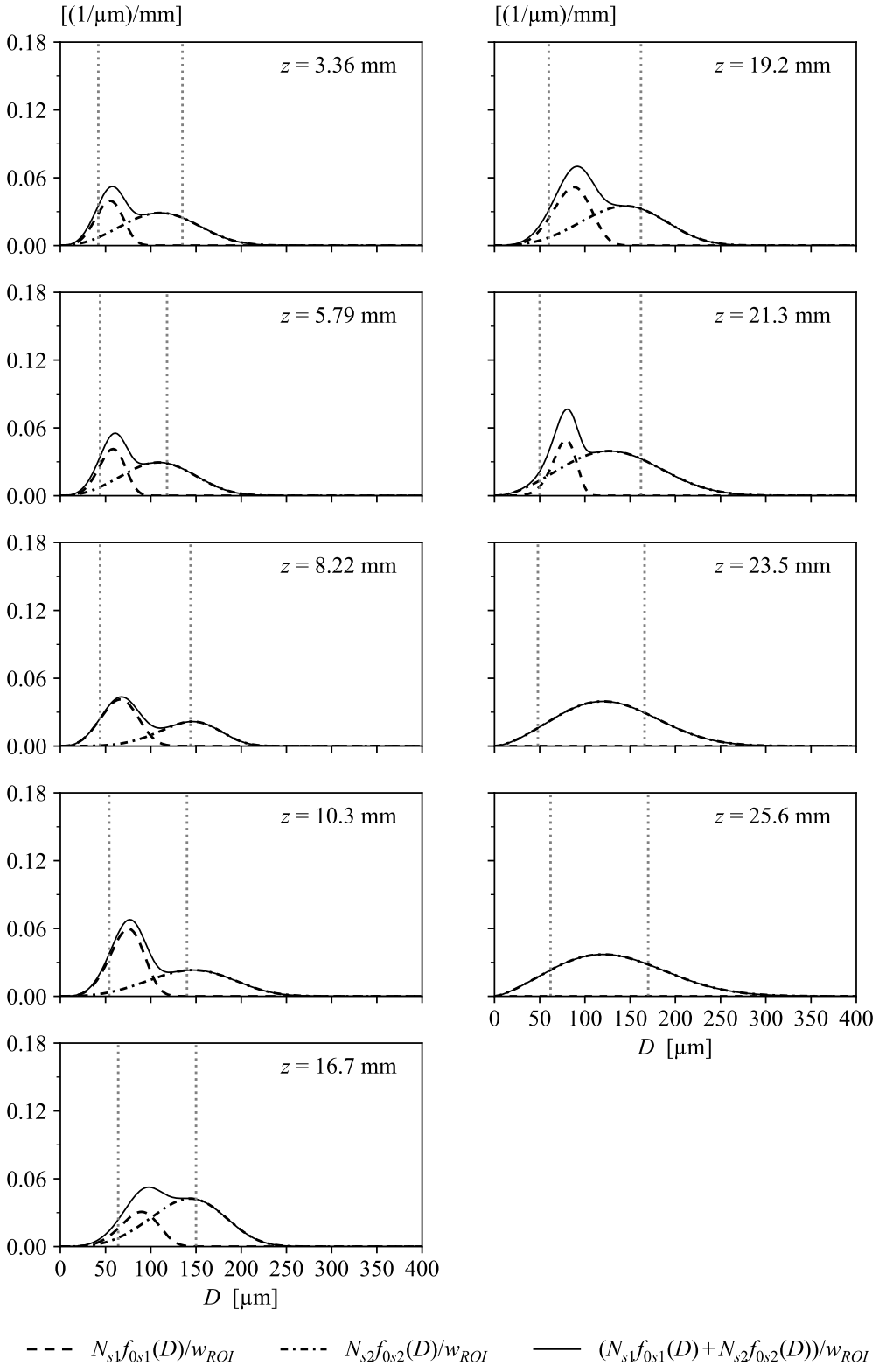

FIGURE A.3: Weighed blob diameter distribution of populations 1 and 2, and their sum, for each z position of OC *RC*.

List of Figures

List of Tables

Bibliography

M. Averseng, D. Zuzio, A. Boutsikakis, and J.-L. Estivalèzes. Dns simulation and analysis of periodic planar liquid sheet assisted atomization. In *10th International Conference on Multiphase Flow (ICMF 2019)*, 2019.

E. Babinsky and P. Sojka. Modeling drop size distributions. *Progress in energy and combustion science*, 28(4):303–329, 2002.

F. Baillot, J.-B. Blaisot, G. Boisdron, and C. Dumouchel. Behaviour of an air-assisted jet submitted to a transverse high-frequency acoustic field. *Journal of Fluid Mechanics*, 640:305–342, 2009.

S. Boulal, N. Fdida, L. Matuszewski, L. Vingert, and M. Martin-Benito. Flame dynamics of a subscale rocket combustor operating with gaseous methane and gaseous, subcritical or transcritical oxygen. *Combustion and Flame*, 242:112179, 2022.

W. Burger and M. J. Burge. *Digital image processing: An algorithmic introduction.* Springer Nature, 2022.

S. Candel, M. Juniper, G. Singla, P. Scouflaire, and C. Rolon. Structure and dynamics of cryogenic flames at supercritical pressure. *Combustion Science and Technology*, 178 (1-3):161–192, 2006.

J. Chesnel, J. Reveillon, T. Menard, and F.-X. Demoulin. Large eddy simulation of liquid jet atomization. *Atomization and Sprays*, 21(9), 2011.

N. Chigier and Z. Farago. Morphological classification of disintegration of round liquid jets in a coaxial air stream. *Atomization and sprays*, 2(2), 1992.

F. Couderc. *Développement d'un code de calcul pour la simulation d'écoulements de fluides non miscibles. Application à la désintégration assistée d'un jet liquide par un courant gazeux.* PhD thesis, Ecole nationale superieure de l'aeronautique et de l'espace, 2007.

J. Cousin and C. Dumouchel. Coupling of classical linear theory and maximum entropy formalism for prediction of drop size distribution in sprays: application to pressure-swirl atomizers. *Atomization and Sprays*, 6(5), 1996.

D. W. Davis and B. Chehroudi. Measurements in an acoustically driven coaxial jet under sub-, near-, and supercritical conditions. *Journal of Propulsion and Power*, 23 (2):364–374, 2007.

C. Dumouchel. A new formulation of the maximum entropy formalism to model liquid spray drop-size distribution. *Particle & Particle Systems Characterization*, 23(6): 468–479, 2006.

C. Dumouchel. On the experimental investigation on primary atomization of liquid streams. *Experiments in fluids*, 45:371–422, 2008.

C. Dumouchel and S. Boyaval. Use of the maximum entropy formalism to determine drop size distribution characteristics. *Particle & Particle Systems Characterization: Measurement and Description of Particle Properties and Behavior in Powders and Other Disperse Systems*, 16(4):177–184, 1999.

C. Dumouchel, J. Cousin, and S. Grout. Analysis of two-dimensional liquid spray images: the surface-based scale distribution. *Journal of Flow Visualization and Image Processing*, 15(1), 2008.

C. Dumouchel, J.-B. Blaisot, F. Abuzahra, A. Sou, G. Godard, and S. Idlahcen. Analysis of a textural atomization process. *Experiments in Fluids*, 60:1–16, 2019.

C. Dumouchel, F. Thiesset, and T. Ménard. Morphology of contorted fluid structures. *International Journal of Multiphase Flow*, 152:104055, 2022.

C. Dumouchel, L. Cottier, and M.-C. Renoult. Fine characterization of the capillary instability of free viscoelastic jets. *Journal of Non-Newtonian Fluid Mechanics*, 322: 105135, 2023.

H. Eroglu, N. Chigier, and Z. Farago. Coaxial atomizer liquid intact lengths. *Physics of Fluids A: Fluid Dynamics*, 3(2):303–308, 1991.

S. Fadnavis. Image interpolation techniques in digital image processing: an overview. *International Journal of Engineering Research and Applications*, 4(10):70–73, 2014.

N. Fdida, L. Vingert, G. Ordonneau, and S. Petitot. Coupling high-speed imaging diagnostics to study a lox/gh2 flame in a high-pressure rocket combustor. In *5th European Conference for Aeronautics and Space Sciences*, pages 1–13. EUCASS Assoc. Munich, 2013.

N. Fdida, L. Vingert, A. Ristori, and Y. Le Sant. Droplet size and velocity measurements in a cryogenic jet flame of a rocket-type combustor using high-speed imaging. *Atomization and Sprays*, 26(5), 2016.

N. Fdida, L. Vingert, Y. Mauriot, L.-H. Dorey, and M. Théron. Comparison of lox/methane and lox/hydrogen cryogenic spray combustion with simultaneous optical diagnostics. In *EUCASS 2019*, pages 1–10, 2019.

A. Ficuciello, J. Blaisot, C. Richard, and F. Baillot. Investigation of air-assisted sprays submitted to high frequency transverse acoustic fields: Droplet clustering. *Physics of Fluids*, 29(6), 2017.

F. Granger. *Modélisation de l'atomisation primaire d'oxygène liquide dans les flammes diphasiques des moteurs fusées à ergols liquides.* PhD thesis, Toulouse, ISAE, 2023.

P. Grenard, N. Fdida, L. Vingert, L.-H. Dorey, L. Selle, and J. Pichillou. Experimental investigation of heat transfer in a subscale liquid rocket engine. *Journal of Propulsion and Power*, 35(3):544–551, 2019.

S. Grout, C. Dumouchel, J. Cousin, and H. Nuglisch. Fractal analysis of atomizing liquid flows. *International Journal of Multiphase Flow*, 33(9):1023–1044, 2007.

D. Guildenbecher, C. López-Rivera, and P. Sojka. Secondary atomization. *Experiments in Fluids*, 46(3):371–402, 2009.

M. Habiballah, M. Orain, F. Grisch, L. Vingert, and P. Gicquel. Experimental studies of high-pressure cryogenic flames on the mascotte facility. *Combustion Science and Technology*, 178(1-3):101–128, 2006.

R. A. Herrera Leclerc. *Experimental study of assisted jets in a pressurized atmosphere and modeling in the presence of non-linear effects of acoustics.* PhD thesis, Normandie Université, 2022.

J.-C. Hoarau, L.-H. Dorey, D. Zuzio, F. Granger, and J.-L. Estivalezes. Direct numerical simulation of a subcritical coaxial injection in fiber regime using sharp interface reconstruction. *International Journal of Multiphase Flow*, 180:104974, 2024.

E. Hopfinger. Liquid jet instability and atomization in a coaxial gas stream. In *Advances in Turbulence VII: Proceedings of the Seventh European Turbulence Conference, held in Saint-Jean Cap Ferrat, France, 30 June–3 July 1998/Actes de la Septième Conférence Européenne de Turbulence, tenue à Saint-Jean Cap Ferrat, France, 30 Juin–3 Juillet 1998*, pages 69–78. Springer, 1998.

M. Ishii and T. Hibiki. *Thermo-fluid dynamics of two-phase flow.* Springer Science & Business Media, 2010.

M. Juniper, A. Tripathi, P. Scouflaire, J.-C. Rolon, and S. Candel. Structure of cryogenic flames at elevated pressures. *Proceedings of the Combustion Institute*, 28(1):1103–1109, 2000.

B. H. Kaye. *A Random Walk Through Fractal Dimensions.* Wiley-VCH, 1994.

J. C. Lasheras and E. Hopfinger. Liquid jet instability and atomization in a coaxial gas stream. *Annual review of fluid mechanics*, 32(1):275–308, 2000.

C. Le Touze. *Couplage entre modèles diphasiques à phases séparées et à phase dispersée pour la simulation de l'atomisation primaire en combustion cryotechnique*. PhD thesis, Université Nice Sophia Antipolis, 2015.

C. Le Touze, L.-H. Dorey, N. Rutard, and A. Murrone. A compressible two-phase flow framework for large eddy simulations of liquid-propellant rocket engines. *Applied Mathematical Modelling*, 84:265–286, 2020.

V. Lechner. *Experimental study of LOX/CH4 flames in rocket engines*. PhD thesis, université Paris-Saclay, 2024.

M. Lecompte and C. Dumouchel. On the capability of the generalized gamma function to represent spray drop-size distribution. *Particle & Particle Systems Characterization*, 25(2):154–167, 2008.

D.-T. Lee. Medial axis transformation of a planar shape. *IEEE Transactions on pattern analysis and machine intelligence*, (4):363–369, 1982.

A. Lefebvre. Atomization and sprays, hemisphere pub. vol. 1989. *New York: Corp*, 1989.

B. Leroux, O. Delabroy, and F. Lacas. Experimental study of coaxial atomizers scaling. part i: dense core zone. *Atomization and Sprays*, 17(5), 2007.

X. Li, R. S. Tankin, B. Sztal, and J.-M. Most. Derivation of droplet size distribution in sprays by using information theory. *Combustion science and technology*, 60(4-6): 345–357, 1988.

X. Li, R. S. Tankin, and M. Renksizbulut. Calculated characteristics of droplet size and velocity distributions in liquid sprays. *Particle & particle systems characterization*, 7 (1-4):54–59, 1990.

J. Lux and O. Haidn. Flame stabilization in high-pressure liquid oxygen/methane rocket engine combustion. *Journal of Propulsion and Power*, 25(1):15–23, 2009.

P. Marmottant and E. Villermaux. On spray formation. *Journal of fluid mechanics*, 498:73–111, 2004.

I. Marter. *Méthode d'interface immergée pour la simulation directe de l'atomisation primaire*. PhD thesis, Institut supérieur de l'Aéronautique et de l'Espace (ISAE); Université de ..., 2017.

K. R. Mecke and H. Wagner. Euler characteristic and related measures for random geometric sets. *Journal of Statistical Physics*, 64(3):843–850, 1991.

R. Mugele and H. Evans. Droplet size distribution in sprays. *Industrial & Engineering Chemistry*, 43(6):1317–1324, 1951.

V. D. Ngo. *Etude de la morphologie des éléments d'un spray liquide et de leur production.* Phd thesis, Université de Rouen, Rouen, France, February 2013.

G. Ordonneau, P. Hervat, L. Vingert, S. Petitot, and B. Pouffary. First results of heat transfer measurements in a new water-cooled combustor on the mascotte facility. In *Proceedings of the 4th European Conference for Aerospace Sciences (EUCASS'11)*, 2011.

N. Phansalkar, S. More, A. Sabale, and M. Joshi. Adaptive local thresholding for detection of nuclei in diversity stained cytology images. In *2011 International conference on communications and signal processing*, pages 218–220. IEEE, 2011.

E. Porcheron, J.-L. Carreau, D. Le Visage, and F. Roger. Effect of injection gas density on coaxial liquid jet atomization. *Atomization and Sprays*, 12(1-3), 2002.

N. Rutard. *Simulation numérique et modélisation de l'influence d'ondes acoustiques de haute amplitude sur un jet diphasique: application au domaine de la propulsion fusée à ergols liquides.* PhD thesis, Université Paris Saclay (COmUE), 2019.

N. Rutard, L.-H. Dorey, C. Le Touze, and S. Ducruix. Large-eddy simulation of an air-assisted liquid jet under a high-frequency transverse acoustic forcing. *International Journal of Multiphase Flow*, 122:103144, 2020.

R. Sellens and T. Brzustowski. A prediction of the drop size distribution in a spray from first principles. *Atomisation Spray Technology*, 1(2):89–102, 1985.

R. W. Sellens. Prediction of the drop size and velocity distribution in a spray, based on the maximum entropy formalism. *Particle & Particle Systems Characterization*, 6 (1-4):17–27, 1989.

W. Sirignano and C. Mehring. Comments on energy conservation in liquid-stream disintegration. In *Proceedings of ICLASS*, 2000.

M. Theron, M. M. Benito, B. Vieille, L. Vingert, N. Fdida, Y. Mauriot, R. Blouquin, C. Seitan, M. Onori, and L. Lequette. Experimental and numerical investigation of lox/methane cryogenic combustion at low mixture ratio. In *8th European Conference for Aeronautics and Space Sciences (EUCASS), Madrid, Spain*, 2019.

E. Villermaux. Fragmentation. *Annu. Rev. Fluid Mech.*, 39(1):419–446, 2007.

E. Villermaux, P. Marmottant, and J. Duplat. Ligament-mediated spray formation. *Physical review letters*, 92(7):074501, 2004.

L. Vingert, G. Ordonneau, N. Fdida, and P. Grenard. A rocket engine under a magnifying glass. *Aerospace Lab*, (11):15, 2016.

L. Vingert, N. Fdida, Y. Mauriot, I. O. Colomer, C. Irimea, D. Delhaye, A. K. Mohamed, V. Corbas, and M. Theron. Experimental investigations of liquid oxygen/methane combustion at very low mixture ratio at the mascotte test facility. In *32nd ISTS & 9th NSAT Joint Symposium*, 2019.

F. A. Williams. Spray combustion and atomization. *The physics of fluids*, 1(6):541–545, 1958.

R. Woodward, R. Burch, K. K. Kuo, and F. B. Cheung. Correlation of intact-liquid-core length for coaxial injectors. In *ICLASS 94 Proceedings of the Sixth International Conference on Liquid Atomization and Spray Systems*. Begell House, 1994.

P.-K. Wu and G. M. Faeth. Aerodynamic effects on primary breakup of turbulent liquids. *Atomization and Sprays*, 3(3), 1993.

P.-K. Wu, L.-K. Tseng, and G. M. Faeth. Primary breakup in gas/liquid mixing layers for turbulent liquids. *Atomization and sprays*, 2(3), 1992.

P.-K. Wu, R. d. Miranda, and G. M. Faeth. Effects of initial flow conditions on primary breakup of nonturbulent and turbulent round liquid jets. *Atomization and sprays*, 5 (2), 1995.

T. Xavier, D. Zuzio, M. Averseng, and J.-L. Estivalezes. Toward direct numerical simulation of high speed droplet impact. *Meccanica*, 55:387–401, 2020.

B. Yang, F. Cuoco, and M. Oschwald. Atomization and flames in lox/h2-and lox/ch4-spray combustion. *Journal of Propulsion and Power*, 23(4):763–771, 2007.

D. L. Youngs. Time-dependent multi-material flow with large fluid distortion. *Numerical methods for fluid dynamics*, 1982.

D. Zuzio. *Direct numerical simulation of two phase flows with adaptive mesh refinement.* PhD thesis, Ecole nationale superieure de l'aeronautique et de l'espace, 2010.

D. Zuzio, J.-L. Estivalèzes, and B. DiPierro. An improved multiscale eulerian–lagrangian method for simulation of atomization process. *Computers & Fluids*, 176:285–301, 2018.

D. Zuzio, A. Orazzo, J.-L. Estivalèzes, and I. Lagrange. A new efficient momentum preserving level-set/vof method for high density and momentum ratio incompressible two-phase flows. *Journal of Computational Physics*, 410:109342, 2020.